2019

As-Manufactured Modeling of a Mistuned Turbine Engine Compressor Evaluated Against Experimental Approaches

Daniel L. Gillaugh
Wright State University

As-Manufactured Modeling of a Mistuned Turbine Engine Compressor Evaluated Against Experimental Approaches

A Dissertation submitted in partial fulfillment
of the requirements for the degree of
Doctor of Philosophy

by

Daniel L. Gillaugh
B.S.M.E., Wright State University, 2010
M.S., The Ohio State University, 2012

2019
Wright State University

Wright State University
Graduate School

May 7, 2019

I HEREBY RECOMMEND THAT THE DISSERTATION PREPARED UNDER MY SUPERVISION BY Daniel L. Gillaugh ENTITLED As-Manufactured Modeling of a Mistuned Turbine Engine Compressor Evaluated Against Experimental Approaches BE ACCEPTED IN PARTIAL FULFILLMENT OF THE REQUIREMENTS FOR THE DEGREE OF Doctor of Philosophy.

Joseph C. Slater, Ph.D., P.E.
Dissertation Director

Mary E. Fendley, Ph.D.
Interim Director, Ph.D. in Engineering Program

Barry Milligan, Ph.D.
Interim Dean of the Graduate School

Committee on
Final Examination

Joseph C. Slater, Ph.D.,P.E.

J. Mitch Wolf, Ph.D.

Harok Bae, Ph.D.

Richard G. Cobb, Ph.D.

Jeffrey M. Brown, Ph.D.

ABSTRACT

Gillaugh, Daniel L. Phd, Department of Mechanical and Materials Engineering, Wright State Uni-versity, 2019. *As-Manufactured Modeling of a Mistuned Turbine Engine Compressor Evaluated Against Experimental Approaches.*

As-manufactured rotors behave quite differently than nominal, as-designed rotors due to small geometric and material property deviations in the rotor, referred to as mistuning. Traditional integrally bladed rotor (IBR) modeling approaches assume each blade is identical. State-of-the-art IBR dynamic response predictions can be accomplished using as-manufactured models (AMM) generated via optical topography measurements and mesh morphing. As-manufactured models account for geometric deviations occurring through the machining process, material deviations and field wear, allowing each blade to respond differently. Rotor designs are intended to avoid resonance crossings throughout an engine's operating range, but total avoidance is challenging. This has led to conservative designs as well as heavily instrumented rig and engine testing to attempt to reduce future HCF issues, debiting aircraft performance while increasing development costs. Therefore, it is vital that accurate modeling approaches predict the forced response of resonance crossings to capture mistuning phenomenon and to place safety instrumentation appropriately.

Safe engine operation is ensured by setting safety limits on rotor airfoil mounted strain gages that monitor the dynamic response of the component. Traditionally, strain gage limits are generated utilizing geometry obtained from an "as-designed nominal model where finite element analysis is used to compute the static and modal s tresses. Predicted modal stresses of the cyclic analysis are used to optimize strain gage locations to ensure modal observational coverage, modal identification, and maximum vibrational stress for each mode. Strain gage limits are then produced for these optimal strain gage locations on the tuned finite element model. The described nominal geometry based process is subject to errors associated with airfoil mode shape variations caused by manufacturing deviations. This work develops a new process based on as-manufactured geometry measurements that obtains

more accurate strain gage limits. It is shown that, due to the variability of blade-to-blade geometry, strain gage limits can vary significantly between blades. This is demonstrated by analyzing a mistuned IBR on a sector by sector basis. The developed approach has the capability to more accurately place gages on responsive blades to ensure safe engine operation during testing.

Although blade mounted strain gages are vital during rig and engine development to ensure safe engine operation, they also enable a change in dynamics of IBRs. The mistuning of a 20 bladed IBR is evaluated via analytical methods, benchtop testing, and using a rotating compressor research facility. The resonant response of the IBR at various modes and harmonic excitations is investigated in this work. Two AMM finite element models (FEM) are created of a 20 bladed IBR. One FEM has no strain gages present, where the second FEM includes strain gages on six blades. Traditionally, strain gages and lead wires are treated as the same material property as the IBR itself. It will be shown that the inclusion of strain gages in AMMs using this method changes the IBRs predicted mistuning. An alternative AMM approach is developed that changes the material properties of the finite elements attributed to the strain gages. The predicted mistuning for each AMM is accomplished using the Fundamental Mistuning Model (FMM ID), where the predicted mistuning will be compared to both Traveling Wave Excitation (TWE) experiments and a rotating compressor rig. Findings show mistuning predictions of the non-strain gaged AMM compare far better to the experiments compared to the inclusion of the strain gages in the AMM. Additionally, altering material properties of the strain gages in the AMM improves mistuning prediction compared to treating the strain gages as the parent IBR material. The work herein supports the recommendations that AMM should be acquired using clean, non-strain gaged rotors or the material properties of strain gaged elements need to be altered to more accurately model the component. This body of work ultimately shows the importance and ability to use AMM approaches to significantly increase the fidelity of understanding of turbine engines from both a component and system level.

List of Acronyms

$AFRL$	Air Force Research Laboratory
AMM	As-Manufactured Model
B	Blades
BTT	Blade Tip Timing
CAD	Computer Aided Design
$CARL$	Compressor Aero Research Laboratory
CFD	Computational Fluid Dynamics
CMM	Coordinate Measurement Machine
CMS	Component Mode Synthesis
DOD	Domestic Object Damage
DOF	Degree of Freedom
EO	Engine Order
FEA	Finite Element Analysis
FEM	Finite Element Model
FMM	Fundamental Mistuning Model
FOD	Foreign Object Damage
FRA	Forced Response Analysis
GMM	Geometrically Mistuned Model
HCF	High Cycle Fatigue
HPC	High Pressure Compressor
IBR	Integrally Bladed Rotor
ICP	Iterative Closest Point
LCF	Low Cycle Fatigue
$MMDA$	Modified Modal Domain Approach
$MORPH$	Intelligent Mesh Morphing Method
PCA	Principal Component Analysis
PBS	Parametric Blade Study
N	Number of Blades
ND	Nodal Diameter
$NSMS$	Non-intrusive Stress Measurement System
ROM	Reduced Order Model
$SDOF$	Single Degree of Freedom
$SWAT$	Sine Wave analysis Technique
SNM	Subset of Nominal Modes
TAF	Tuned Absorber Factor
$TEFF$	Turbine Engine Fatigue Facility
TWE	Traveling Wave Excitation

List of Symbols

C	Engine Order
F	Complex Force
f_s	Modal Scale Factor
G_e	Goodman Envelope
Q	Damping
R	Pearson Correlation Coefficient
r_{sg}	Strain Gage Ratio
s	Blade Number
σ_v	Von Mises Stress
σ_s	Steady Stress
$\sigma_{\nu_{max}}$	Maximum Vibratory Stress
U	Displacement Vector
ω	Natural Frequency

Contents

List of Figures

List of Tables

Acknowledgment

First, I would like to take this opportunity to thank Dr. Joseph Slater for his support and guidance throughout the journey that has been this dissertation. He was influential in the successful completion of this work, and I look forward to continued research and collaboration.

I would like to also thank my committee members: Dr. Mitch Wolff, Dr. Harok Bae, Dr. Richard Cobb, and Dr. Jeffrey Brown. Their feedback and influence helped mold this research into a more complete work.

I would like to thank the Air Force Research Laboratory's (AFRL) Engine Integrity Branch under the direction of Ms. Kathleen Sargent for allowing me the opportunity to pursue this research. Having the ability to tie my research to Air Force needs enabled increased motivation and desire throughout this process.

I would like to thank AFRL's Turbine Engine Fatigue Facility (TEFF) for the use of benchttop experimental facilities to enable this work. Dr. Tommy George, Dr. Onome Scott-Emuakpor, Dr. Casey Holeycross, Bryan Langley, Trevor Tomlin, Angie Still, and Philip Johnson played critical roles in the setup and collection of data using the Traveling Wave Excitation System and ATOS machines. Additionally, I would like to thank AFRL's Compressor Aero Research Laboratory (CARL) for the opportunity to collaborate with their team to collect rotating tip deflection data that also played a critical role in the success of this research. Mr. Chase Nesslar, Mr. Timothy Janczewski, Mr. Tom McCray, and Mr. Terry Norris spent countless hours with me in the test cell to ensure I collected the necessary data to provide effective comparisons of the experiment to our as-manufactured models. These two facilities enabled me to obtain data not capable of collecting in very many places in the world.

I would like to thank Dr. Jeffrey Brown, Dr. Joseph Beck, Mr. Alex Kaszynski, and Ms. Emily Carper for their analytical expertise and continued support throughout the as-manufactured modeling process. Their knowledge, friendship, guidance, and support

throughout this PhD program has made the road that much easier.

I would like to thank my Mom and Dad for their emotional and financial support throughout the combined 13 years I have been undergoing some form of college education. Without their backing, this milestone would have had a much steeper path.

Most importantly, I would like to thank my wife, Annie. Her steadfast love and support throughout this journey has been amazing. An apartment, two houses, one entire home remodel, and three beautiful children later, we deserve a new sense of normalcy. I'm excited to begin this next chapter with you and the kids.

Dedicated to

Lillian, 4
Luke, 2
James, 1

Introduction

1.1 Turbine Engine Background

The turbine engine has been the foundational means for the creation of thrust and power for decades. It has revolutionized both the commercial and military worlds by continual modifications and improvements to help airplanes go further and faster more efficiently. Turbine engines consist of a combination of both stationary and rotating components. A cross section of a typical turbine engine can be found in Figure 1.1. At its core, the turbine engine consists of a compression, combustion, and expansion cycle. The compression systems function is to compress incoming air to a high pressure. Fuel is then mixed with the high pressure air in the combustor and burned to produce a high pressure, high velocity gas. The turbine system extracts the energy from this gas to produce power. This power is then used to drive the compressive system, to produce thrust, or to generate torque for other applications.

Turbine engines are subject to strenuous and varying environments with high temperatures, pressures, vibratory and centripetal loads imparted on each component. These conditions must be accounted for in the challenging endeavor of designing a high performance yet durable turbine engine. Detailed analyses must be performed to consider the interaction of aerodynamics, thermodynamics, aeromechanics, and rotordynamics to ensure turbine engines are capable of withstanding thousands of hours of usage. Increased

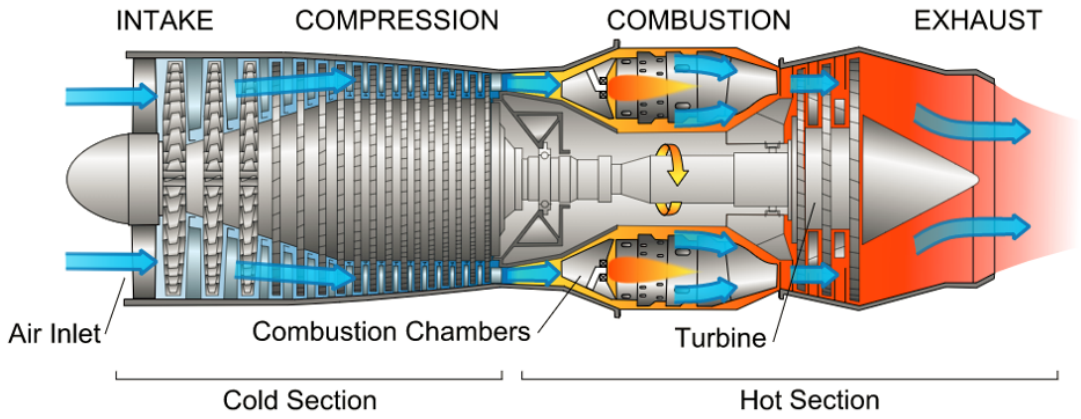

Figure 1.1: Turbine Engine [1].

turbine engine efficiency and performance goals drives designs to reduce weight without compromising durability. This increases the already challenging endeavor of designing a turbine engine to withstand failures.

Predominant failure mechanisms in turbine engine blades consist of low cycle fatigue (LCF), high cycle fatigue (HCF), creep, thermomechanical fatigue, environmental problems (oxidation/corrosion), foreign object damage (FOD), domestic object damage (DOD), or a combination. LCF is caused by relatively high cyclic loads that induce plastic strain during each cycle causing failures in 10,000 cycles or less. Conversely, HCF is caused by relatively low cyclic loads and strains confined largely to the elastic range causing failures in greater than 10,000 cycles. Creep can be experienced by hot section components that encounter high temperatures with sustained loads for an extended period of time potentially leading to excessive deflection or fracture. Thermomechanical fatigue is associated with thermal stresses and could initiate cracks if they exceed the material yield stress. Environmental problems like oxidation and corrosion can effect hot section components like airfoil and turbine blades/stators and combustors when the hot gas reacts with the component material. FOD/DOD occurs due to impact damage from birds, ice ingestion or from domestic parts that become liberated during engine operation. The majority of these failure modes occur slowly over time and can be identified using engine maintenance routines such as

engine overhauls and on-wing inspections. The goal of these maintenance inspections is to identify components that fail inspection criteria and to replace or repair those components to continue successful turbine engine operation in the aircraft. However, the failure mode of HCF has the potential to impart cycles on components rapidly causing failures in relatively short periods of time. HCF has been the subject of research for decades and is a significant focus of this research.

1.2 High Cycle Fatigue

The problem of HCF in turbine engines is pervasive in that it can affect both rotating and stationary components. As of 1996, HCF was the single largest cause of component failures in modern military gas turbine engines, accounting for 24% of failures [2]. The substantial maintenance costs associated with HCF as well as the reduced operational readiness of aircraft led to a significant time and resource investment to better understand HCF. Improvements have been made to reduce occurrences; however, HCF continues to be an issue even today. Current and future engine programs continue to push the state-of-the-art to increase both efficiency and performance while attempting to improve durability and reliability. These improvements led to integrally bladed rotors (IBR) with higher pressure ratio fans and compressors that increase loading on each stage, increase modal density in the operating range, increase mistuning, and reduce the blade damping. Each of these scenarios could be indicators of potential HCF problems.

HCF failures can be induced by a number of potential drivers including mechanical vibrations, airfoil flutter, acoustic fatigue, and aerodynamic excitations. Mechanically induced HCF is due to rotor imbalance that has the capability to affect all aspects of the turbine engine. Current rotordynamic design practices are instituted to avoid detrimental critical speeds induced by rotor imbalance. These practices include built-in margin to account for modeling errors and other unknowns. Airfoil flutter is an asynchronous vibration

phenomenon as a result of unsteady aerodynamic forces created due to blade displacement causing aeromechanical instability that affects blades alone. Although a significant amount of research is yet to be done, computational fluid dynamics (CFD) advancements have enabled the prediction of flutter and have compared well with experimental tests [3–5]. Acoustic fatigue mainly affects the combustor, nozzles, and augmentor and is not subject to the research associated with this effort. Common sources of aerodynamic excitations include stator vanes, support struts, inlet distortion patterns, or a combination that create pressure perturbations that can affect blades and vanes alike, where HCF failures driven by aerodynamic drivers is the primary subject of this research.

It is an industry standard practice to assess HCF risks in components. Three-dimensional finite element models (FEMs) are created to predict airfoil resonances, steady and vibratory stresses. An airfoil's resonant frequencies are determined using the component's geometry, material properties, and boundary conditions. Predicted component resonances are compared with integral engine order (EO) drivers using a Campbell diagram (Figure 1.2). A Campbell diagram uses the potential EO excitations along with the predicted system modes as a function of engine rpm to determine potential resonance crossings. Designers attempt to evade resonance crossings throughout the engine operating range to avoid potential HCF issues, but total avoidance of EO excitations is challenging. The introduction of low-aspect ratio blades and their inherent high modal densities make the avoidance of resonance crossings even more challenging. HCF margin is then assesed by plotting the steady stress as a function of the vibratory stress using the modified Goodman diagram (Figure 1.3). The modified Goodman diagram is constructed for a constant design life, typically 10^7 cycles. The x-axis is the steady stress from centrifugal forces, where the y-axis is the vibratory or alternating stress. The Goodman line is generated between the material's endurance limit and the ultimate strength as seen in Figure 1.3. An additional constraint can be imposed by employing a secondary constraint connecting the material's yield strength on the x-axis to the material's yield strength on the y-axis. Furthermore, an additional safety factor is

used by utilizing the 60% Goodman line as the limiting constraint. This accounts for uncertainties in the design process such as material properties and mistuning. A component condition under the 60% Goodman line is determined safe from HCF for up to the number of cycles that diagram was constructed for. To properly determine if a component is safe from HCF, the vibratory stress of that component needs to be evaluated using forced response analyses. The potential ramifications of HCF issues in fleets compound the importance of accurate HCF predictions in turbomachinery components, specifically the largest risk area of rotating airfoils, which is the primary focus of this research.

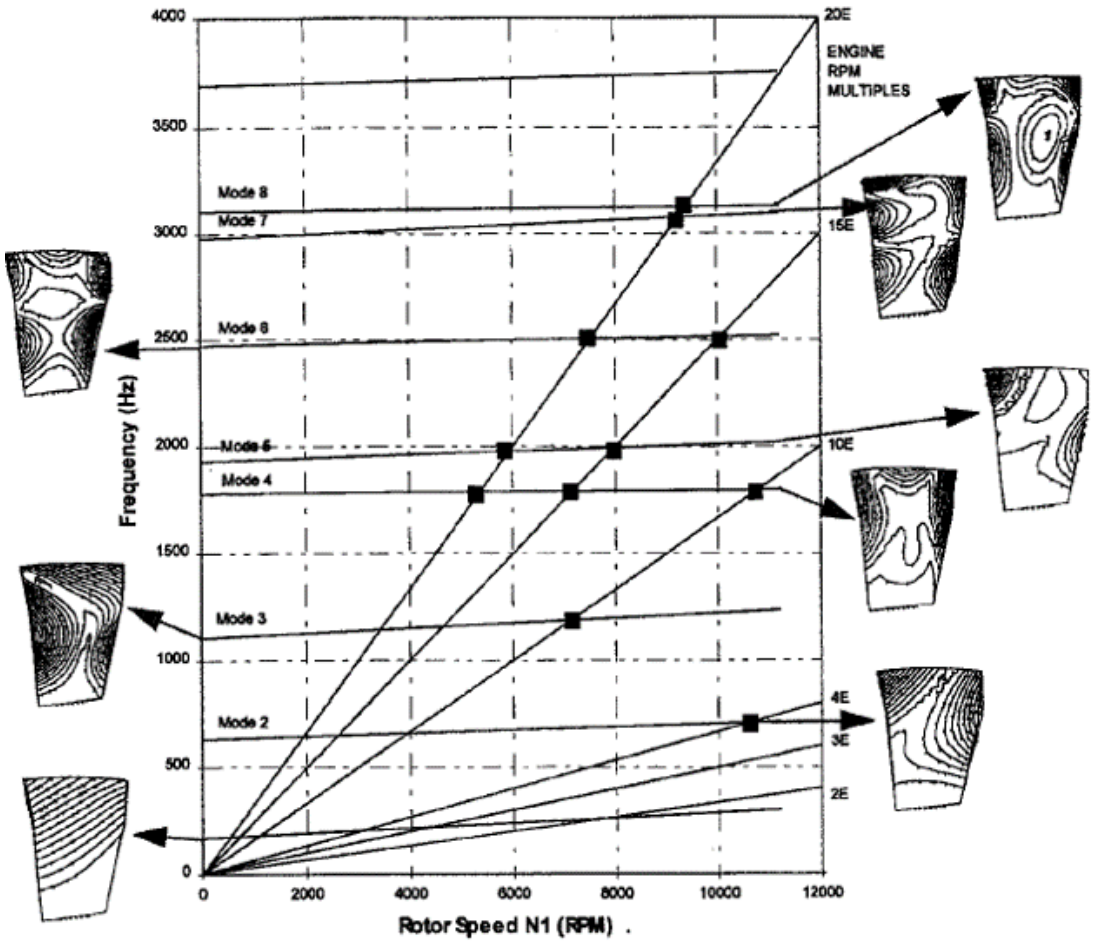

Figure 1.2: Example Campbell Diagram [2].

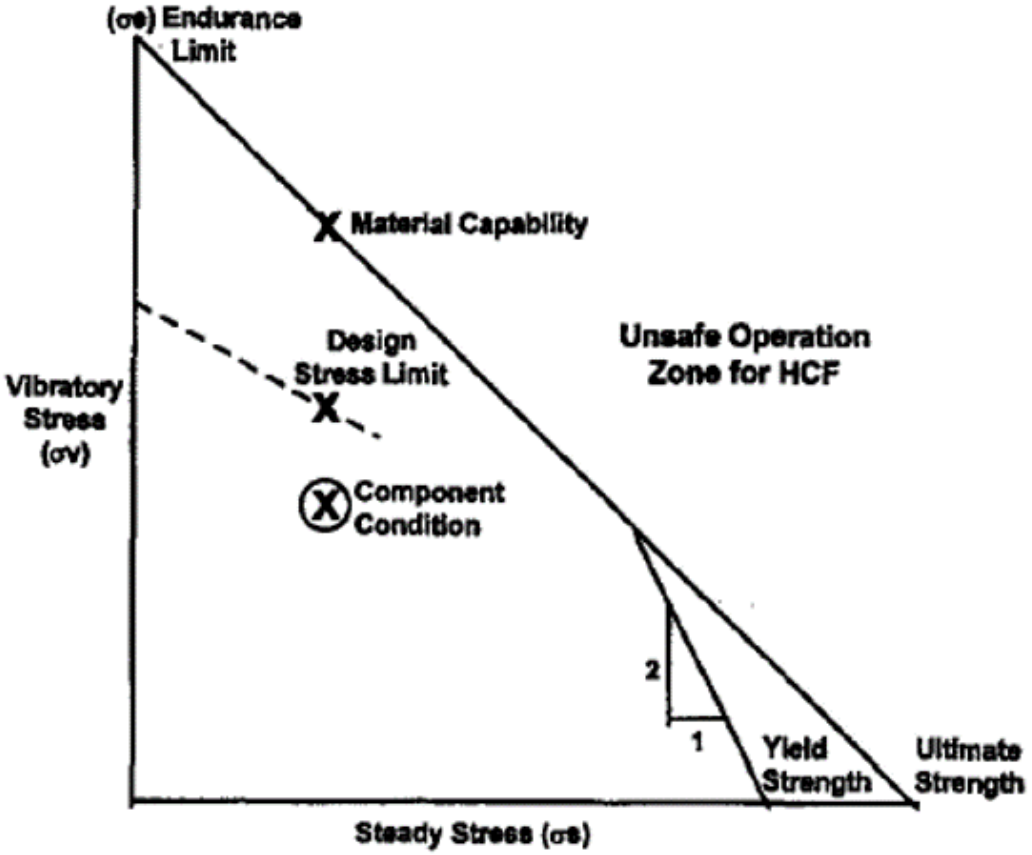

Figure 1.3: Modified Goodman Diagram [2].

1.3 Airfoil Forced Response

Airfoil forced response is caused primarily by the interaction of unsteady aerodynamic forces with the rotating airfoils. These aerodynamic forces produce harmonic excitation forces on each airfoil via upstream and downstream components as well as inlet swirl and distortion patterns. A blade resonant response occurs when the frequency of these aerodynamic harmonic excitations coincide with the airfoil's natural frequency, which are indicated by the potential crossings in a Campbell diagram like in Figure 1.2. Forced response analysis needs to be conducted for potential resonance crossings to determine the resonant stress of the airfoils. The magnitude of the blade's stress is a function of system damping as well as modal loading. System damping is a function the material properties, material interfaces, and aerodynamic damping. There exist two different types of rotors: blade

inserted rotors and integrally bladed rotors (IBR). Inserted blades inherently have more system damping due to the frictional interface between the blade and the disk. However, IBR's are integrally machined as one complete rotor which greatly reduces the damping in the component, leading to a larger blade forced response if excited. The modal loading on the airfoils are a combination between the vibrating blade inducing a motion dependent unsteady aero load and the blade experiencing flow effects as it passes through symmetric pressure gradients inducing a displacement independent unsteady aero load. Computational fluid dynamics (CFD) is needed to perform the forcing and damping calculations, which needs to be coupled with a structural FEM to produce an accurate HCF stress prediction. A schematic outlining the HCF stress prediction process can be found in Figure 1.4.

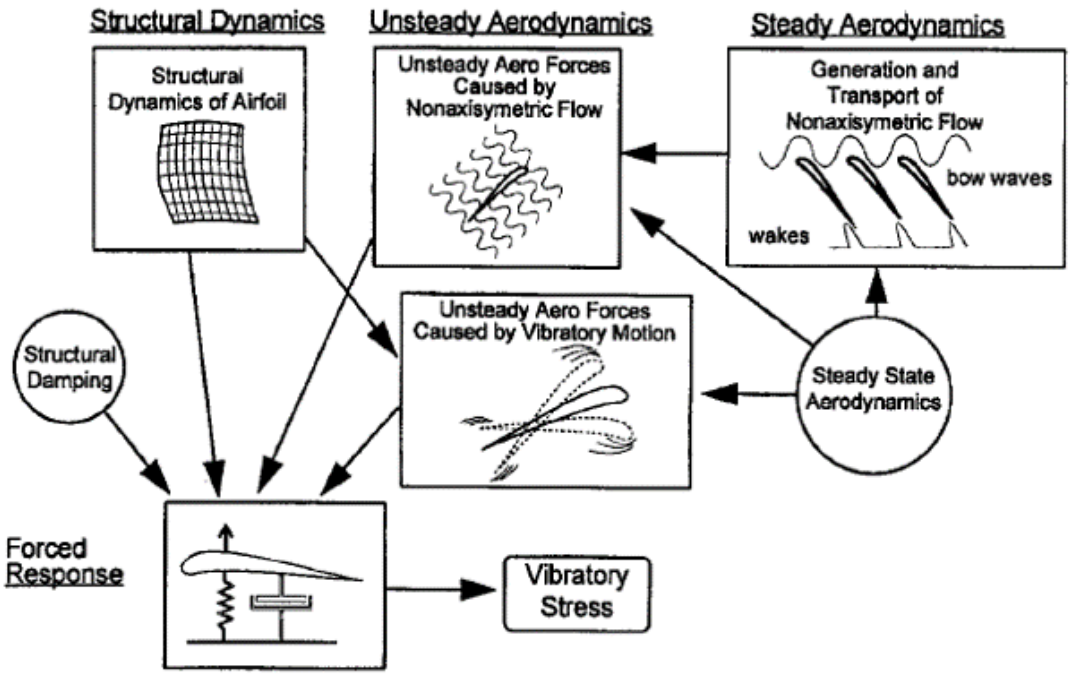

Figure 1.4: HCF Stress Prediction Outline [2].

Traditionally, the computational time and expense to perform a fluid/structure interaction to predict HCF forced response makes it unfeasible to accomplish early in the design phase. Instead, a certain level of conservatism is placed on the design to reduce the probability of HCF issues. This conservatism can limit the design window, impacting aircraft

performance and cost. Lack of detailed understanding of HCF response early in the design phase requires heavily instrumented rig and engine demonstrations to demonstrate durability or to discover detrimental modes. These engine/rig demonstrator rigs can be instrumented with both strain gages and blade tip timing probes that are capable of monitoring the state of stress in a component. Safety limits are set on these sensors in terms of a strain gage limit or a deflection limit in order to ensure safe operation. Unfortunately, if a design flaw is discovered at this stage of an engine development program, it requires costly and time consuming changes. Therefore, improvements in both the understanding and prediction of HCF response early in the design phase are needed to reduce engine development and maintenance costs while potentially increasing the design window for blade designers, leading to more efficient/reliable turbine engines. Recent advancements in computational resources and modeling approaches make implementing an "HCF check" early in the design phase an achievable goal.

1.4 Mistuning

The traditional approach for modeling IBRs for HCF predictions assumes nominal part geometries, i.e., each blade is identical to each and every blade. An ideally cyclically symmetric rotor would respond at only the tuned system modes that resonate at the corresponding EO excitation. However, actual manufactured rotors perform quite differently due to small differences in geometric and material characteristics of individual blades, referred to as mistuning [6]. The machining process, material deviations, and field wear allow for each blade to have varying properties and thus varying natural frequencies and responses that could lead to mistuning and the confinement of vibrational energy to an individual blade known as mode localization [7]. Figure 1.5 shows an example of mode localization. The tuned IBR response is shown on the left in Figure 1.5 with an even distribution of energy throughout the blades. However, the mistuned IBR response is shown on the right

in Figure 1.5 with energy localized in a single blade region. The localization of energy in a single blade results in increased resonant responses referred to as mistuning amplification, potentially resulting in higher risk of HCF failure. An example of mistuning amplification is shown in Figure 1.6, where the tuned response is represented with the dotted line, and the individual mistuned blade responses are represented with the solid lines. It can be seen that several blades respond with higher amplitudes than the tuned response. There exists a need for physics-based models to predict mistuned rotor response as well as an increased need to validate these models to operational rigs and engines. This work presents a direct response to this need by utilizing advanced modeling techniques using as-manufactured models to predict mistuned rotor response and validating these approaches using benchtop experiments and compressor rigs.

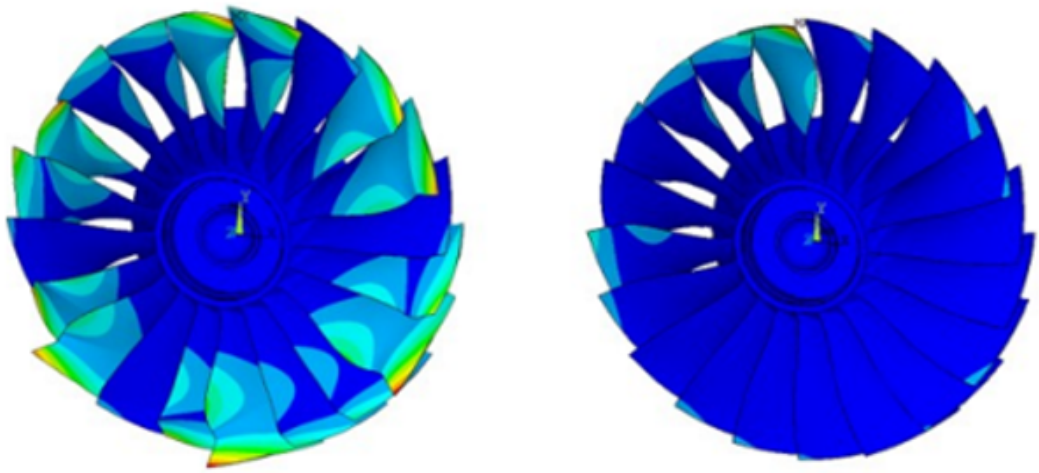

Figure 1.5: Tuned and Mistuned IBR Response.

1.5 As-Manufactured Models

It has been stated that traditional approaches for modeling IBRs use nominal or tuned models where each blade is assumed to be identical. An alternative to using a tuned FEM is to

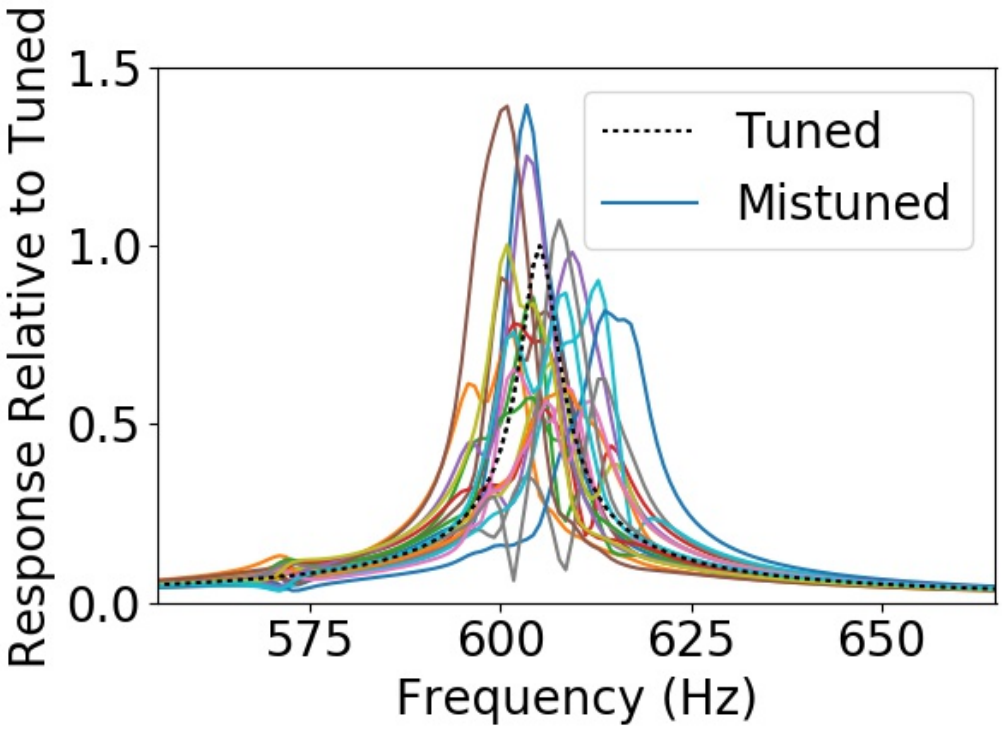

Figure 1.6: Mistuning Amplification of a 20 Blade IBR.

use numerical modeling to create an as-manufactured FEM that accounts for geometric differences. Significant research has been conducted on utilizing reverse engineered physics-based models to predict responses based on coordinate measurement machine points or optically-scanned geometry, i.e., as-manufactured models [8–10]. Using as-manufactured models allows for the calculation of frequency mistuning patterns and forced response directly from a finite element model (FEM). As-manufactured FEMs can be created for both newly machined components and components that have been in service undergoing degradation from engine wear, allowing for IBRs to be analyzed throughout their life-cycle. Further, it has been shown that accounting for the geometric blade-to-blade variation via as-manufactured FEMs illustrates a large variation in sensor response and placement of safety instrumentation, i.e., strain gages and tip timing probes [11, 12]. Hence, as-manufactured models have the potential to be utilized for not only mistuning identification, but also higher

fidelity sensor placement, more accurate computationally fluid dynamic (CFD) simulations for turbines and compressors [13, 14], and a suite of other possibilities, representing a dramatic increase in knowledge for the turbine engine community. This works aims to show the ability to use as-manufactured models to accurately predict mistuning patterns and mistuned rotor response using a combination of as-manufactured FEMs, benchtop experiments, and rotating compressor rigs.

1.6 Overview of the Dissertation

This dissertation is laid out in the following manner: Chapter 2 covers a literature review of reduced order models (ROM) for mistuning, as-manufactured models (AMM), mistuning identification methods, and a review of mistuning comparison studies between ROMs, AMMs, and experiments. The purpose of this review is to highlight the research gap that is addressed in this document. These gaps are addressed in Chapter 3 which focuses the research needs and contributions of this work. Chapter 4 illustrates how to develop more accurate strain gage limits and locations using as-manufactured modeling on a turbine engine compressor. Chapter 5 utilizes the as-manufactured models developed in Chapter 4 to compare as-manufactured modeling of this compressor against multiple experimental approaches. Particularly, this chapter shows the importance and ability to use as-manufactured models to help increase detailed understanding of aerospace systems and to have the ability to have increased confidence in these models. Chapter 6 further builds on the previous chapters' findings to demonstrate the negative impact treating strain gages as the parent rotor material has on mistuning predictions when developing as-manufactured models. A modeling approach is developed to more effectively model strain gages in turbomachinery applications that improves model fidelity. Lastly, Chapter 7 provides a brief conclusion of the document.

Literature Review

Mistuning has been studied for decades. The high cost and ramifications associated with potential HCF failure still make it a high interest across the turbine engine community even today. The following chapter provides a detailed literature review of the subject. Section 2.1 provides a review of reduced order models (ROMs) used to predict mistuning patterns and amplifications. A subset of these ROMs will be used as a tool to evaluate mistuning using various experimental and analytical methods. This will be followed by a discussion in Section 2.2 on as-manufactured models and how advancements in reverse-engineering methods and mesh morphing enable a purely analytical mistuning identification method. Next, mistuning identification methods will be discussed in Section 2.3. These methods consist of both experimental methods as well as ROMs to use in conjunction with experimental data to determine an IBR's mistuning. Lastly, Section 2.4 reviews comparison studies between mistuning predictions and experimental measurements.

2.1 Reduced Order Models for Mistuning

Reduced-order modeling approaches for predicting mistuning patterns and amplifications and the potential for HCF continue to make advancements. Thorough reviews of the subject have been conducted by Slater, et al. [15] and Castanier and Pierre [6]. This review seeks to provide a brief review of these works as well as introduce recent ROM advancements in the last decade.

2.1.1 Lumped Parameter Models

Early mistuning research began with lumped parameter models where bladed disks were modeled as cyclic chains of spring-mass oscillators [6]. The mistuning for these models was implemented by varying the stiffness parameter of the blades. Lumped parameter models present a beneficial means to model mistuning trends and can be easily applied to perform statistical investigations [16–22]. To more accurately predict the mistuning associated with an actual rotor, finite element models present a better solution over the basic lumped parameter models. Finite element models allow the blade and disk to be modeled together rather than introducing a coupling parameter. A full IBR model is needed to sufficiently capture the mistuning of a given IBR, which can lead to lengthy solve times, especially when analyzing simulated fleets of rotors. This led to reduced order models (ROM) generated from a parent FEM.

2.1.2 Component Mode Methods

Component mode synthesis (CMS) is one of the very first ROMs developed [23, 24] that allows for the prediction of mistuning of a full IBR by calculating the modes of each component individually, reducing the DOF of the system. This allows each blade and disk to be components to obtain each individual blades natural frequency, enabling the modeling of mistuning. Certain compatibility conditions are then used at the disk interfaces to form a system model of the IBR. Ramifications associated with early CMS approaches [23–25] were that they needed constraint modes, increasing the DOF of the models and making it difficult to run computationally efficient Monte Carlo simulations. To increase the computational efficiency of these models, even lower-order models were created by Castanier, et al. using REDUCE [26] by eliminating constraint modes. REDUCE models a single disk-blade sector with a massless blade attached to the disk and allows for the addition of mistuning by varying the stiffness parameter of the blade. After adjusting values for the nominal

blade modal stiffness, it was shown that the REDUCE ROM was able to capture the physics associated with the FEM. Bladh et al. was able to condense the DOF of ROMs further by using a cyclic Craig-Bampton model followed by classical modal analysis of the full Craig-Bampton model - Secondary modal analysis reduction technique (SMART) [27, 28]. The authors found that SMART was very computationally inexpensive compared to the mistuning projection method that performs a classical modal analysis on the full FEM and then project each blade's mistuning onto the cyclic system modes.

2.1.3 System Mode Methods

System mode based methods present an alternative to component based methods. Yang and Griffin developed the subset of nominal modes (SNM) method that no longer required component modes as in the CMS methods [29, 30]. SNM, or modal domain analysis (MDA), treats the blade and disk as a single structure instead of components as previously discusses. The authors use nominal system modes to predict the mistuned modes using a subset of the nominal modes, i.e. mistuned modes are a linear combination of tuned system modes. These tuned system modes can be determined from an FEM model for each nodal diameter to then input into the SNM model. The ROM developed works well with blade dominant modes where most of the strain energy presides in the blade itself, and mistuning is introduced to the ROM by changing the stiffness matrix of the blade. As the mistuning of the model diminishes, SNM predictions equal the tuned FEM results. The SNM model was able to accurately predict both mistuned frequencies/mode shapes as well as the forced response of an academic model. Feiner and Griffin extended SNM for a single isolated family of blade-dominant modes using a fundamental mistuning model (FMM) [31]. FMM is a very efficient ROM of mistuning that operates under the assumption of an isolated model family, thereby reducing prediction inputs to the tuned system frequencies and the frequency deviations of each blade. Errors from measurement variation can be reduced by using several system modes from the same family. Moreover, mistuning amplification

can be predicted using the predicted tuned system frequencies, sector frequency deviations, EO driver, and an assumed damping ratio. FMM predicted good agreement for both an academic rotor as well as a more traditional rotor. It will be shown later how FMM can be used as a mistuning identification method [32, 33]. Lim et al. formulated a method called component mode mistuning (CMM) that uses a combination of both tuned system modes as well as virtual blade mistuning components [34]. The authors developed two formulations: considering large and small mistuning, where the small mistuning ROM is denoted CMM that uses a FEM of a tuned sector and a tuned cantilevered blade. Mistuning was implemented into the model via the stiffness matrix. This method was validated against both proportional and non-proportional mistuning. The proportional mistuning case worked well considering only a single eigenvalue mistuning pattern. The non-proportional case when multiple blade-dominant modes are present the mistuning values were needed. Each of the system based reduced-order models (SNM, FMM, CMM) are developed in tuned system modal coordinates, allowing the implementation of aerodynamic coupling that will be discussed later in this chapter.

2.1.4 Geometric Mistuning Methods

The approaches outlined thus far have made assumptions that a mistuned modal response could be approximated using a linear summation of the tuned system modal response. Mistuning was implemented into the ROMs by changing the stiffness matrix causing a uniform shift in the blade's frequencies or by projecting the mistuning onto tuned modes causing non-proportional frequency mistuning. These are frequency based methods and all potential variations (geometric or material properties) only change an airfoil's natural frequency and therefore do not take into account changes in an airfoil's mode shapes. Brown et al. developed a ROM to predict geometric effects on blade-alone forced response using a principal component analysis (PCA) approach to reduce the number of geometric parameters [35]. The geometric deviations for an industrial IBR were measured using a coordinate

measurement machine (CMM) and full FEMs of these as-measured models were developed to assess sensitivity to variations from the nominal rotor. Brown found significant variations on frequency, and additionally found that mode shape variations accounted for large variations in the forced response. Sinha et al. used proper orthogonal decomposition to show that vibratory parameters of a blade can be taken from CMM data [8]. Not accounting for mode shape has the potential to create significant error in predictions [35–37] and should be accounted for using geometric reduced order modeling methods.

Sinha further refined the MDA (or SNM) model to account for geometric perturbations using only important POD features as basis functions [8, 38–40]. This refined MDA modeling method is called the modified modal domain approach (MMDA) and performed perturbations in both the mass and stiffness matrices of blades. It was shown to accurately predict mistuned frequencies, mistuned mode shapes, and forced response of a academic model with geometric mistuning. Madden et al. uses a pristine-rogue-interface modal expansion (PRIME) along with a CMM extension that is capable of modeling both large and small mistuning [41]. Baek et al. developed an extension to CMM, PRIME, and MMDA using only sector-level calculations, providing increased computational savings [42]. The authors predicted natural frequencies and forced response results that agreed well with an academic blisk model.

Beck et al. developed a ROM defined as the Modal Analysis for Geometric Mistuning Analyses (MAGMA) that eliminates the use of tuned airfoil modes and their corresponding errors in forced response predictions [43, 44]. The authors used secondary modal analysis on different submatrices of a parent Craig-Bampton CMS method with two different approaches possible: computed interface modes of the ROM constraint DOF or computed ancillary modes of the constraint and disk fixed-interface normal modes, where the modes could be either tuned or mistuned. It was found that accurate approximations were possible for both high and low responding rotors while reducing solution times compared to traditional CMS ROMs. MAGMA also showed improved accuracy for peak IBR response and

airfoil-to-airfoil predictions compared to traditional frequency based approaches. Beck et al. further refined this method to include a mistuned disk-blade connection and found that including the mistuned interface did not strongly impact the forced response predictions until large perturbations were produced [45].

2.2 As-Manufactured Models

More recently, research has been conducted on utilizing reverse engineered physics-based models to predict responses based on coordinate measurement machine points or optically-scanned geometry, i.e., as-manufactured models [9, 10]. Previously discussed ROMs induce mistuning in IBRs by changing the mass and stiffness matrices of FEM models using the Young's modulus or using specified geometric features. An alternative method is to explicitly model the geometric features of specific components directly via as-manufactured modeling. Using as-manufactured models allows for the calculation of frequency mistuning patterns and forced response for engine specific parts directly from a finite element model. As-manufactured FEMs can be created for both newly machined components and components that have been in service undergoing degradation from engine wear, allowing for IBRs to be analyzed and tracked throughout their life-cycle.

Schoenenborn, et al. used optical measurements to create single airfoil models with simplified blocks at the blade/disk interface [46]. The authors generated 3-D point clouds of an IBR using optical scanning via fringe projection. An optical measurement software was used to separate each airfoil from the disk in a semi-automated manner. Holes in the triangulated surface mesh are present upon completion of this procedure, which are "filled-in" in using quasi geometric partial differential equations from the boundary points and neighbors. The airfoil fillet is closed-in at the root of each blade, and a surface block is extruded at the foot of each airfoil. This block does not represent the disk of the IBR. The end procedure of this method develops airfoil FEMs that represent the actual geometry

of the rotor to a high degree. However, it uses unstructured mesh grids that can present analytical mistuning error. Brajlih, et al. utilized a GOM ATOS™II 3-D optical scanner to perform uncertainty quantifications [47]. The authors performed uncertainty scans of the ATOS™ using three different scan blocks and found scanner uncertainty to be ± 1 thousandth of an inch with a 95% confidence level. Additional studies were completed to examine the effect of spray coatings on the uncertainty of 3-D scanners. Spray coatings are traditionally used to coat parts with high reflectivity, but results indicated that spray coating did not have a significant influence on accuracy. Hönisch, et al. [48] also used optical measurements with fringe projections to develop FEMs of an axial compressor and a turbine blisk for a turbocharger. The actual development of the FEM was not discussed in this work. Paulic, et al. utilized optical scanning to generate a point cloud of a car volume button [49]. The author's had to use a developer spray in order to obtain a successful scan of the part. The commercial solid modeling code SolidWorks was used to generate a solid model based on the surface scan of the part. Developing a model in this method provides an approximation of the original feature, but is not necessarily an exact replica.

Cazenove, et al. [50] also used optical scanning to create a point cloud of an entire IBR. The surface mesh of the IBR was reduced using a GOM Inspect software that significantly reduced the size of the STL file. Features of the IBR that were left with holes were filled using geometry representative of the IBR, where a CAD model was built from the faceted and filled geometry. This process represents the IBR to a high fidelity with a mapped, hexahedral, quadratic mesh to minimize analytical mistuning, but can be very time consuming to generate a full representative as-manufactured CAD model. Schnell, et al. [13] utilized 2-D profile cross-sections of the blades and performed a PCA-based approach to assess manufacturing effects on aerodynamic performance. The authors also developed 3-D CFD FEMs via optical scans of the nine bladed rotor to assess manufacturing effects on performance. Additionally, Schnell, et al. developed simplified FEM simulations of blade only airfoils with no disk for the nine scanned blades. Little insight was

given to how these different as-manufactured FEMs were actually developed. Nyssen, et al. used optical scanning to develop as-manufactured FEMs of a very simple academic structure [51]. Stapelfeldt, et al. demonstrated that accurate flutter predictions could not be made without including identical blade geometries [52].

Kaszynski, et al. developed an automated optical 3-D geometry measurement, measurement, and analysis process for mistuned integrally bladed rotor reverse engineering [9]. The authors collected optical geometry measurements from a transonic IBR to generate a point cloud and then a tessellated surface mesh that was then exported to a reverse engineering software. An assumption was made that the disk of the IBR was uniform to simplify the modeling process, and the surface of each airfoil was created using blade section lines extracted using radial sections. The number of blade sections was optimized for lower order modes in this study, but could be further refined for higher order modes. Upon completion of the solid model creation, a structured hexahedral mesh was generated of the IBR to reduce analytical mistuning. This study proved repeatability of scan data within ± 0.0002 in. Replicated scans were used to demonstrate robustness of the proposed reverse engineering process. This method is referenced in literature as SABRE. Even this semi-automated method presents a time-consuming, tedious task to develop as-manufactured FEM from scan data.

Kaszynski, et al. developed another as-manufactured finite element mesh updating scheme termed an intelligent mesh morphing method (MORPH) [53]. This work developed a reverse engineering process that could be utilized on IBRs at the fleet level, instead of strictly on an academic level. The mistuned FEMs of the IBR were created through optical topography measurement and mesh morphing. The mesh morphing process begins with an optical scanning system that uses structured light and high density charged coupled devices to develop a point cloud geometry that represents the surface coordinates of the as-manufactured IBR. From the point cloud a simple computer aided design (CAD) model of a single, nominal sector is created and discretized into a notional, tuned FEM. The mesh

morphing process updates the tuned FEM nodes to match the tessellated surface data via an iterative closest point procedure. Next, the as-manufactured point cloud is aligned to the tuned FEM via an iterative closest point procedure. The surface nodes of the FEM are then modified to match the tessellated surface data of the point cloud. The outcome of this mesh morphing process is a mistuned FEM that matches the actual as-manufactured geometry of the IBR. Kaszynski, et al. further refined the MORPH algorithm by adding mesh quality verification algorithms and experimental validations [11, 54]. A similar mesh morphing approach was recently developed by Maywald, et al. [10]. The authors begin with a base tuned finite element mesh and project the surface nodes onto the optically measured surface to output a mistuned IBR mesh. The MORPH approach developed by Kaszynski, et al. is the as-manufactured modeling method used to generate the mistuned FEMs in the research herein.

2.3 Mistuning Identification Methods

Analyzing the mistuning of rotors requires the collection of frequency response functions (FRF) of individual blades. Many of the aforementioned methods generate FRFs utilizing forced response analysis techniques via finite element analysis [11, 13]. Experimental techniques are available to generate a rotor's FRF for each blade including modal ping testing, traveling wave excitation (TWE) experiments, and rotating compressor rigs. These systems utilize measuring techniques using laser vibrometers, blade tip timing (BTT), and strain gages to generate the FRFs for each individual blade. The mistuned modes and system frequencies found in the FRFs are then inputs into ROMs to predict a rotor's mistuning by creating analytical models from the experimental (or analytical) results [31–33, 55].

2.3.1 Modal Ping Testing

Modal ping testing is a common method to determine the natural frequencies of components. It can be accomplished using a modal impact hammer or shaker, where the frequency response can be collected using various methods such as accelerometers or laser vibrometers [56, 57]. The drawback with modal ping testing and IBRs is individual blades need to be "de-coupled" from the system to determine an individual blade's natural frequency. Research in the past detuned the system by using additional masses [10, 58, 59]. Each isolated blade is excited using a miniature modal hammer, and the vibration response is measured using a scanning laser vibrometer to obtain each blade's natural frequencies. The frequency deviation is obtained to determine the mistuning pattern, which is then used to update a model by varying Young's Modulus using the mistuning pattern. Results in [58] show that the updated model devleloped using the modal ping testing data captured the general mode localization effects for a particular compressor blisk. Isolating individual blades to determine mistuning patterns provides an adequate representation for lower order modes, but breaks down when there is a significant amount of blade-disk interaction.

2.3.2 Traveling Wave Excitation

Traveling wave excitation (TWE) is a form of experimental testing that simulates an engine order environment. Traveling wave systems have been utilized by both industry and academia to research the mistuning phenomena inherent in turbine engine IBRs [6, 60–62], where additional research investigated IBR vibrational analysis via contact and contactless excitation methods [63, 64]. A typical TWE configuration consists of a stationary rotor, mounting fixture, actuators (electromagnets or acoustic speakers), and components to control the phasing and excitation levels of each actuator positioned under each blade. During traveling wave excitation of the IBR, the frequency response of each airfoil is measured with a scanning laser vibrometer. This enables an ease of input into FMM ID for mistuning

prediction, allowing for a robust means of screening IBRs for mistuning using TWE.

2.3.3 Rotating Compressor Rig

Rotating compressor rigs offer the ability to represent the actual environment of IBRs. The frequency response functions of individual blades can be measured using experimental means such as strain gages or blade tip timing (BTT) methods. Thin film strain gages are applied to airfoils to capture strain information without disturbing the flow field [65]; however, they potentially have the capability to alter the rotor's mistuning [66]. Manwaring, et al.[67] used strain gages to measure the vibratory response of a low aspect ratio transonic fan, which showed blade-to-blade variations at near resonance conditions. Kenyon, et al. [68] investigated mistuning characteristics of a bladed rotor from a two-stage transonic compressor rig using rotor response data taken using strain gages.

A non-intrusive way to obtain a rotor's frequency response is to utilize BTT using non-intrusive stress measurement systems (NSMS). Unlike strain gages, BTT has the capability to measure each blade on an IBR. Most engine and rig tests utilize both strain gages and NSMS on rotor systems as a compliment to one another [69]. Both Heath, et al. [70] and Kharyton, et al. [71] conducted surveys of blade tip-timing measurement techniques for turbomachinery vibration and their advancement in the turbine engine community. NSMS systems have the capability of detecting flutter conditions, cracked blades, mistuning, and static shifts in blade deflections. Additionally, NSMS can be used to determine safety limits to ensure vibration levels of components are below "safe" limits, but is mainly used as an analysis tool to analyze blade vibration data. Besem, et al. [72, 73] utilized a multistage compressor rig to analyze a first torsion mode blade response. Li, et al. [74, 75] used the same multistage compressor rig to analyze force response predictions of various ROMs for a first chordwise bending mode of the embedded compressor stages. The response data from each blade can then be used to perform comparison studies between ROMs, as-manufactured models and experiments.

2.4 Comparison Studies of ROMs & As-Manufactured Models to Experiments

Despite advancements in mistuning ROMs and as-manufactured modeling approaches, there exists a void of studies comparing these analytical methods to real world applications such as rig and engine tests. There have been published studies comparing ROMs such as component mistuning model (CMM) and Fundamental Mistuning Model (FMM) ID to Traveling Wave Excitation (TWE) benchtop experiments that have shown the capability of using these models to determine mistuning in a bladed disk [31, 34, 55, 62]. Feiner and Griffin additionally showed the ability of FMM ID to accurately predict the mistuning pattern of an IBR under rotating conditions in a spin pit using a non-intrusive measurement system (NSMS) [55]. Additional studies have used ROMs to predict the mistuned response of rotating compressors in both single and multistage rigs. Petrov, et al. [76] performed a comparative study between a FEM with computational fluid dynamic (CFD) inputs and a wind tunnel with a full-scale rotating bladed disk and aerodynamic excitation by nozzle guide vanes. The predicted blade responses were on the same order, but showed significant variation between the predictions and the experiments. Besem, et al. [72, 73] conducted a forced response analysis of a first torsion mode in a multistage compressor and found good agreement between the analysis and the experiment for the maximum blade response, but underpredicted the maximum blade amplitudes compared to the experiment. The most recent study by Li, et al. [74, 75] analyzed the forced response predictions using FMM and CMM of a first chordwise bending mode of an embedded multistage compressor. The study found the predicted response has a high sensitivity to small deviations in the blade frequency mistuning patterns and showed that a mistuning problem should be approached in a probabilistic manner.

In addition, there have been several comparisons of FEMs generated using point clouds from optical measurements. Schoenenborn, et al. [46] used optical measurements

to create single airfoil models with simplified blocks at the blade/disk interface and compared to eigenfrequencies determined from isolated modal testing. The general mistuning trend for both a $2F$ and $3F$ mode was predicted well, but there were quantitative differences between the generated FEMs and modal tests. Hönisch, et al. [48] also used optical measurements with fringe projections to develop FEMs of an axial compressor and a turbine blisk for a turbocharger. The actual development of the FEM was not discussed and the predicted sector frequency deviations did not compare well to experimental modal ping testing. Cazenove, et al. [50] also used optical scanning to create a point cloud of an IBR from which they generated a CAD model and then FEM of the blisk. Each blade was isolated in a cantilevered analysis and compared to isolated ping testing, isolated acoustic excitation, and shaker tests with noticeable variations in the blade frequency deviations between each comparison. Schnell, et al. [13] developed simplified FEM simulations of only blade airfoils with no disk for nine scanned blades and found the eigenfrequency scattering due to geometric variability was on the order of ± 3 Hz. Nyssen, et al. [51] used optical scanning to develop as-manufactured FEMs of a simple academic structure from which a mistuning comparison utilizing a ROM developed by Lim [34] was made to experimental electrodynamic shaker tests. Initial mistuning and mode shape comparisons did not relate well and the Young's modulus of the FEMs were also changed to achieve better results. Maywald, et al. [10] utilized an as-manufactured model via mesh morphing to predict the mistuning pattern of an IBR and successfully compared the results to an experiment that isolated individual blades to determine the blade alone frequencies. Kaszynski, et al. [54] showed that a full 360° digital twin model via mesh morphing of an IBR is sufficient in predicting the mistuned response and validated the approach to TWE. The majority of the discussed comparison studies of as-manufactured FEMs are related to isolated modal ping tests or electrodynamic shaker experiments with only a single as-manufactured comparison to TWE experiments. The work presented here seeks to fill a void by providing additional as-manufactured FEM comparison studies to not only isolated modal experiments

and TWE, but also to a rotating compressor rig.

Geometric mistuning model comparison studies discussed in open literature have been between ROMs/benchtop experiments, ROMs/compressor rigs, parametrized FEMs/compressor rigs, and as-manufactured FEMs/benchtop experiments. This work will provide an all-inclusive mistuning evaluation of an IBR comparing as-manufactured models, traveling wave excitation, and a rotating compressor rig with inlet distortion.

2.5 Summary

This chapter discussed open literature research involving mistuning ROMs, AMMs, mistuning identification methods, and a review of comparison studies between ROMs, AMMs, and experiments. The next chapter will focus on the shortfalls addressed and identify the research contributions presented in this work.

Research Contribution

3.1 Research Need

Integrally bladed rotors are designed to be cyclically symmetric where each blade is identical to every other blade. However, as-manufactured rotors do not exhibit this condition due to small geometric and material deviations in the rotor known as mistuning. The machining process, material deviations and field wear allow for each blade to have varying properties and thus varying natural frequencies and responses. Moreover, the introduction of IBRs have created bladed designs with high modal densities in the operating range. This compounds the potential to excite modes when a rotor is subject to harmonic excitations during engine operation, causing resonance and premature failure from high cycle fatigue. Designers attempt to evade resonance crossings throughout the engine operating range to avoid HCF issues, but total avoidance is challenging. This has led to conservative designs as well as heavily instrumented rig and engine testing to attempt to reduce future HCF issues, debiting aircraft performance while increasing development costs. Therefore, it is vital that accurate modeling approaches predict the forced response of resonance crossings.

Both reduced-order modeling approaches and as-manufactured modeling approaches for predicting mistuning patterns and amplifications and the potential for HCF continue to make advancements. Despite these modeling advancements, there exists a void of studies comparing these analytical methods to real world applications such as rig and engine tests. The majority of comparison studies of as-manufactured FEMs are related to isolated modal

ping tests or electrodynamic shaker experiments with only a single as-manufactured comparison to traveling wave excitation experiments (TWE). The work presented here seeks to fill a void by providing additional as-manufactured FEM comparison studies to not only isolated modal experiments and TWE, but also to a rotating rig.

Moreover, the prescribed nominal geometry-based processes for determining not only airfoil stresses but also safety instrumentation (blade tip timing and strain gages) placement and limits is subject to errors associated with airfoil mode shape variations caused by manufacturing deviations. The blade-to-blade variability in an IBR can cause both frequency and mode shape variation that affects both placement and safety limits for critical instrumentation to monitor potential HCF issues. The approach developed in this work develops a process to reduce the errors associated with developing instrumentation placement and limits by utilizing as-manufactured modeling approaches in lieu of the traditional nominal geometry approach.

Further, researchers fail to account for instrumentation embedded in as-manufactured models. Treating the instrumentation (strain gages and wires) as the same parent material as the rotor itself has the potential to negatively impact mistuning and forced response predictions. A better approach to deal with instrumentation in as-manufactured models is by changing the material properties of the instrumentation wires to more closely match reality. This research quantifies the negative impact by developing a modeling strategy to more accurately account for instrumentation using as-manufactured modeling approaches. The developed approach is validated by improving mistuning comparisons between AMMs, TWE, and compressor rigs.

3.2 Research Scope

The defined goal for this body of work is to show that the utilization of as-manufactured modeling significantly increases model fidelity leading to improved mistuning evaluation

capabilities, sensor placement and safety limits, and instrumentation modeling techniques. These added capabilities via as-manufactured modeling are limited by the accuracy of the optical scan of the component; therefore, high quality scans are used in this work. Further, uncertainties are introduced when comparing these as-manufactured modeling approaches to experimental investigations. Diligent experimental test procedures were followed to ensure repeatable test measurements for each analyzed mode. The research contribution associated with this work is an enabler to advance and incorporate as-manufacturing modeling approaches into both design and life-management systems.

3.3 Research Contribution

Chapter 4 develops a new process based on as-manufactured geometry measurements from a high fidelity optical geometry collection system that obtains more accurate strain gage limits. As-manufactured models are utilized to predict modal stresses and frequencies to optimize strain gage locations to ensure modal observational coverage, modal identification, and maximum vibrational stress for each mode. This approach thus captures both frequency and mode shape variation due to geometric deviations between each blade. Strain gage limits are then produced for these optimal strain gage locations, and it is shown that due to the variability of blade-to-blade geometry, strain gage limits can vary significantly between blades. This is demonstrated by analyzing a mistuned IBR on a sector-by-sector bases. The approach developed presents a more accurate means of correctly determining the sensor location with the capability to apply strain gages with satisfactory gage ratios on responsive blades. More importantly, this approach has the potential to set the sensor limits more accurately to avoid scenarios where operation occurs outside the Goodman envelope. This ultimately shows the importance of using as-manufactured models to develop sensor limits.

Chapter 5 provides an all-inclusive mistuning evaluation of an IBR comparing as-

manufactured models, traveling wave excitation, isolated modal testing, and a rotating compressor rig. A geometrically accurate FEM of a 20 bladed IBR was developed using optical scanning and mesh morphing. Experimental and analytical forced response analyses were conducted to analyze three modes with four different drivers. Three experimental methods were utilized. The first is a benchtop TWE that is operated at AFRL in the Turbine Engine Fatigue Facility (TEFF). The second is a benchtop test that isolates the blades experimentally and performs modal testing. The third is a rotating compressor rig at AFRL in the Compressor Aero Research Laboratory (CARL). Analytical forced response simulations were done using the developed as-manufactured models. Approaches were developed to post process experimental data accounting for both isolated modes as well as heavily damped "merged" modes. Mistuning was evaluated using three separate methods: tuned absorber factor (TAF), isolated blades to generate mistuning patterns, and using a reduced-order model called FMM ID. It is shown that TAF shows variability between each method providing indications TAF may not be the best approach of force amplification predictions. Basic mistuning agreements exist when isolating blades both experimentally and analytically exhibiting as-manufactured models are capable of representing full experiments. System ID methods provide a basic agreement between both the mistuning pattern and the mistuning amplification for all three methods analyzed. This ultimately shows the importance and the ability to use as-manufactured models to help increase detailed understanding of aerospace systems and the ability to have increased confidence in these models to determine how rotors will potentially respond during bench, rig, and engine tests. It also illustrates the ability to use as-manufactured models to predict both the mistuning pattern and the mistuning amplification across a broad series of modes.

Chapter 6 will build from the work developed in Chapter 5 by developing a method to account for strain gage instrumentation in as-manufactured models. The AMMs developed in Chapter 5 had strain gages and instrumentation wires embedded in the models. These quantities were treated as the same material as the rotor itself (titanium). Modeling the

instrumentation in this manner skews the mistuning predictions by adding mass/stiffness to certain blades with instrumentation. Chapter 6 compares the results presented in Chapter 5 to an as-manufactured model developed from a clean point-cloud with no strain gages associated with the rotor. It is shown that improved mistuning predictions are developed when no strain gages are present on the AMM; therefore, including instrumentation in the AMM without altering material properties changes the mistuning predictions. An alternative as-manufactured modeling approach is developed that changes the material properties of the finite elements attributed to the strain gages and instrumentation. The mistuning predicted using various as-manufactured models are compared to both stationary and rotating experimental tests, namely TWE experiments and a rotating single stage compressor rig. Additionally, changing the material properties of the strain gages to more accurately represent the instrumentation itself produces a better mistuning prediction of the IBR. An additional comparative study is conducted using TWE of an IBR before and after strain gage application using a soft epoxy resin bonding. The mistuning pattern and mistuning amplification of three different modes (1st bend, 2nd bend, and 1st torsion) are analyzed across multiple engine order excitations. Findings show that the soft epoxy mounted strain gages have the possibility to change the mistuning of an IBR and should be accounted for during development. Therefore, the generation of as-manufactured models using optical scanning should be acquired using a clean, non-strain gaged rotor, and in the case where this is not possible, the finite elements associated with the strain gages and resin need to be modeled using more accurate material properties.

3.4 Summary

Specific contributions of the research are as follows:

Major Contribution 1 Developed a new approach based on as-manufactured FEMs

to create more accurate strain gage limits (Chapter 4)

Minor Contribution 1.1 Performed detailed investigation of mistuned strain gage limit variation compared to nominal limits

Minor Contribution 1.2 Developed approach to utilize as-manufactured FEMs to optimally place strain gages on responsive blades

Major Contribution 2 Conducted all-inclusive mistuning evaluation of an IBR comparing as-manufactured models, traveling wave excitation, isolated modal testing, and a rotating compressor rig (Chapter 5)

Minor Contribution 2.1 Conducted assessment of mistuning characterizations using tuned absorber factor, experimentally isolated blades, and using ROMs

Minor Contribution 2.2 Developed a method to isolate IBR blades for traveling wave excitation experiments

Minor Contribution 2.3 Developed as-manufactured model of rotor simulating the TWE environment

Minor Contribution 2.4 Developed as-manufactured model of rotor simulating rotating rig environment

Major Contribution 3 Performed detailed investigation into the inclusion of instrumentation wires in an as-manufactured FEM on the mistuning prediction of a transonic compressor (Chapter 6)

Minor Contribution 3.1 Developed and investigated as-manufactured model of rotor without strain gages

Minor Contribution 3.2 Developed and investigated as-manufactured model of rotor with strain gages

Minor Contribution 3.3 Developed modeling approach to account for strain gages in as-manufactured model

Minor Contribution 3.4 Conducted detailed investigation of strain gage effect on mistuning using traveling wave excitation experiment

Accurate Strain Gage Limits Through Geometry Mistuning Modeling

Safe engine operation is ensured by setting safety limits on rotor airfoil mounted strain gages that monitor the dynamic response of the component. Traditionally, strain gage limits are generated utilizing geometry obtained from an as-designed nominal model where finite element analysis is used to compute the static and modal stresses. Predicted modal stresses of the cyclic analysis are used to optimize strain gage locations to ensure modal observational coverage, modal identification, and maximum vibrational stress for each mode. Strain gage limits are then produced for these optimal strain gage locations on the tuned finite element model. This described nominal geometry based process is subject to errors associated with airfoil mode shape variations caused by manufacturing deviations. This paper develops a new process based on as-manufactured geometry measurements from a high fidelity optical geometry collection system that obtains more accurate strain gage limits. It will be shown that, due to the variability of blade-to-blade geometry, strain gage limits can vary significantly between blades. This will be demonstrated by analyzing a mistuned IBR on a sector by sector basis. The approach utilized in this paper has the capability to more accurately place gages on responsive blades to ensure safe engine operation during testing.

4.1 Introduction

Turbine engines are comprised of a series of bladed rotors subject to both integral and non-integral vibrations during operation. Common sources driving these vibrations correspond to aerodynamic excitations such as stator vanes, support struts, inlet distortion patterns, or a combination. The potential exists to excite the bladed rotor's natural frequencies when subject to these harmonic excitations, causing resonance and premature failure from high cycle fatigue(HCF) [77]. The issue of HCF is not only very difficult to predict, but it is also one of the costliest, making it of vital importance to the gas turbine engine community[2, 78, 79]. Designers attempt to avoid resonance crossings during engine operation, but total avoidance is challenging. Finite element models (FEM) are used to predict airfoil vibratory stresses due to the potential resonance crossings. It is still necessary to monitor the real-time vibratory stress of these bladed rotors to ensure safe engine operation during testing. This can be accomplished using the traditional approach of blade mounted strain gages by determining the maximum component vibratory stresses using derived ratios from measurement locations to critical locations [80]. Strain gages have been the foundation for real-time health monitoring of rig and engine testing in the turbine engine community for decades.

Finite element models (FEM) are used to determine placement and safety limits for strain gages during engine and rig testing by estimating airfoil mode shapes and natural frequencies [80–82]. Attaining strain information from the FEM corresponding to the strain gage locations can be accomplished via a four node, planar, quadrilateral finite element that accounts for area averaging on the surface of the component [83]. Strain gage placement is a tradeoff between mode identification, mode visibility, data integrity, and geometry to determine optimum locations for measurement [81]. Optimum locations for each strain gage are necessary to limit the number of sensors applied to components while providing complete coverage for multiple modes of vibration using a finite number of gages [84]. Commercially available software is available to optimize gage placement using multiple objective functions: amplitude, misplacement, distance, alignment, and mode ID. The am-

plitude objective refers to the gage ratio ($\varepsilon_{\text{gage}}/\varepsilon_{\text{max}}$) of the sensor, the misplacement objective minimizes the change in sensor ratio with a user defined space, the distance objective ensures sensors are not placed within the user specified distance, the alignment objective aligns sensors within a specified tolerance to an element edge, and the mode ID objective ensures sensors are placed to be able to distinguish between adjacent modes. The goal of a successful strain gage placement is to obtain coverage for all potential system modes in the operating range, to correctly identify which modes are excited, to determine the maximum response of the component for each mode excited, and to obtain clean data from the sensors. Completion of the strain gage placement is culminated by setting appropriate strain gage limits for each gage to ensure safe operation during test.

The classical approach to determine strain gage limits assumes nominal part geometry. In the case of an integrally bladed rotor (IBR), this assumes cyclic symmetry boundary constraints, i.e., each disk-airfoil sector on the IBR is assumed to be identical. An ideal cyclically symmetric rotor would respond at only the tuned system modes that resonate at the corresponding engine order (EO) excitation. However, actual manufactured rotors perform quite differently due to small differences in the geometric and material characteristics of individual blades, referred to as mistuning [6, 43]. Mistuning breaks down the periodicity of the IBR so that an excitation at a single EO will generate a response at multiple adjacent NDs. To account for mistuning, the geometric variation from blade-to-blade needs to be accounted for when determining not only strain gage limits, but also the placement of strain gages on individual blades. Researchers have shown the importance of including the knowledge of airfoil surface geometry variations to show there impact on mode shape variation in addition to variations in airfoil frequency to improve mistuning predictions [35, 43]. Reduced-order modeling approaches have been developed predicting frequency variation and forced response amplification due to mistuning [31–33, 38, 41, 85]. Probabilistic methods have been incorporated to show how mistuning can vary the forced response across a population of IBRs, and Beck et al. [43] provides a good review. Ex-

perimental methods using either compressor rigs or benchtop experiments have quantified mistuning and compared to predictions [31, 34, 62, 72, 73, 76]. Each of these studies emphasizes the importance mistuning plays in the uncertainty of forced response analysis of rotors. This uncertainty should be accounted for when determining instrumentation limits.

Additionally, mistuning via the application of strain gages to airfoils and the associated effect has also been investigated. Typical blade mounted strain gages consist of foil strain gages that are embedded in an epoxy resin or high temperature strain gages embedded in a ceramic cement. It has been shown that the soft epoxy resin does not strongly affect the blade vibrational behavior, where the stiff ceramic cement does have an effect on blade vibrational behavior [66, 86]. When monitoring the airfoil responses of fans and high pressure compressor (HPC) stages with low temperature levels (less than 500 F), foil strain gages with the soft epoxy resin can be used as is the case with this study where a single stage compressor is analyzed. Hence, the application of strain gages should not have a significant impact on the compressors vibrational behavior.

What has not been considered to date is the impact of blade-to-blade geometry variations on the mode shapes used to determine strain gage limits. The author is aware of no published technique or algorithm that accounts for the variation in static and vibrational stress due to mistuning to develop strain gage limits. Utilization of optical 3D geometry measurement, nominal model mesh morphing, and analysis processes allow for the development of an approach to account for the static/vibrational stress variation due to mistuning to more accurately determine strain gage limits and to optimize which blades to instrument [9, 13]. The work herein will show that the strain gage limits based on the nominal cyclic rotor approach can vary widely from limits generated from geometrically mistuned rotors. This will be demonstrated using cyclic sector mistuned FEMs. Previous work demonstrated that it is possible to analyze a mistuned IBR on a sector by sector basis in order to extract blade mode shapes for higher-order modes that are impossible to extract using a full model [87]. This effectively allows for the analysis of each individual mistuned

blade as a tuned IBR with that isolated blades geometry and allows for the extraction of higher order NDs while accounting for geometry that would not be possible using a full mistuned IBR.

This chapter proceeds in the following manner: First, the procedure utilized for conventional strain gage limits will be defined. Second, a short overview of the gage optimization process will be covered. Then conventional strain gage limits will be generated for an experimental rig rotor assuming a nominal, cyclically symmetric integrally bladed rotor. Next, a straightforward approach to extract geometrically mistuned sector based strain gage limits will be presented. This approach has been used in previous work by Kaszynski and Brown to generate blade tip timing limits through geometry mistuning modeling [87]. Lastly, it will be shown how to utilize sensor limit results from a mistuned IBR to better place strain gages. The proposed methodology can be applied to any mistuned rotor to more accurately determine strain gage limits for the mistuned rotor using geometrically mistuned models (GMMs).

4.2 Strain Gage Limit Generation

The process of generating limits can be one of the most time and cost intensive processes in a development phase of a program and errors associated with this process are common due to schedule and cost pressures [84]. This makes the development of a robust method to determine strain gage limits even more vital. This process requires an accurate finite element model (FEM) that represents the test rotors to the highest physical and numerical fidelity possible [88]. The research associated with this effort involves an IBR, but could also be readily applied to inserted blades. Inserted blades have inherit damping due to the interface between the blades and the disk. However, IBRs have minimal damping and, thus, have a strong coupling between blades that form system modes excited by EO excitations that are typically known during the design process of turbine engines. The IBR investigated in

this effort consists of 20 blades and upstream and downstream hardware with the capability to generate EO drivers 1-7 and 31. A Campbell diagram uses the potential EO excitations along with predicted system modes as a function of engine rpm to determine potential resonance crossings. Each potential resonance crossing illustrated on the Campbell diagram should be monitored by strain gages during an engine or rig development program. To generate the Campbell diagram an FEM is utilized, where the traditional FEM approach is to use cyclic symmetric models where every blade on the IBR is assumed to be the exact same with no variations in geometry or material properties. This cyclic assumption allows for the model to be solved for all harmonic indexes for each mode where each harmonic index corresponds to an EO excitation. Each EO driver will excite a specific nodal diameter (ND) on the IBR. A Campbell diagram needs to be generated for each potential ND response since the resonance crossing can vary between ND responses. An example Campbell diagram for the IBR being analyzed in this research is shown in Figure 4.1. The formula to determine the nodal diameter excited given an engine order excitation is

$$ND(EO) = \begin{cases} EO & EO \leq \frac{B}{2} \\ B - EO & \frac{B}{2} < EO \leq B \end{cases} \tag{4.1}$$

where EO is the integer engine order excitation and B is the number rotor blades [87]. Figure 4.1 displays that strain gage limits would be produced for 1B at 2 ND, 2B and 1T at 5 ND, and M20 and M21 at 9 ND. These strain gage limits will monitor the state of stress of the mode shapes of the blade when deflected at the maximum allowable stress, where the modal equivalent stress contours for the subsequent modes can be found in Figure 4.2.

Strain gage limits for each strain gage ensures the rotor is operating in an acceptable stress state for each mode, where acceptable limits are determined using the Goodman diagram. The Goodman diagram (Figure 4.3) for a particular blade and specific mode

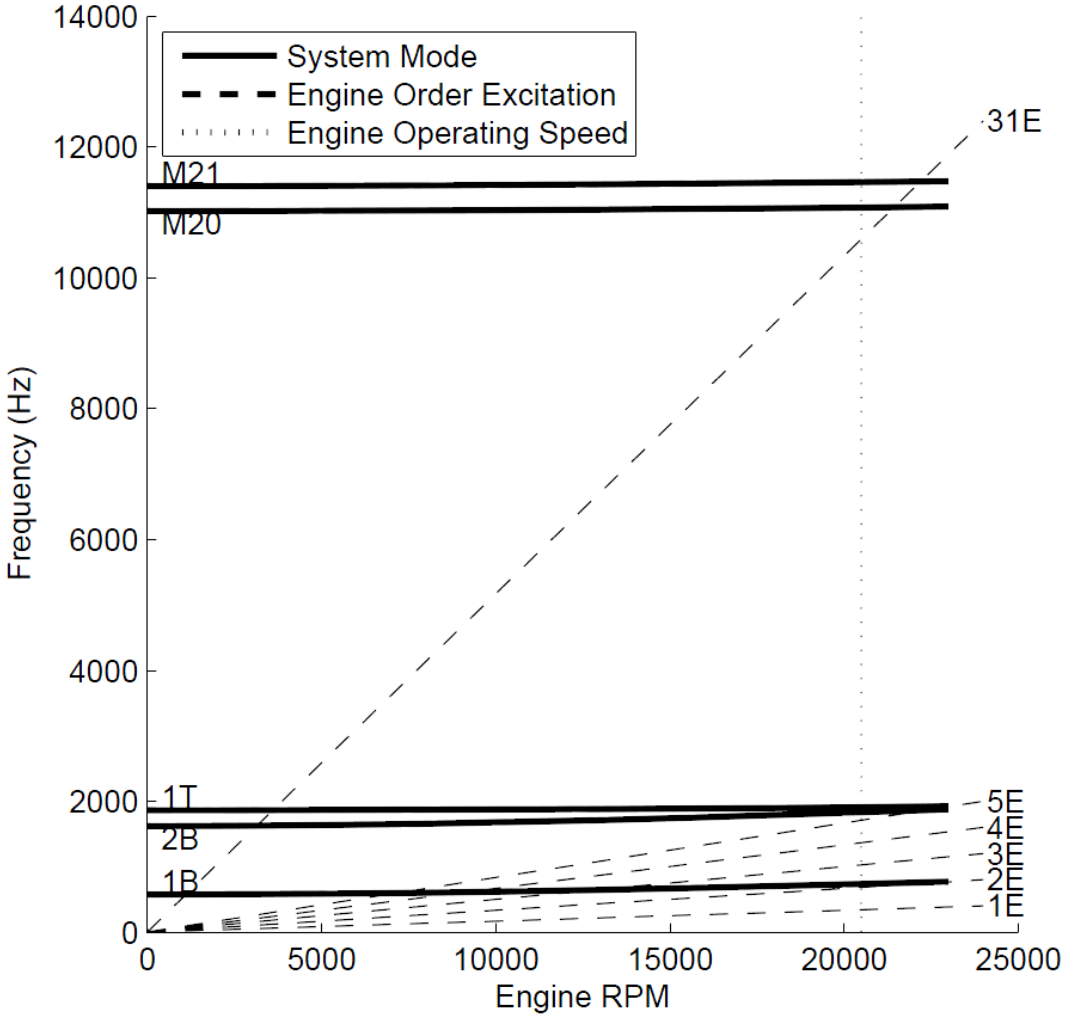

Figure 4.1: Campbell Diagram (Irrelevant Modes Removed).

shows the stress cloud indicating the static and vibratory stress state for each node in the FEM. The failure region is above the solid line, and an additional 60% Goodman line is applied to the figure to account for uncertainties. The calculated strain gage limits are generated using this 60% Goodman line. The static stress for a specific operating condition is unchanged where the vibratory stress depends on the specific mode being analyzed. The modal displacement of a blade is determined using the solution of the Eigen problem

$$[[K] - \omega^2[M]]X = 0 \tag{4.2}$$

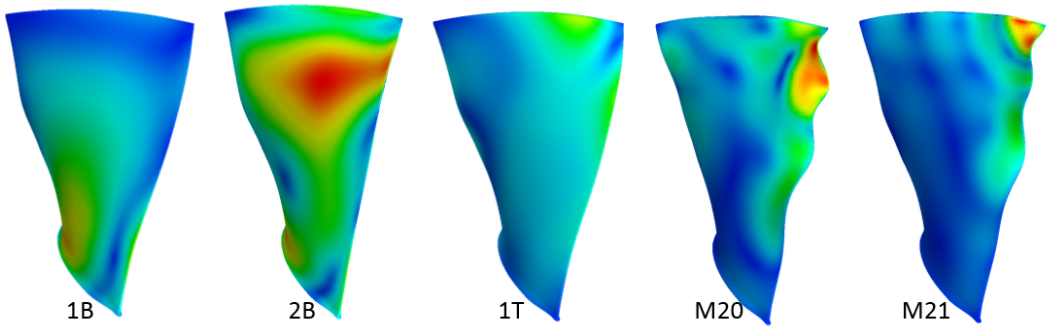

Figure 4.2: Modal Equivalent Stress Contours.

that yields a set of eigenvalues $[\omega_N^2]$ and eigenvectors $[\psi] = [\psi_1, \psi_2, \ldots \psi_N]$ where N corresponds to the DOF of that system. Each node in the FEM is subject to a static stress due to centrifugal effects of spinning the rotor. Each node is also subject to a unscaled vibratory stress due to the mode shape. The Goodman diagram plots the vibratory stress as a function of the static stress, where the limiting node with maximum vibratory stress corresponding to the 60% Goodman line can be found by

$$\sigma_{\nu_{max}}(\sigma_s) f_s \leq G_e \tag{4.3}$$

Equation4.3 takes the unscaled vibratory stress σ_ν and scales it by a factor f_s so that the maximum vibratory stress as a function of the steady stress is within the Goodman envelope G_e. In this paper, the factor f_s is called the modal scale factor, and it will be further discussed when strain gage limits are generated for the tuned FEM.

4.3 Strain Gage Optimization

Strain gages monitor the dynamic stress at multiple locations on a set of blades and relate it to the stresses at uninstrumented critical locations. The design and layout of the placement of these strain gages is not a trivial matter. Proper care and appropriate procedures must

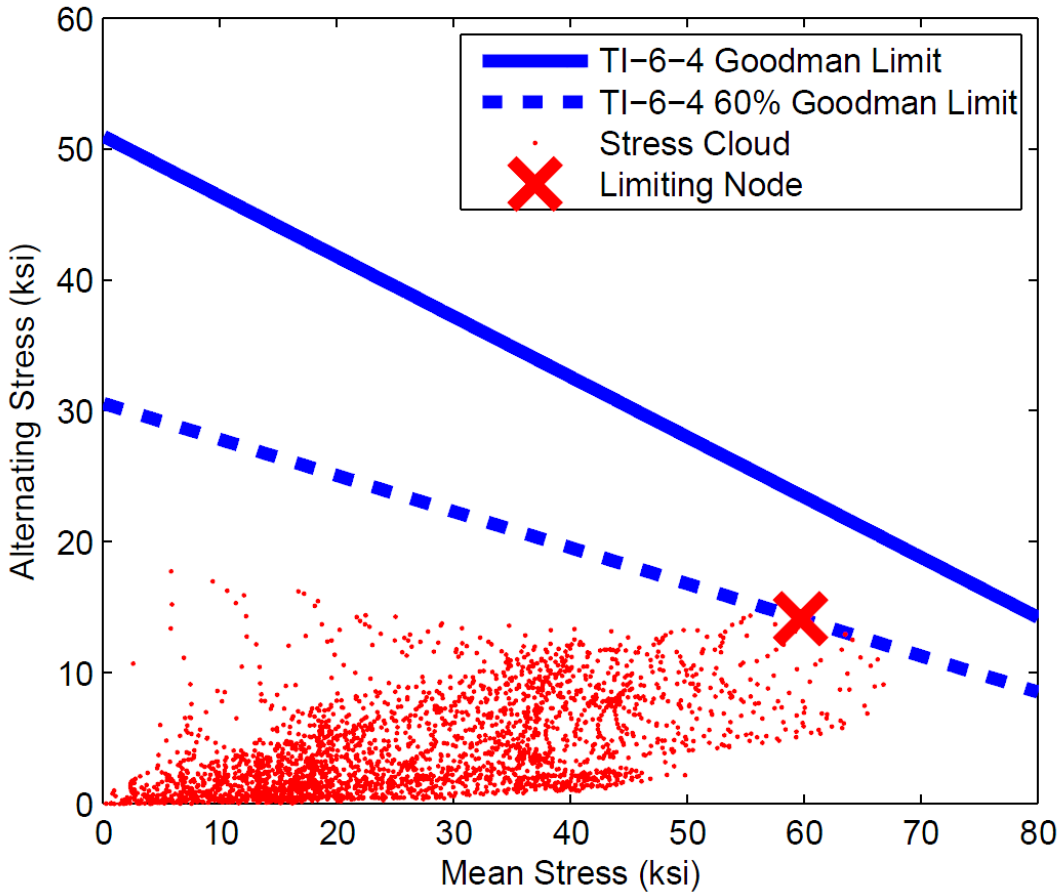

Figure 4.3: Sample Goodman Diagram.

be taken to optimize the location/direction of each gage. The strain gages must be placed in such a way to obtain coverage for all potential system modes in the operating range, to correctly identify which modes are excited, to determine the maximum response of the component for each mode excited, and to obtain clean data from the sensors. Additionally, gages must be placed in accessible locations as some areas on components do not provide enough access to place the gages. There are two types of sensor optimization objectives. One potential method is to find the gage locations for the minimum number of sensors that are capable of observation of a set of modes. This method only maximizes the strain gage ratio, where the gage ratio for each mode of each gage is computed by simply dividing the uniaxial stress recorded by the strain gage by the maximum vibratory stress. Another sensor optimization method optimizes the location and orientation of a user-defined number

of strain gages. This method allows various objectives to be optimized such as amplitude, misplacement, distance, alignment, and mode ID. In many cases the number of strain gages is limited by the data acquisition capacity of the test cell. The work presented here started with a set number of sensors (defined by the data acquisition channel counts) and optimized the location and orientation of eight strain gages by weighting four different objectives: amplitude, misplacement, distance, and mode ID. The final sensor placement is a tradeoff between the various objective functions, and it is not guaranteed that every single objective will be met. Sensor optimization is accomplished in this effort using a commercially available software that utilizes a proprietary randomized searching algorithm that places each sensor on the model and then checks the overall sensor design against the defined objectives to find a high quality design[81, 89].

The amplitude objective seeks to maximize the ratio of the sensor to the maximum value such that

$$r_i^{\epsilon} = \frac{\max(\varepsilon_1 \varepsilon_2 \ldots \varepsilon_N)}{\varepsilon_{\max}} \tag{4.4}$$

where N refers to the number of sensor locations, i refers to the mode being analyzed, and $\varepsilon_{\max}$ is the maximum possible sensor response on the part for the given mode[81]. It is important to place sensors in responsive locations for those modes of interest. A low sensor ratio for a particular mode means the gage will not be responsive for that mode. Every sensor will not have an acceptable ratio for every mode since each mode has unique mode shapes and will be responsive in different locations on the blade. The goal of the amplitude objective is to maximize the ratio for each gage to certify that all modes are covered with responsive strain gages with at least one redundant gage capable of measuring the same mode.

The misplacement objective minimizes the change in sensor ratio with a user defined space. Optimizing for misplacement helps to eliminate errors in sensor placement particularly in areas of high modal deflection gradients. The user has the capability to specify x and y tolerances (Δx and Δy) as well as rotation tolerances ($\Delta\theta$). These tolerances corre-

spond to how far off the actual mounted strain gages can be from the intended locations. The maximum possible mounting error is computed for each sensor location using the i_{th} gage, k_{th} mode using

$$\Delta\varepsilon_{i,k} = \frac{\delta\varepsilon}{\delta x}\Delta x_{max} + \frac{\delta\varepsilon}{\delta y}\Delta y_{max} + \frac{\delta\varepsilon}{\delta\theta}\Delta\theta_{max} + \frac{\delta^2\varepsilon}{\delta\theta^2}(\Delta\theta_{max})^2 \tag{4.5}$$

where the composite gradient value is then computed using a weighted average that ensures that the worst mode meets at least a certain standard according to an average mounting uncertainty of[81]

$$\bar{\Delta\varepsilon_k} = \frac{\Sigma_{i=1}^{N}\varepsilon_{i,k}\cdot\Delta\varepsilon_{i,k}}{\Sigma_{i=1}^{N}\varepsilon_{i,k}} \tag{4.6}$$

The distance objective ensures sensors are not placed within the user specified distance of another gage, where the mode ID objective ensures sensors are placed to be able to distinguish between adjacent modes. Comparing predicted natural frequencies to measured is not an adequate means of mode identification due to a variety of factors such as closely spaced modes with similar frequencies and mode swapping via stress stiffening, temperature, or other influences. Since vibration mode shapes form a mutually orthogonal basis for the structure, mode shapes represent another aspect to use to optimize mode identification. However, there are only a finite number of strain gages on the component, forming a reduced mode shape for each mode, and since the gage locations do not form a continuum the mode shape vectors do not retain their orthogonality[81]. Therefore, the mode identification metric is optimal when the angle between subsequent modes (Equation (4.8)) is as close to orthogonal as possible. This can be demonstrated by looking at the reduced mode shape for an individual mode as

$$\bar{\varphi_i} = \{\varepsilon_1\varepsilon_2\ldots\varepsilon_{N_i}\} \tag{4.7}$$

where the angle between any two mode shape vectors is expressed as[81]

$$\theta_{i,j} = cos^{-1} \frac{\varphi_I \cdot \varphi_J}{\|\bar{\varphi}_I\| \|\bar{\varphi}_J\|} \tag{4.8}$$

The rotor being analyzed in this study had a total of eight strain gages mounted. Three gages were applied on the suction surface of the airfoils, where five gages were mounted on the pressure surface of the airfoil. For the purpose of this study only seven of these gages will be studied because the eighth gage provides coverage for modes other than those being examined here. Placement of the strain gages were optimized to ensure coverage of all potential system modes, mode identification, mode visibility, gage redundancy, data integrity, and geometry, where all objectives were met in the layout of the strain gages. The layout of the strain gages can be found in Figure 4.4. The remainder of the paper will focus on the development of safety limits on rotor airfoil mounted strain gages based on as-manufactured geometry measurements from a high fidelity optical geometry collection systems that obtains more accurate strain gage limits.

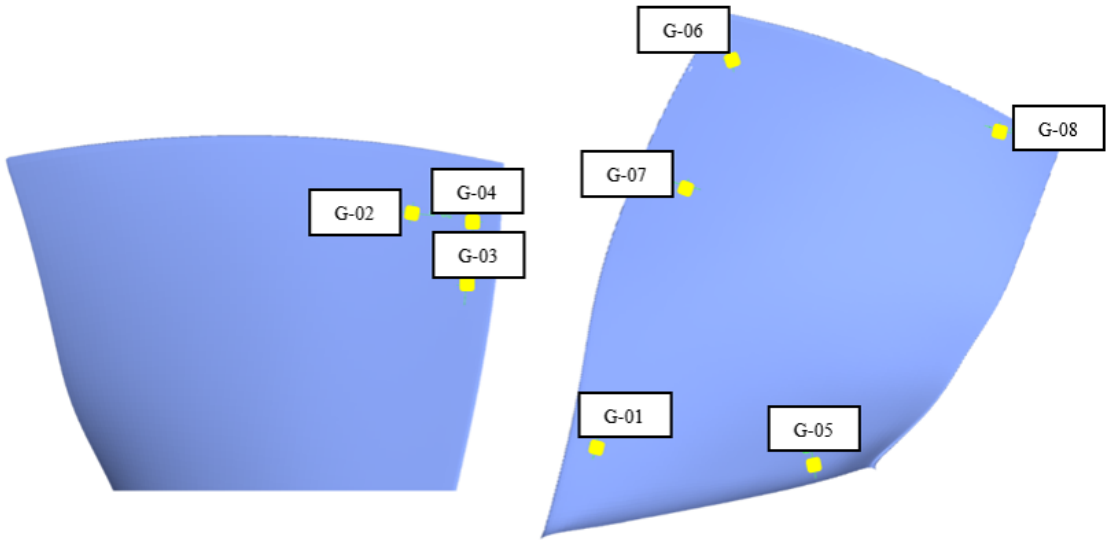

Figure 4.4: Strain Gage Locations.

4.4 Tuned Strain Gage Limit Approach

The transonic compressor analyzed throughout this paper is an IBR consisting of 20 low-aspect ratio blades and 31 stator vanes[90]. A single sector of the disk-airfoil FEM can be found in Figure 4.5, which consists of 95% hexahedral elements and a tetrahedral/pyramidal element interface between the base of the airfoil and the disk. To simulate the compressor operating enivornment, cyclic boundary conditions were used and the IBR was constrained at the hub of the rotor. A rotational velocity of 21,233 rpm was applied to the FEMs to account for the steady stress component followed by a pre-stressed modal analysis to calculate the vibratory stress associated with each sector FEM. The FEM analysis results were used as inputs to perform the aforementioned strain gage optimization to meet the specified objective functions.

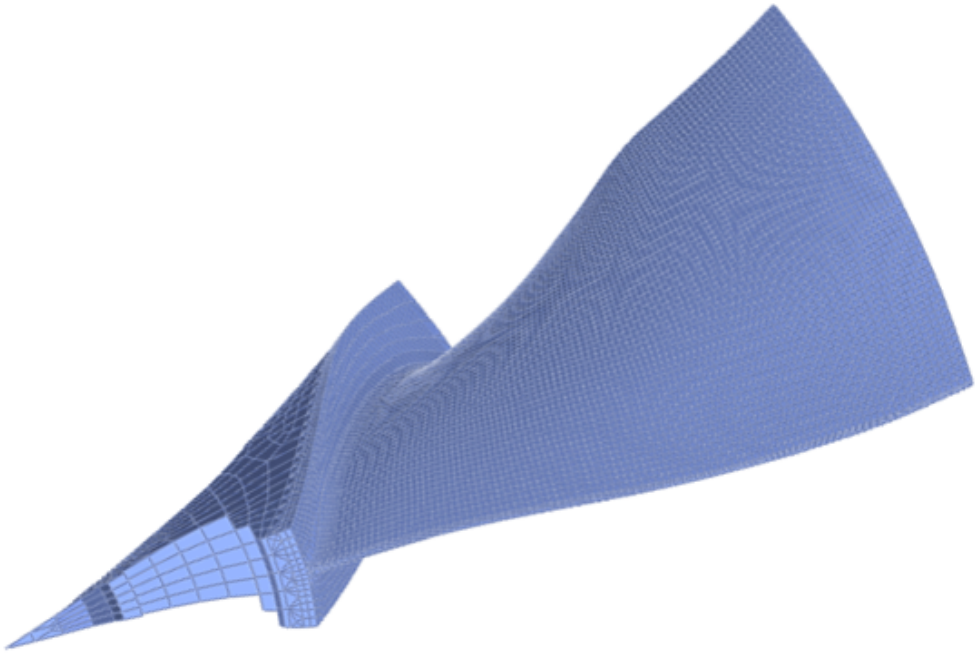

Figure 4.5: Single Sector of the IBR FEM.

After the optimization of the strain gage locations, the strain gage limits can be derived. The standard approach for determining strain gage limits requires the computation of the gage ratios to the maximum vibratory stress for each mode. If a gage is less than

a standard ratio (typically 0.30), strain gage limits are not initially set for that gage. If the gage ratios are greater than 0.30, then they can be considered responsive strain gages. The strain gage limits associated with the five modes identified in the Campbell diagram of Figure 4.1 will be generated. The gage ratios for the responsive strain gages can be found in Table 4.1 in the columns labeled Ratio. It can be seen from Table 4.1 that all five modes of interest are well covered. This helps to ensure modal coverage if strain gages begin to fail during engine/rig operation. The strain gage limits are generated using

$$\sigma_{limit} = r_{sg} \times f_s \times \sigma_{max} \tag{4.9}$$

where r_{sg} is the strain gage ratio, f_s is the modal scale factor generated by scaling the maximum vibrational stress to the Goodman envelope, σ_{max} is the maximum vibrational stress on the airfoil of the sector model, and σ_{limit} is the sensor limit of a strain gage. The limits for the responsive strain gages were generated using Equation (4.9) and can also be found in Table 4.1. If a strain gage were to reach this limit in practice, then some location on the airfoil has reached or exceeded the Goodman envelope. If no limit is recorded in the table for a specified gage/mode, then the sensor ratio did not meet the threshold gage ratio. Again, it is important to point out that the safety limits developed in Table 4.1 were calculated with a nominal model of the rotor geometry, and the results will be further discussed in the following sections. The next section will define the approach that will be implemented to compare the nominal sector strain gage limits to the individually mistuned sectors to analyze the variation between the nominal model compared to the as-manufactured results.

Table 4.1: Nominal Sector Strain Gage Results

		Gage 01		Gage 02		Gage 03		Gage 04		Gage 05		Gage 06		Gage 07	
Mode	**ND**	**Ratio**	**σ (ksi)**	**Ratio**	**σ (ksi)**	**Ratio**	**σ (ksi)**	**Ratio**	**σ (ksi)**	**Ratio**	**σ (ksi)**	**Ratio**	**σ (ksi)**	**Ratio**	**σ (ksi)**
1B	2	0.58	11.90	–	–	–	–	–	–	0.83	16.98	–	–	–	–
2B	5	0.66	12.19	–	–	0.63	11.60	–	–	0.60	11.13	0.51	9.45	0.39	7.12
1T	5	–	–	0.46	10.39	–	–	–	–	–	–	–	–	–	–
M20	9	–	–	–	–	0.31	8.51	0.84	23.49	–	–	0.37	10.31	–	–
M21	9	–	–	–	–	–	–	0.36	10.00	–	–	0.68	18.97	–	–

4.5 Mistuned Strain Gage Limit Approach

An alternative to using a tuned FEM to determine strain gage limits, is to use numerical modeling to create an as-manufactured FEM of each airfoil-disk sector. Each as-manufactured bladed sector FEM is referred to as a mistuned FEM. The mistuned FEMs of the IBR were created through optical topography measurement and mesh morphing. The mesh moprhing process begins with an optical scanning system that uses structured light and high density charged coupled devices to develop a point cloud geometry that represents the surface coordinates of the as-manufactured IBR. The point cloud generatred for this IBR contained 2 x 10^6 scan points with an average observable noise of ± 0.3 thousandths of an inch (significantly smaller than tuned FEM to AMM deviations)[9]. Next, the as-manufactured point cloud is aligned to the tuned FEM via an iterative closest point procedure. The surface nodes of the FEM are then modified to match the tessellated surface data of the point cloud. The outcome of this mesh morphing process is a mistuned FEM that matches the actual as-manufactured geometry of the IBR. The mesh morphing process for this IBR is displayed in Figure 4.6, where Figure 4.6a shows the pre-mesh morphing process where the tessellated surface data (white surface mesh) is aligned to the tuned FEM and Figure 4.6b shows the post mesh morphing process after the surface nodes of the FEM were aligned to match the white surface mesh. The described mesh morphing process created 20 separate cyclically symmetric as-manufactured, mistuned FEMs matching the actual geometry of each airfoil-disk sector. Further details of this mesh morphing process can be found in the works of Kaszynski et al [53, 87].

Using the procedure outlined with the nominal rotor model, strain gage limits were computed for each one of the 20 isolated blade sectors. This was accomplished by using the same approach and assumptions as in the tuned IBR except with modified geometry. Identical strain gage locations were utilized for each airfoil. The strain gage results for each of these 20 isolated mistuned blade sectors can be found in Table 4.2. The gage ratios for

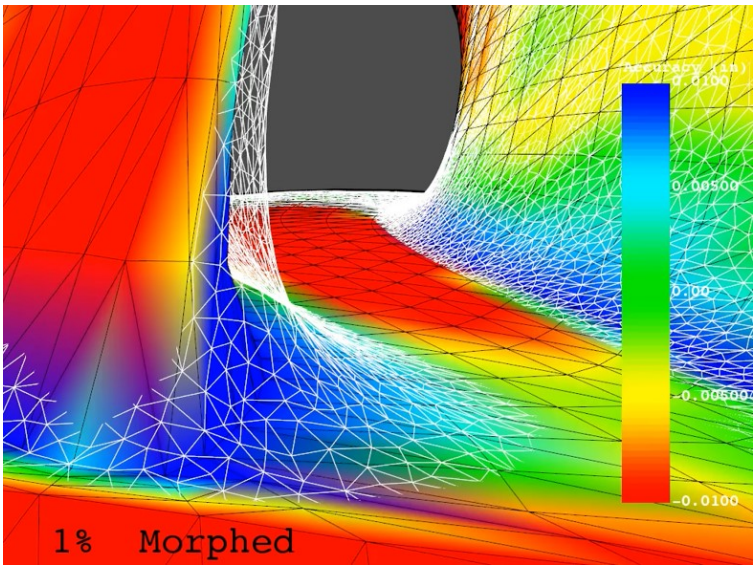

(a) Pre-Mesh Morphing

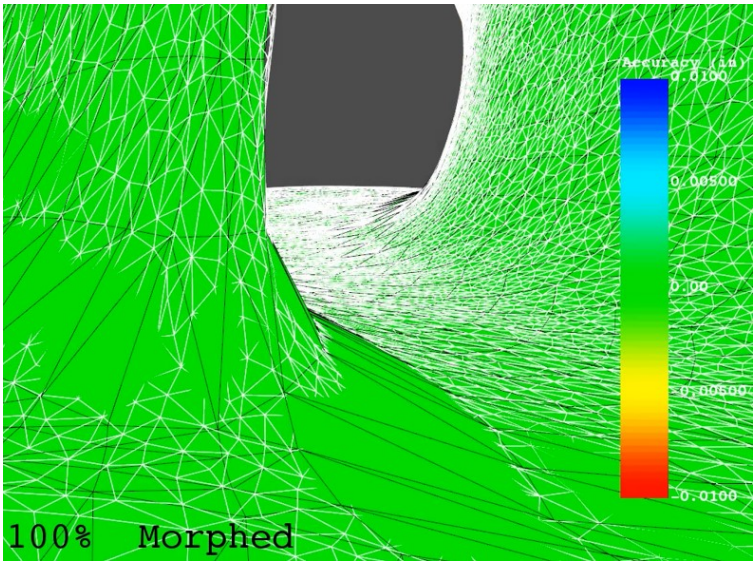

(b) Post-Mesh Morphing

Figure 4.6: Mesh Morphing Process.

the responsive strain gages can be found in Table 4.2 in the columns labeled Ratio, where the safety limits for each gage can be found in the adjacent column. The results indicate that the small perturbations in the airfoil geometry representing the as-manufactured rotor create a significant variation in the strain gage ratios and safety limits.

To further examine the results presented in Tables 4.1 & 4.2, lets interrogate Mode 21 (M21) using Gage 04 (G-04). Specifically, three cases will be investigated. Case 1 investi-

gates the interpretation of the nominal analysis found in Table 4.1. The gage sensitivity and associated gage limit for the nominal model are 0.36 and 10 ksi respectively. This essentially means that the gage is anticipated to be responsive to this mode, and a limit of 10 ksi would be set for this gage. If this limit were exceeded, then depending on the severity of the exceedance, cycles above limit would need to be analyzed to determine remaining life as well as other time-intensive work to accomplish to get back to test, i.e., cost and schedule risk. Case 2 explores the scenario where the gage ratio of the mistuned sector falls below the threshold. The gage ratio for M21, G-04 in Table 4.2 varies between 0.07-0.47. This signifies that the G-04 gage location gage ratio falls below the threshold of 0.30 for some blades on this rotor. Since the sensitivity of some of the blades fall below the threshold, a gage would not want to be placed on these blades and safety limits would not be set because it is not considered a responsive gage. So if by chance G-04 is randomly put on one of the blades with a small gage sensitivity, the gage could be unresponsive even though the nominal model indicates it would. This would be an inadequate use of one of the data acquisition channels. Finally, Case 3 considers the scenario where the gage is responsive but the safety limit is lower than nominal. The gage sensitivity and associated gage limit for one of the responsive blades for M21, G-04 are 0.32 and 8.7 ksi. As is presented in the nominal model (Case 1), the gage is responsive, but the safety limit for this blade is 8.7 ksi compared to the nominal limit of 10 ksi. If G-04 were placed on this notional blade and limits were set using the nominal limit, the actual limit for this blade could be continuously exceeded without exceeding nominal limits. Therefore, continuous operation above the 60% Goodman envelope is possible under present day strain gage limit techniques. During typical engine and rig demonstrations, there is a redundancy of three gages to monitor each mode, so this does reduce the odds of encountering Case 2 or 3 above. However, gage mortality rates provide increasing odds that one of the cases can be encountered with the potential for catastrophic failures. Consequently, as-manufactured models are required for assured strain gage measurement.

Table 4.2: Mistuned Sector Strain Gage Results

		Gage 01		Gage 02		Gage 03		Gage 04	
Mode	**ND**	**Ratio**	**σ (ksi)**	**Ratio**	**σ (ksi)**	**Ratio**	**σ (ksi)**	**Ratio**	**σ (ksi)**
1B	2	0.55 – 0.62	9.20 – 12.81	–	–	–	–	–	–
2B	5	0.47 – 0.69	8.91 – 13.17	–	–	0.49 – 0.69	8.08 – 12.96	–	–
1T	5	–	–	0.37 – 0.57	8.43 – 12.71	–	–	–	–
M20	9	–	–	–	–	0.10 – 0.39	2.57 – 10.73	0.48 – 0.89	13.08 – 25.15
M21	9	–	–	–	–	–	–	0.07 – 0.47	2.07 – 13.56

(a) Strain Gages 01 – 04

		Gage 05		Gage 06		Gage 07	
Mode	**ND**	**Ratio**	**σ (ksi)**	**Ratio**	**σ (ksi)**	**Ratio**	**σ (ksi)**
1B	2	0.75 – 0.89	13.63 – 17.89	–	–	–	–
2B	5	0.42 – 0.62	8.39 – 11.91	0.41 – 0.57	6.38 – 10.44	0.17 – 0.46	3.79 – 9.34
1T	5	–	–	–	–	–	–
M20	9	–	–	0.10 – 0.51	2.85 – 14.76	0.08 – 0.33	2.37 – 8.94
M21	9	–	–	0.60 – 0.76	16.57 – 22.59	–	–

(b) Strain Gages 05 – 07

Investigating the variation in sensor ratios and limits further, the sensor limits from Tables 4.1 & 4.2 have been combined to form Figure 4.7 to better compare the nominal model and the mistuned isolated sectors. Figure 4.7a displays the strain gage ratio variation across each blade, where Figure 4.7b shows the strain gage limit variation across each blade. The solid square in each figure indicates the ratio and limit assuming the tuned/nominal model where every blade is treated as identical. The triangle bounds show the variation between blades 1 through 20. The x-axis specifies the gage and the associated mode that gage covers. There is clearly significant variation for each gage and for each mode. For example, G06/M20 has a nominal sensor ratio above the threshold but when accounting for the as-manufactured blades, the sensor ratio can vary well above to well below the threshold. These large sensor ratio variations can play a large effect on sensor limits and also show a need to account for this variation to maximize the strain gage response. The sensor limit variation across each as-manufactured blade portrays substantial deviation from the nominal limit. This allows the capability to increase or decrease limits depending on which blade a particular sensor is placed.

It is interesting to note that there is a significantly lower variation between the maximum mistuned sector limit and the nominal limit compared to the minimum mistuned

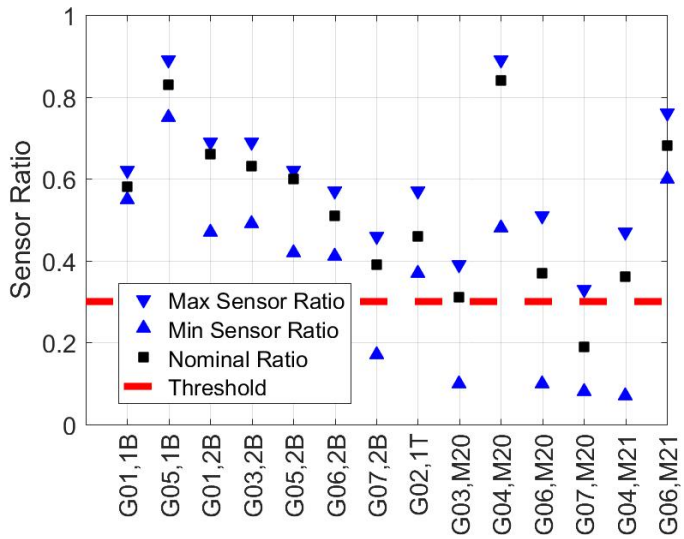

(a) STRAIN GAGE RATIO VARIATION

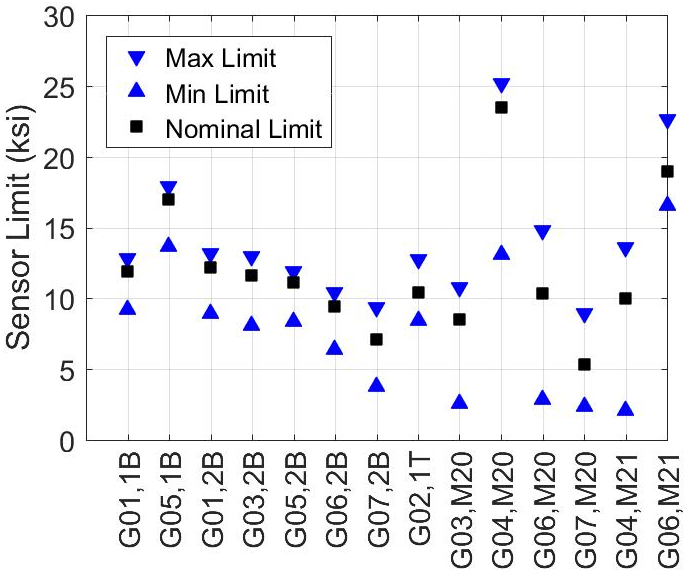

(b) STRAIN LIMIT VARIATION

Figure 4.7: Sensor Ratio and Limit Variations.

sector limit and the nominal limit. The nominal model utilized in this effort was compiled by averaging each of the 20 sectors of the rotor, so this could imply the lower order modes average/nominal model limits better represents the higher responding blades. It is clear to see that all gages for all modes have significant limit variation between the nominal and mistuned sector. This is true regardless of the gage ratio. Most of the gages for the higher

order modes have a much larger variation compared to the lower order modes. Viewing the mode shapes for these higher order modes (Figure 4.2), it can be seen that the modal activity is localized at the tip region. A small perturbation in the geometry of a blade greatly effects the strain gage limits of the higher order modes. The sensor limit variation is so significant for these higher order modes because the sensor ratio for several of the blades falls below the required threshold of 0.3. Therefore, sensor limits should not even be set for some of these blades since they could be unresponsive. This ultimately shows the importance of using as-manufactured models to develop sensor limits to reduce the risk of catastrophic failures.

4.6 Utilizing Sensor Limits from a Mistuned IBR

It has been shown that due to the high variability of blade-to-blade geometry the strain gage limits can vary significantly between blades. This knowledge lays the foundation to more accurately place strain gages on responsive blades to ensure safe engine operation during testing. There are different techniques for choosing blades for which to apply strain gages, and different engine manufacturers and companies follow their standard work when choosing which blades to instrument. The work presented in this paper allows for the capability to use the as-manufactured models to place strain gages.

To investigate this more thoroughly, the sensor ratio and strain gage limits for only Gage 06 will be examined since it provides coverage across three different modes (2nd bend, Mode 20, and Mode 21). Figure 4.8a displays G-06 sensor ratios as a function of blade number for each of the five modes of interest. The threshold ratio of 0.3 is also visible in the figure, where a gage is considered responsive if it is greater than this threshold. Gage 06 clearly provides coverage for Mode 2 and Mode 21, while it also provides coverage for Mode 20 for some of the blades. Due to the geometric variation in the blades, the sensor ratio for Mode 20 for some of the blades falls below the required threshold, and gages

should not be applied on these blades. One approach to more accurately place Gage 06 on this rotor is to survey the local maxima for the mode that crosses above and below the threshold. If the local maxima of this mode (Mode 20) is above the threshold, than that would be one possible blade to apply a strain gage. This ensures coverage for all three modes with this single gage. Figure 4.8a shows seven potential blades (Blade 1, 5, 7, 10, 11, 15, and 19) to apply Gage 06.

To calculate sensor limits for Gage 06 going forward, Blade 19 will be picked to apply the strain gage. Figure 4.8b presents the sensor limit for Gage 06 as a function of blade number, where the nominal gage limit is also presented for each mode covered by the gage. Mode 2 has a nominal limit of 9.45 ksi, where the actual limit determined using the as-manufactured model of blade 19 specifically is 10.34 ksi, an 8.6% difference. Mode 20 has a nominal limit of 10.31 ksi with an actual limit of 14.76 ksi, a 30.1% difference. Finally, Mode 21 has a nominal limit of 18.97 ksi with an actual limit of 18.72 ksi, a -1.3% difference. Consequently, utilizing the isolated mistuned blade models to place strain gages presents a more accurate means of correctly determining the sensor location. This approach has the capability to apply strain gages with satisfactory sensor ratios on responsive blades. More importantly, this approach has the potential to set the sensor limits more accurately to avoid scenarios where operation occurs outside the Goodman envelope, minimizing the possibility of catastrophic failure.

4.7 Conclusion

Strain gages are a commonly used stress measurement system to analyze the operational stresses within engine rotors. Safe engine operation is ensured by setting safety limits on rotor mounted strain gages to ensure the stresses on the component are at or below safe engine operation. Traditionally, strain gage limits are generated utilized nominal geometry obtained from an as-designed nominal model where finite element analysis (FEA) is used

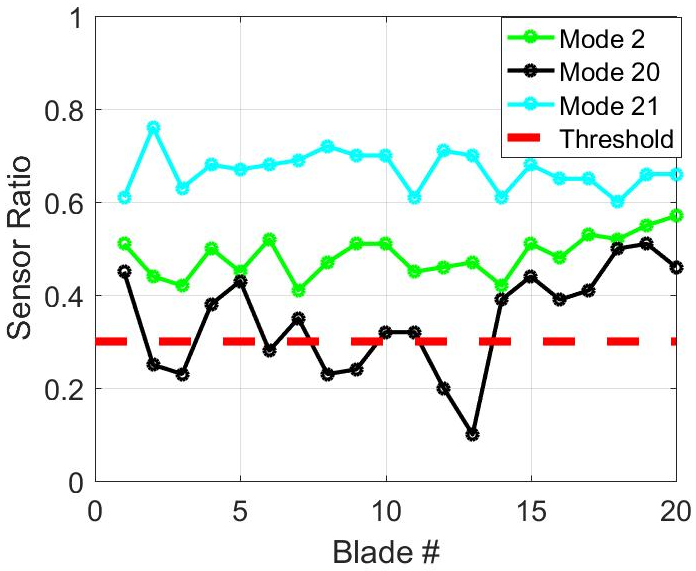

(a) SENSOR RATIO vs. BLADE NUMBER

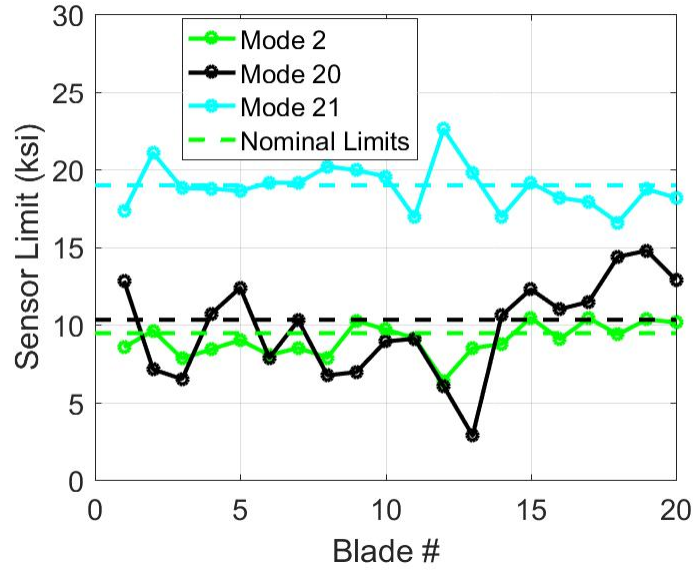

(b) SENSOR LIMIT vs. BLADE NUMBER

Figure 4.8: Sensor Ratio and Limit Variations for Gage 06.

to compute the static stresses as well as the mode shapes. The predicted mode shapes of the cyclic analysis are used to optimize strain gage locations to ensure modal coverage, modal ID, and to ensure determination of maximal vibrational stress for each mode of interest. Strain gage limits are then produced for these optimal strain gage locations on the tuned finite element model. It is now possible through high fidelity optical geometry

collection systems to obtain more accurate strain gage limits using measured IBR geometry from as-manufactured rotors. It has been shown that due to the high variability of blade-to-blade geometry obtained from an optically scanned rotor that the strain gage limits can vary significantly between blades. This was demonstrated by analyzing a mistuned IBR on a sector by sector basis. The approach utilized in this paper presents a more accurate means of correctly determining the sensor location with the capability to apply strain gages with satisfactory gage ratios on responsive blades. More importantly, this approach has the potential to set the sensor limits more accurately to avoid scenarios where operation occurs outside the Goodman envelope. This ultimately shows the importance of using as-manufactured models to develop sensor limits.

Mistuning Evaluation Comparison via As-Manufactured Models, Traveling Wave Excitation, and Compressor Rigs

As-manufactured rotors behave quite differently than nominal, as-designed rotors due to small geometric and material property deviations in the rotor, referred to as mistuning. The mistuning of a 20 bladed, integrally bladed rotor (IBR) will be evaluated via analytical methods, benchtop testing, and using a rotating compressor research facility. Analytical methods consist of the development of an as-manufactured model based on geometry measurements from a high fidelity optical scanning system. Benchtop testing of the IBR is done using a traveling wave excitation (TWE) system that simulates engine order excitation in stationary bladed disks for the purpose of determining potentially high responding blades due to mistuning. The compressor research facility utilizes blade tip timing (BTT) to measure the blade vibration of the IBR. The resonant response of the IBR at various modes and harmonic excitations is investigated in this work. A comprehensive mistuning and force amplification comparison between the as-manufactured model, TWE, and the compressor rig is performed. Mistuning of each method is evaluated using three different methods. First, the tuned absorber factor (TAF), which is a metric to determine potential high responding blades, is determined for each system. Next, mistuning is analyzed by isolating

individual blades both experimentally on the bench and analytically to determine the mistuning patterns. Lastly, the mistuning determined by each system will be evaluated using a reduced-order model, namely the Fundamental Mistuning Model Identification (FMM ID). It will be shown that TAF shows variability between each method providing indications TAF may not be the best approach of force amplification predictions. Basic mistuning agreements exist when isolating blades both experimentally and analytically exhibiting as-manufactured models are capable of representing full experiments. System ID methods provide a basic agreement between both the mistuning pattern and the mistuning amplification for all three methods analyzed. This ultimately shows the importance and the ability to use as-manufactured models to help increase detailed understanding of IBRs.

5.1 Introduction

Integrally bladed rotors are designed to be nominally cyclically symmetric, i.e., each blade is identical to every other blade. However, as-manufactured rotors do not exhibit this condition due to small geometric and material deviations in the rotor known as mistuning [6]. The machining process, material deviations, and field wear allow for each blade to have varying properties and thus varying natural frequencies and responses that could lead to the confinement of the vibrational energy to an individual blade [7]. The potential exists to excite these natural frequencies when a rotor is subject to harmonic excitations during engine operation, causing resonance and premature failure from high cycle fatigue [91]. HCF and mistuning is still of interest despite being studied for decades [2, 78, 79]. Designers attempt to evade resonance crossings throughout the engine operating range to avoid potential HCF issues, but total avoidance of engine order (EO) excitations is challenging. Therefore, it is vital that accurate modeling approaches predict the forced response of resonance crossings.

Reduced-order modeling (ROM) approaches for predicting mistuning patterns and amplifications and the potential for HCF continue to make advancements. Beck et al. [36]

provides a good overview of mistuning ROMs showing the progression and advancements from lumped parameter models to approaches that predict and quantify forced response distributions for a population of mistuned IBRs probabilistically. More recently research has been conducted on utilizing reverse engineered physics-based models to predict responses based on coordinate measurement machine points or optically-scanned geometry, i.e., as-manufactured models [8–10]. These as-manufactured models align with visions for aircraft and engine digital twins by the Air Force Research Laboratory (AFRL) and NASA [92]. Using as-manufactured models allows for the calculation of frequency mistuning patterns and forced response directly from a finite element model (FEM). As-manufactured FEMs can be created for both newly machined components and components that have been in service undergoing degradation from engine wear, allowing for IBRs to be analyzed throughout their life-cycle. Further, it has been shown that accounting for the geometric blade-to-blade variation via as-manufactured FEMs illustrates a large variation in sensor response and placement of safety instrumentation, i.e., strain gages and tip timing probes [11, 12]. Hence, as-manufactured models have the potential to be utilized for not only mistuning identification, but also higher fidelity sensor placement, more accurate computationally fluid dynamic (CFD) simulations for turbines and compressors [13, 14], and a suite of other possibilities, representing a dramatic increase in knowledge for the turbine engine community.

Despite advancements in mistuning ROMs and as-manufactured modeling approaches, there exists a void of studies comparing these analytical methods to real world applications such as rig and engine tests. There have been published studies comparing ROMs such as component mistuning model (CMM) and Fundamental Mistuning Model(FMM) ID to Traveling Wave Excitation (TWE) benchtop experiments that have shown the capability of using these models to determine mistuning in a bladed disk [31, 34, 55, 62]. Feiner and Griffin additionally showed the ability of FMM ID to accurately predict the mistuning pattern of an IBR under rotating conditions in a spin pit using non-intrusive measurement

system (NSMS) [55]. Additional studies have used ROMs to predict the mistuned response of rotating compressors in both single and multistage rigs. Petrov, et al. [76] performed a comparative study between a FEM with computational fluid dynamic (CFD) inputs and a wind tunnel with a full-scale rotating bladed disk and aerodynamic excitation by nozzle guide vanes. The predicted blade responses were on the same order, but showed significant variation between the predictions and the experiments. Besem, et al. [72, 73] conducted a forced response analysis of a first torsion mode in a multistage compressor and found good agreement between the analysis and the experiment for the maximum blade response, but underpredicted the maximum blade amplitudes compared to the experiment. The most recent study by Li, et al. [74, 75] analyzed the forced response predictions using FMM and CMM of a first chordwise bending mode of an embedded multistage compressor. The study found the predicted response has a high sensitivity to small deviations in the blade frequency mistuning patterns and that a mistuning problem should be approached in a probabilistic manner.

In addition, there have been several comparisons of FEMs generated using point clouds from optical measurements. Schoenenborn, et al. [46] used optical measurements to create single airfoil models with simplified blocks at the blade/disk interface and compared to eigenfrequencies determined from isolated modal testing. The general mistuning trend for both a $2F$ and $3F$ mode was predicted well, but there were quantitative differences between the generated FEMs and modal tests. Hönisch, et al. [48] also used optical measurements with fringe projections to develop FEMs of an axial compressor and a turbine blisk for a turbocharger. The actual development of the FEM was not discussed and the predicted sector frequency deviations did not compare well to experimental modal ping testing. Cazenove, et al. [50] also used optical scanning to create a point cloud of an IBR from which they generated a CAD model and then FEM of the blisk. Each blade was isolated in a cantilevered analysis and compared to isolated ping testing, isolated acoustic excitation, and shaker tests with noticeable variations in the blade frequency deviations be-

tween each comparison. Schnell, et al. [13] developed simplified FEM simulations of only blade airfoils with no disk for nine scanned blades and found the eigenfrequency scattering due to geometric variability was on the order of ± 3 Hz. Nyssen, et al. [51] used optical scanning to develop as-manufactured FEMs of a simple academic structure from which a mistuning comparison utilizing a ROM developed by Lim [34] was made to experimental electrodynamic shaker tests. Initial mistuning and mode shape comparisons did not relate well and the Young's modulus of the FEMs were also changed to achieve better results. Maywald, et al. [10] utilized an as-manufactured model via mesh morphing to predict the mistuning pattern of an IBR and successfully compared the results to an experiment that isolated individual blades to determine the blade alone frequencies. Kaszynski, et al. [54] showed that a full 360° digital twin model via mesh morphing of an IBR is sufficient in predicting the mistuned response and validated the approach to TWE. The majority of the discussed comparison studies of as-manufactured FEMs are related to isolated modal ping tests or electrodynamic shaker experiments with only a single as-manufactured comparison to TWE experiments. The work presented here seeks to fill a void by providing additional as-manufactured FEM comparison studies to not only isolated modal experiments and TWE, but also to a rotating compressor rig.

Geometric mistuning model comparison studies discussed in open literature have been between ROMs/benchtop experiments, ROMs/compressor rigs, parametrized FEMs/compressor rigs, and as-manufactured FEMs/benchtop experiments. This work will provide an all-inclusive mistuning evaluation of an IBR comparing as-manufactured models, traveling wave excitation, and a rotating compressor rig with inlet distortion. The culmination of this work will illustrate the ability to use as-manufactured models to predict both the mistuning pattern and the force amplification due to mistuning for a 1^{st} bend, 2^{nd} bend, and 1^{st} torsion mode of an IBR.

5.2 Rotor Description

The IBR being analyzed in this study has 20 low-aspect ratio rotor blades and is given the designated name PBS (Parametric Blade Study) R4 [90]. A schematic of the compressor stage as installed in the compressor facility can be found in Fig. 5.1. PBS R4 is subject to aerodynamic excitations from 31 downstream stator vanes, 4 downstream struts, and an inlet distortion screen. During compressor rig operation, downstream struts excite a 1^{st} bend mode with an EO4 excitation at 9123 rpm, the inlet distortion screen excites a 1^{st} bend mode with an EO3 excitation at 12743 rpm, and a combination of strut and distortion screen drivers combine to produce an EO7 excitation that excite a 2^{nd} bend mode at 14860 rpm and a 1^{st} torsion mode at 16121 rpm. The Campbell diagram for the associated EO excitations and specific modes of interest can be found in Fig. 5.2. Each of these modes will be evaluated for mistuning using isolated modal testing, TWE, a compressor rig, and using an as-manufactured model of PBS R4.

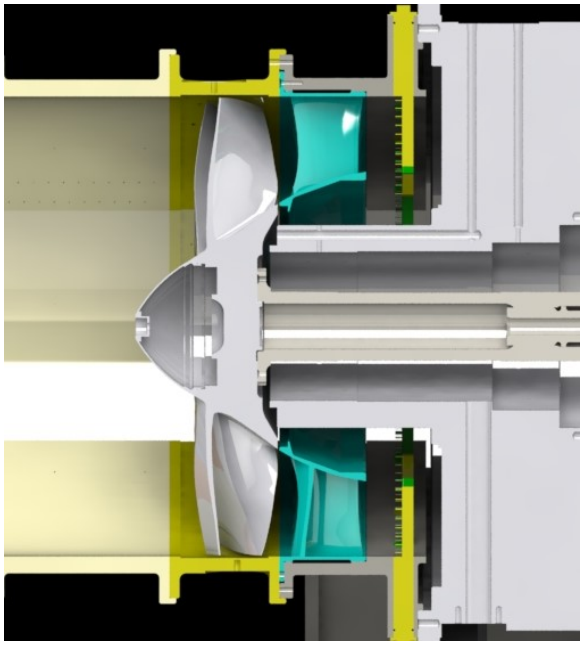

Figure 5.1: PBS R4 Stage Schematic

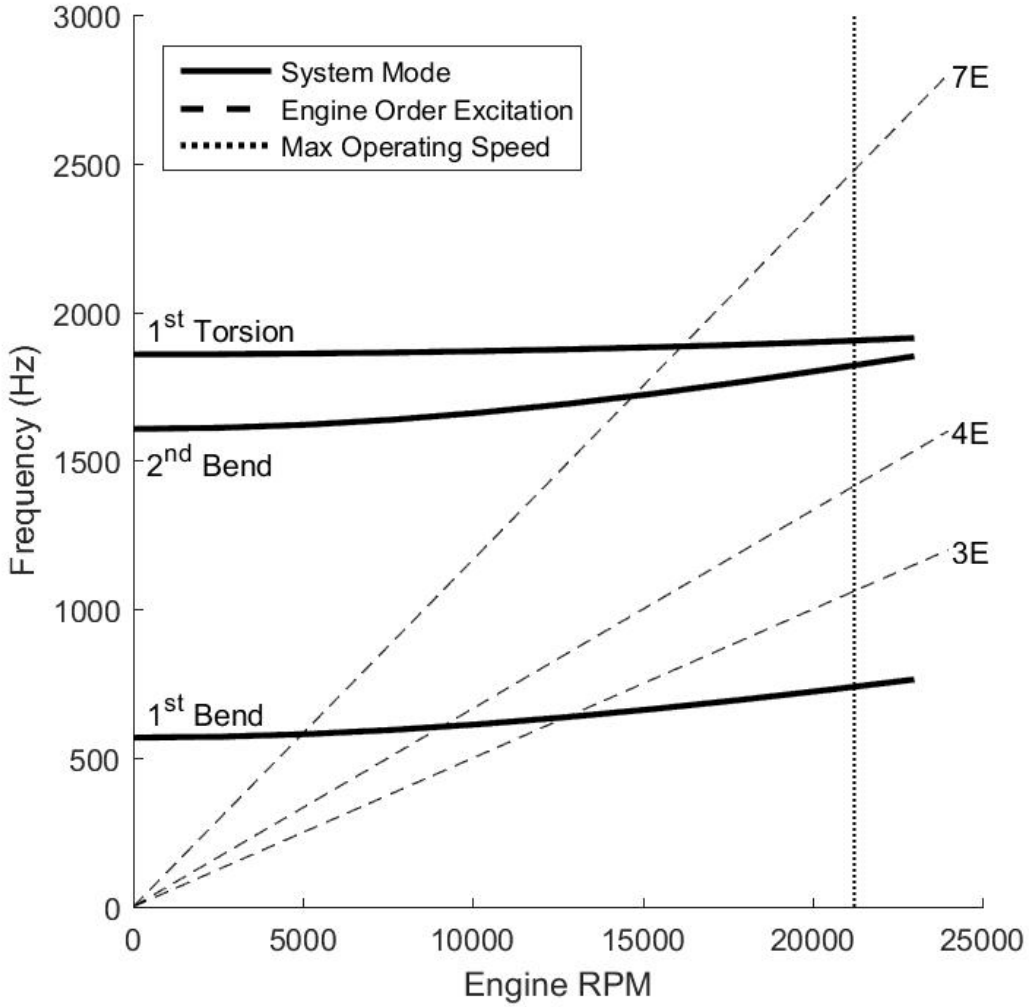

Figure 5.2: PBS R4 Campbell Diagram

5.3 Experimental & Analytical Forced Response

Experimental and analytical forced response analyses were conducted to analyze each mode: 1^{st} bend at EO 3 and EO 4, 2^{nd} bend at EO 7, and 1^{st} torsion at EO 7. Two experimental methods were utilized. The first is a benchtop TWE that is operated at AFRL in the Turbine Engine Fatigue Facility (TEFF). The second is a rotating compressor rig at AFRL in the Compressor Aero Research Laboratory (CARL). Analytical forced response simulations were done using developed as-manufactured models.

5.3.1 Traveling Wave Excitation

Turbine engine rotors experience harmonic excitations driven by the interaction between the rotating airfoils and aerodynamic disturbances from neighboring components such as inlet guide vanes, stators, or support struts. Each airfoil experiences the same load magnitude but at offset phase angles that are a function of the engine order excitation[60]. Traveling wave excitation systems simulates an engine order environment of the rotor[6, 61]. The TWE consists of a stationary IBR, a mounting fixture, electromagnetic actuators, a fixture for the actuators, a function generator, a phase shifting amplifier, impedance matching transformers, and a computer with control software. Since PBS R4 is non-magnetic, small metal disks are temporarily attached to the blade excitation location. The mass of the metal plate is very small compared to the airfoil mass. Internal investigations have shown the metal disks cause a global shift in modal frequencies on the order of $0 - 5\%$ depending on the excited mode that can change mode spacing, but produce similar mistuning patterns compared to acoustically driven TWE experiments. Fig. 5.3 displays an image of the IBR on the TWE table with the electromagnets engaging the small metal disks on the trailing edge of each blade. The response of each airfoil is measured with a scanning laser vibrometer. Traveling wave tests were conducted simulating the EO excitations experienced by the rotor under rig conditions. The response for each blade resulting from TWE is shown in Fig. 5.4, where each colored line in Fig. 5.4 denotes an individual blade response. Results are evaluated for mistuning using the system identification methods discussed in Section 5.4.

5.3.2 Compressor Aero Research Laboratory

Upon completion of TWE testing, PBS R4 was installed in the CARL facility. The facility tests axial flow compressors with speeds up to approximately 21000 rpm. Compressors

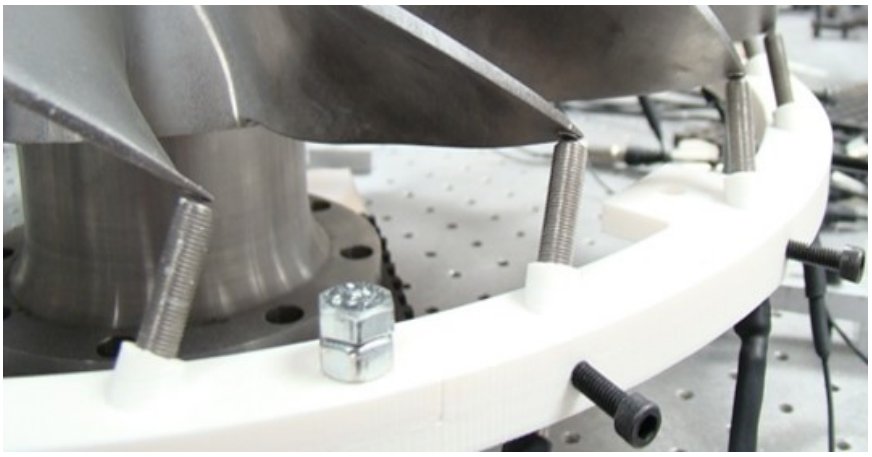

Figure 5.3: PBS R4 TWE Setup

are powered via a 6000 HP induction motor, an eddy current clutch for speed control, and a gearbox to achieve test speeds. The compressor rig in Fig. 5.5 is heavily instrumented including blade mounted strain gages and a non-contact measurement system (NSMS). The strain gages and NSMS probes monitor each of the vibratory modes (as discussed in Section 2) that are excited across three different EO excitations. This was accomplished through a combination of 24 spot probes (12 leading edge probes and 12 trailing edge probes) that were optimally located circumferentially around the single stage compressor to measure blade time of arrival. The integral vibrations of each blade were acquired by performing slow accelerations that traversed each mode of interest at a constant sweep rate. Multiple sweeps (both accelerating and decelerating) through each mode were performed to assess measurement repeatability for each response of interest. The NSMS signals were processed using the Sine Wave Analysis Technique (SWAT) that assumes each blade is vibrating in a sinusoidal motion as a single degree of freedom (SDOF) to provide vibration amplitudes and frequencies for each individual blade as seen in Fig. 5.6[93]. For clarity, Fig. 5.6 highlights the high, medium, and low responding blade with the remaining blade responses in grayscale to show the variability. It is interesting that the higher responding blades exhibit more of a true SDOF system response compared to the lower responding blades that show signs of modal participation from neighboring blades contributing to a

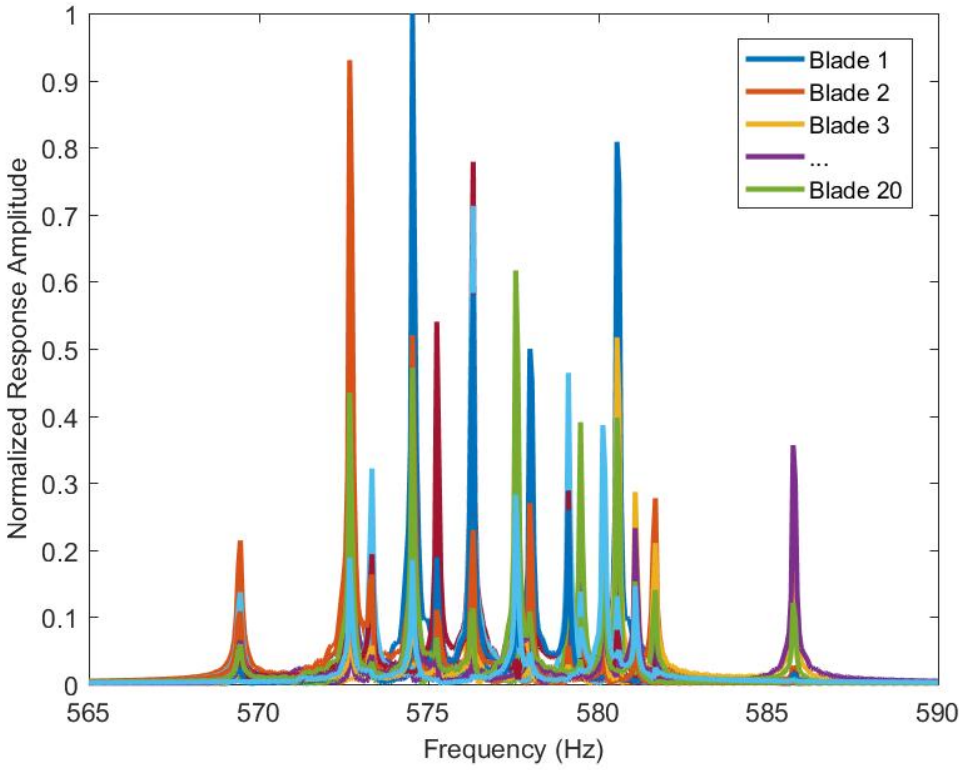

Figure 5.4: 1^{st} Bend EO4 TWE Response

single blade's response. As with the TWE response data, the rig response data from Fig. 5.6 will then be evaluated for mistuning using the system identification methods discussed in Section 5.4.

5.3.3 As-Manufactured Modeling

Both experimental methods discussed so far require substantial setup time and manpower. An alternative is to simulate both the TWE and the compressor rig environment through numerical modeling. Many researchers attempt to simulate these environments by changing parameters in FEMs to artificially insert mistuning in the system by varying properties of the IBR itself. A more geometrically accurate approach can be taken by generating an FEM

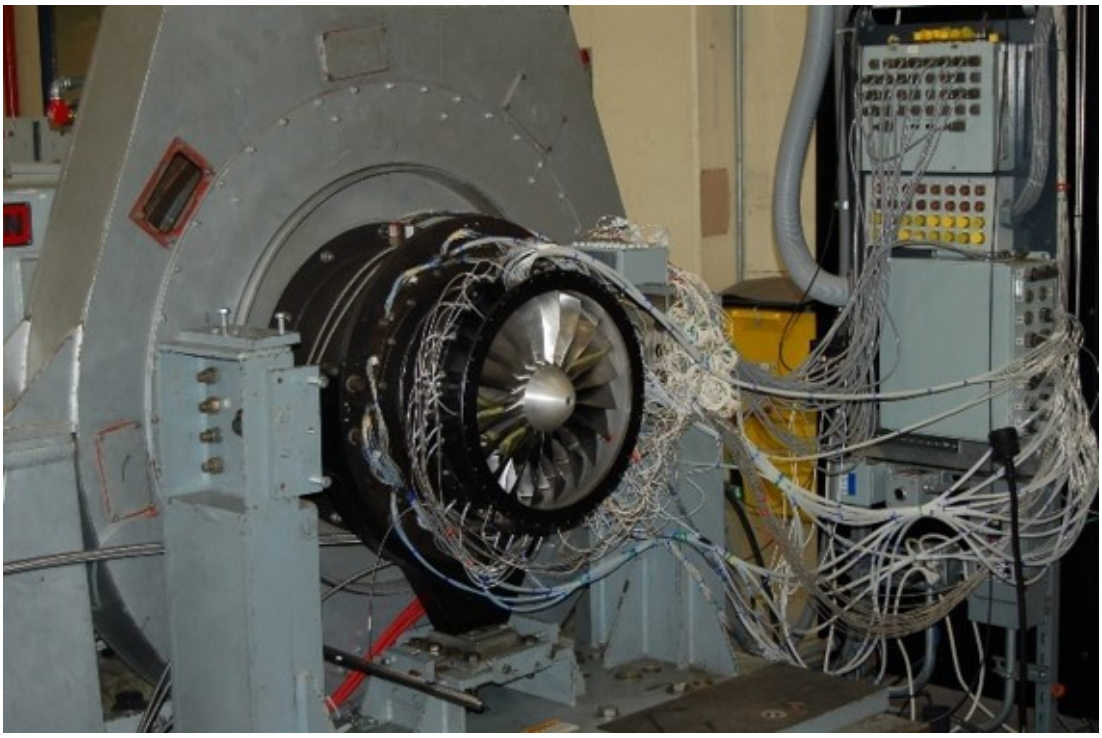

Figure 5.5: PBS R4 Compressor Rig

of the as-manufactured IBR using optical topography measurements and mesh morphing. The optical topography measurement of PBS R4 used a structured light approach with a stereoscopic camera configuration and a central light emitting diode to illuminate the part with a fringe projection. The different fringe patterns are recorded using two 8 Mega pixel cameras, and 3D coordinates are automatically calculated for each camera pixel based on optical transformation equations. These systems allow for rapid acquisition of millions of points to define geometry (i.e. point cloud) with an accuracy of ± 0.0003 inches [9, 47]. From the point cloud a simple computer aided design (CAD) model of a single, nominal sector is created and discretized into a notional, tuned FEM. The mesh morphing process updates the tuned FEM nodes to match the tessellated surface data via an iterative closest point procedure. The details of this process can be found in the works of Kaszynski et al. [9]. Fig. 4.6 shows the beginning and end of the mesh morphing process on the hub of PBS R4, where Fig. 4.6a displays the aligned tuned FEM model to the tessellated surface

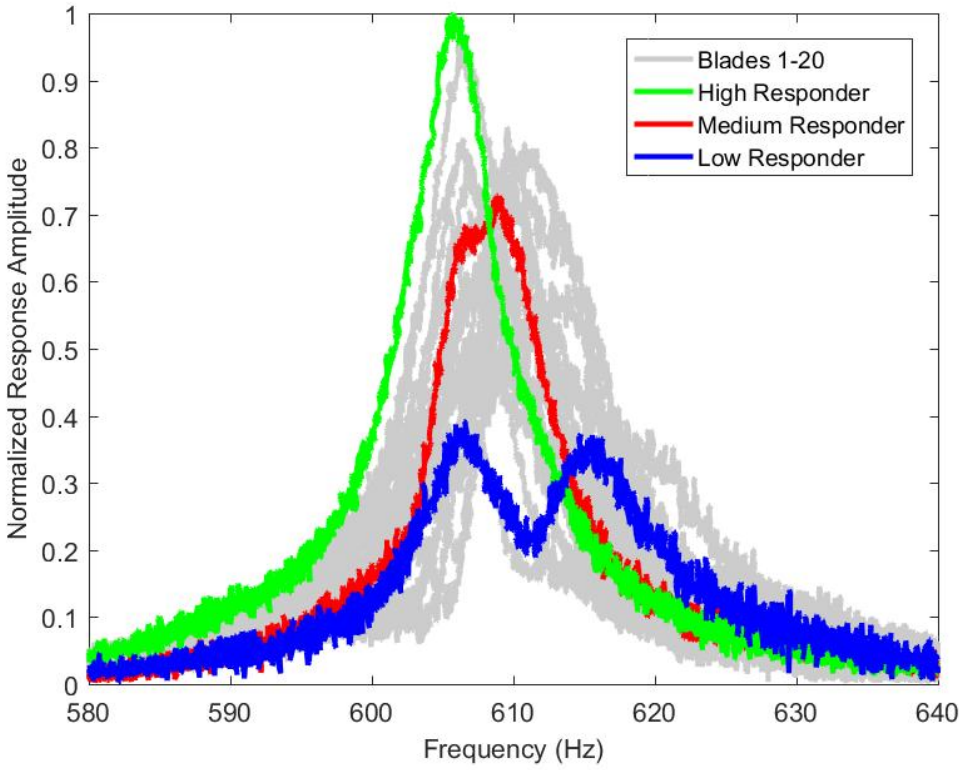

Figure 5.6: 1^{st} Bend EO4 Rig NSMS Response

data of the point cloud denoted by the white surface mesh. The contours in Fig. 4.6 display the deviation between the tuned FEM to the point cloud. There is clearly a discrepancy between the as-manufactured IBR (white surface mesh) and the tuned FEM denoted by the contours ranging from $\pm$ 0.010 inches in Fig 4.6a. Upon completion of the mesh morphing process, Fig. 4.6b shows a representative FEM of an as-manufactured IBR that is within $\pm$0.0003 inches of the tessellated point cloud. This shows the ability to create high-fidelity as-manufactured models via mesh morphing to aid in the increased understanding of IBRs.

The mesh morphing process created an as-manufactured model of PBS R4. The full FEM consists of 2,279,707 nodes and 504,480 elements composed of 95% hexahedral elements with a tetrahedral/pyramidal interface between the blade platform and the remainder of the disk. A mesh refinement study was performed to ensure the mesh was sufficiently dense as to not impact the results. It should be noted that during optical scanning PBS R4

was instrumented with strain gages on blades 1, 3, 4, 11, 13, and 14. The geometry associated with these strain gages and instrumentation wires is embedded in the as-manufactured FEMs, and the material properties associated with this volume is identical to that of the parent rotor. Therefore, artificial stiffening could potentially impact some of the comparison studies. The forced response of the rotor is simulated by applying modal superposition. Each blade is excited at the trailing edge tip with a unit magnitude force, where the force on each blade is calculated by

$$F^{(s)} = F_A \cos[\frac{2\pi C(s-1)}{N}] + jF_A \sin[\frac{2\pi C(s-1)}{N}], \quad s = 1, 2, ..., N \tag{5.1}$$

where F_A is the amplitude of the force applied, C is the EO excitation number, s denotes the blade number, and N is the number of blades. The phase at blade s is written as

$$\phi^{(s)} = \frac{2\pi C(s-1)}{N} \tag{5.2}$$

Blade loading follows the phase shift formulation identified in Eq. 5.2, where the out-of-plane displacement responses are recorded at the leading edge tip. Forced response analyses (FRA) were conducted to excite the modes of interest (Fig. 5.7) in this study with their respective EO drivers. The left column of Fig. 5.7 represents the tuned rotor case where each blade is nominal geometry (cyclically symmetric sector FEM), where the right column represents the as-manufactured or mistuned IBR (full FEM) that displays modal confinement in a single blade. This localization of energy in a single blade has the potential to create HCF issues in the field. Two separate FRAs were conducted depending on the experimental configuration of the rotor. The FRA corresponding to the stationary TWE experiment used FEM constraints with a free-free boundary condition. Similarly, the FRA corresponding to the rotating compressor rig experiment used FEM fixed constraints at the hub of the rotor with a rotational velocity matching the mode and EO driver of in-

terest. The global damping ratio for each FEM were changed to match the environment: one damping ratio for the stationary TWE environment and one damping ratio for the rotating compressor rig environment. The FEM applied global damping ratios for each mode were measured experimentally for both the TWE and compressor rig experiments, where the compressor rig damping ratio is approximately 100 times more than the TWE damping ratio. No additional aerodynamic loadings were applied to the rig FEM analyses, but could be included in the future. The as-manufactured FEM response for each blade can be seen in Fig. 5.8. Fig. 5.8a displays the response for the as-manufactured FEM for the stationary TWE simulation with a damping ratio matching measured TWE experiment, where Fig. 5.8b displays the response for the rotating compressor rig simulation with a damping ratio matching the measured compressor rig experiment. Note the difference in frequencies between the stationary and rotating experiments is due to the centrifugal stiffening effect. The increased damping in the compressor rig makes data post-processing more challenging since the modal frequencies are blended together, not isolated and well-separated as with the experimental TWE. The as-manufactured FEM responses for each blade as seen in Fig. 5.8 is then evaluated for mistuning using the system identification methods discussed in Section 5.4

5.4 Mistuning Identification Methods

The blade response data from TWE, the compressor rig, and the as-manufactured models are evaluated for both frequency mistuning and mistuning amplification using three separate mistuning identification methods. These three methods consist of the tuned absorber factor (TAF) metric, isolating individual blades experimentally and analytically to examine frequency mistuning, and finally using a reduced-order model called FMM ID. Each of these methods will be used to evaluate the mistuning for each mode and comparisons

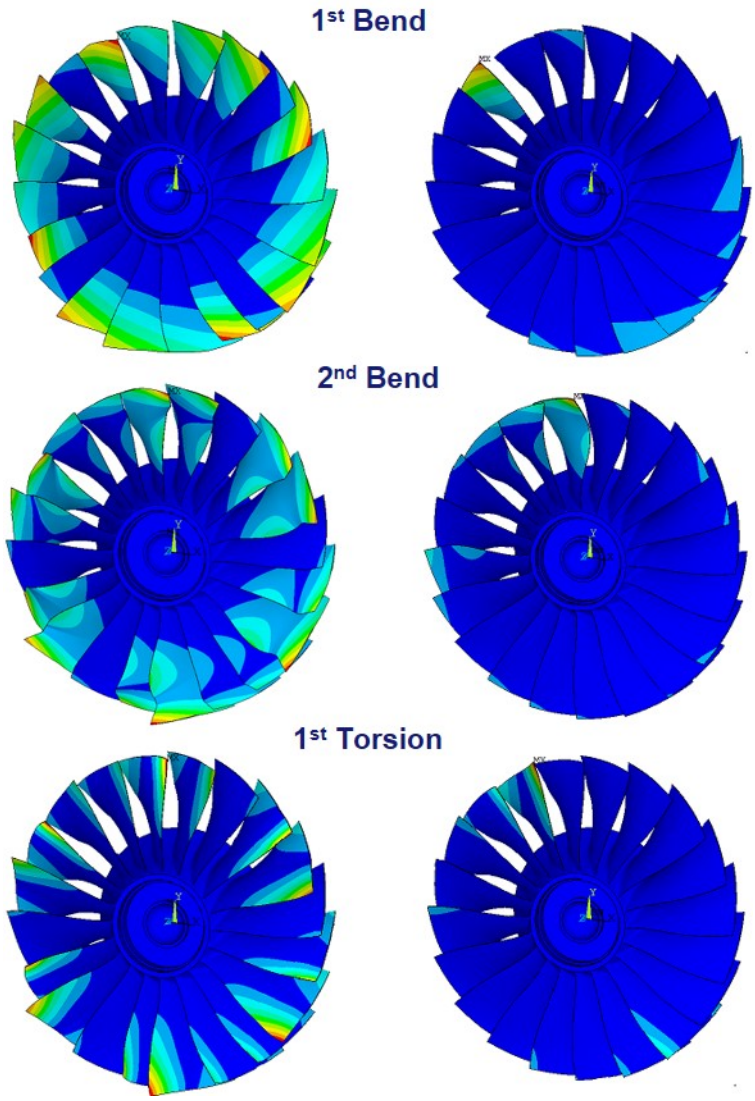

Figure 5.7: PBS R4 Mode Shapes (Tuned:Left, Mistuned:Right)

will be made not only between each mistuning identification method, but also between the fidelity of the three different test methods (TWE, compressor rig, as-manufactured models) used to acquire forced response data.

5.4.1 Tuned Absorber Factor

The tuned absorber factor is commonly used within industry as a metric to determine if any airfoils in a rotor are behaving as a "tuned absorber". No ROM is needed to determine an

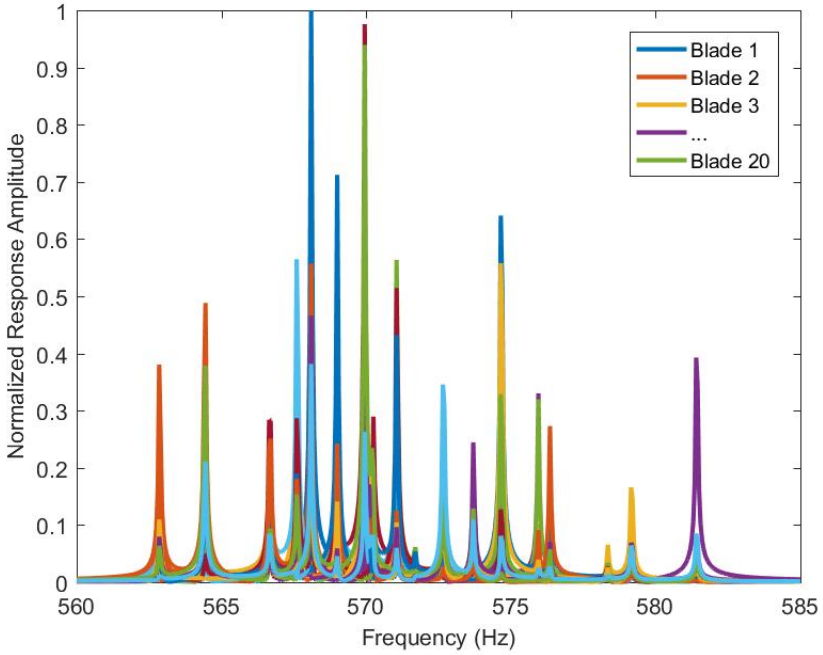

(a) Stationary TWE FEM with TWE Damping Ratio

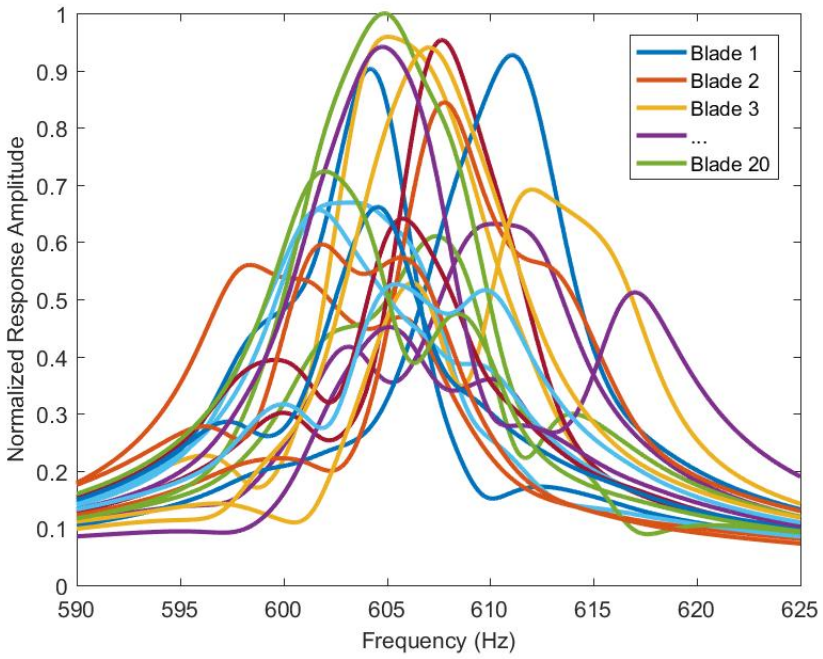

(b) Rotating Compressor Rig FEM with Rig Damping Ratio

Figure 5.8: 1^{st} Bend EO4 As-Manufactured FEM Response

IBR's TAF for a specific mode family. TAF is found by

$$TAF_s = \frac{max[U_s]}{\frac{1}{N}\Sigma_{s=1}^{N} max[U_s]}, \quad s = 1, 2, ..., N \tag{5.3}$$

where U_s is a vector of an IBR's blades leading edge tip displacement at each frequency. Note that $max[U_s]$ is the peak blade response of "Blade s". Therefore, the TAF for "Blade s" is simply the peak blade response of that blade divided by the mean of the peak responses of all the blades. Any blade with a TAF > 1 means that it is responding higher than the average of the peak responses of all the blades. Blades that have large, outlier TAF may indicate that blade could be a "tuned absorber" where most of the vibration energy is confined to that particular blade [44]. An example TAF for this IBR can be found in Fig. 5.9, where the blades are sorted from largest TAF to smallest left to right. It is evident that the IBR has potential tuned absorbers occurring in several blades for this particular mode. The TAF for each mode and for each method will be analyzed and compared to determine whether TAF is a suitable metric to evaluate a IBR's amplification.

5.4.2 Isolated Blade Frequencies

The second method to determine the frequency mistuning is based on isolated blade frequencies, which is accomplished by both analytical and experimental means. Analytically speaking, isolated sector frequencies are accomplished using separate cyclically symmetric models of each blade sector for PBS R4. Each sector represents the actual geometry for that blade and the cyclic regions on the disk are constrained. A modal analysis is performed to determine the natural frequency for the modes of interest for each isolated geometrically morphed blade sector model, i.e., 20 separate as-manufactured individual blade FEMs. The frequency deviation for each bladed sector is found by

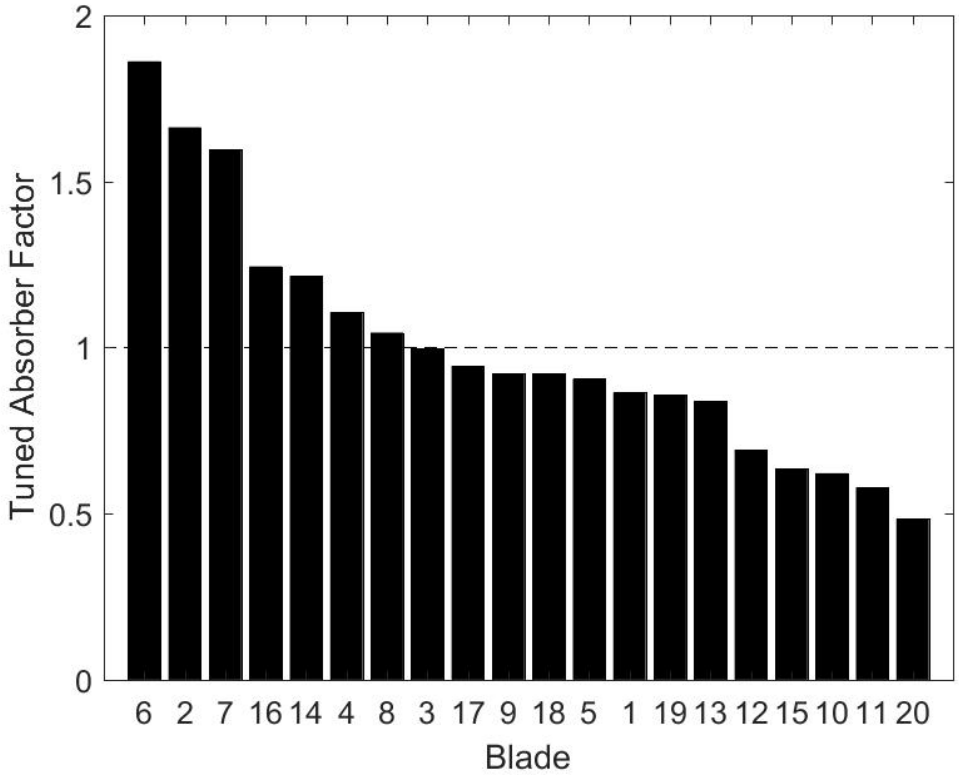

Figure 5.9: Example Tuned Absorber Factor

$$\frac{\delta\omega_{j,i}}{\bar{\omega_j}} = \frac{\omega_{j,i} - \bar{\omega_j}}{\bar{\omega_j}} \tag{5.4}$$

where $\omega_{j,i}$ corresponds to the j^{th} mode for the i^{th} blade and $\bar{\omega_j}$ corresponds to the mean natural frequency for that mode family. Isolating blades experimentally presents more of a challenge. Research in the past detuned the system by using additional masses [10]. The detuning mechanism used in the current study used a series of damping pads between each blade except the blade of interest as seen in Fig. 5.10. The single isolated blade is excited using only the electromagnet for that particular blade, and the vibration response for that blade is measured using a laser scanning vibrometer as was the case during the TWE experiments. Fig. 5.11 shows the individual blade response with the damping pads installed. It is readily apparent that the approach outlined is able to identify blade alone frequencies of

this rotor. This isolated blade frequency approach will be used as a benchmark to evaluate the geometrically mistuned blade sectors to the actual PBS R4. Note that it is not possible to "isolate" the blades during the compressor rig runs, but the compressor rig blade natural frequencies as defined by the SWAT analysis will still be compared to both the isolated blade benchtop experimental tests and as-manufactured FEMs. This is done merely as an exercise to see how well isolated blade mistuning alone can represent rig/engine conditions.

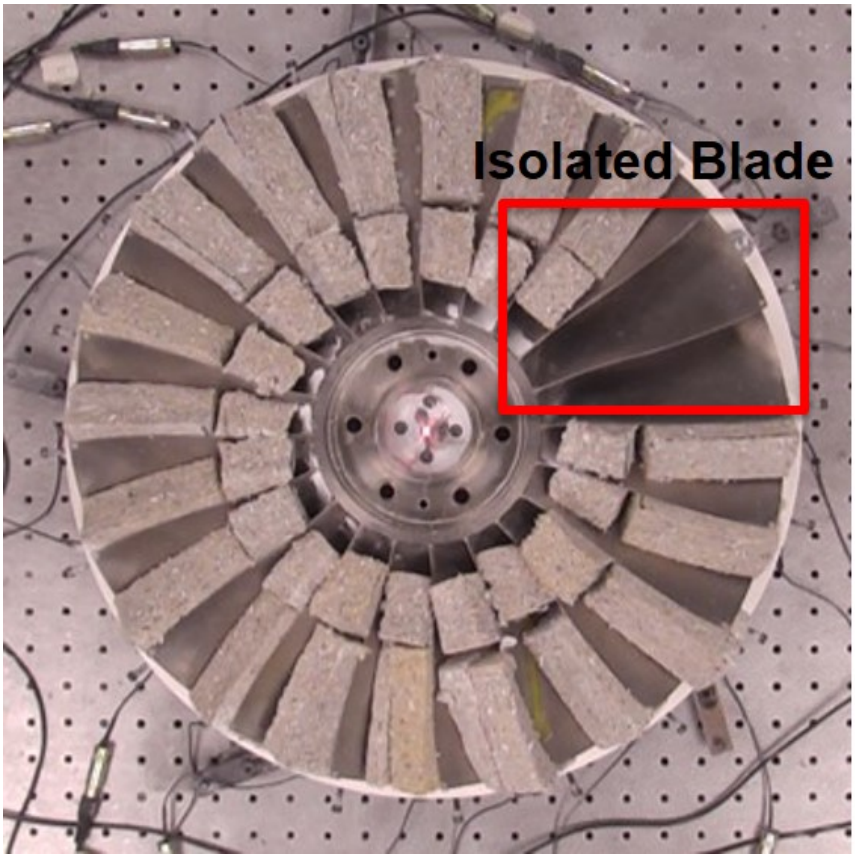

Figure 5.10: PBS R4 Isolated Blade Ping Testing

5.4.3 FMM ID

The last mistuning identification method investigated is a reduced-order mistuning model called the Fundamental Mistuning Model Identification (FMM ID) developed by Feiner &

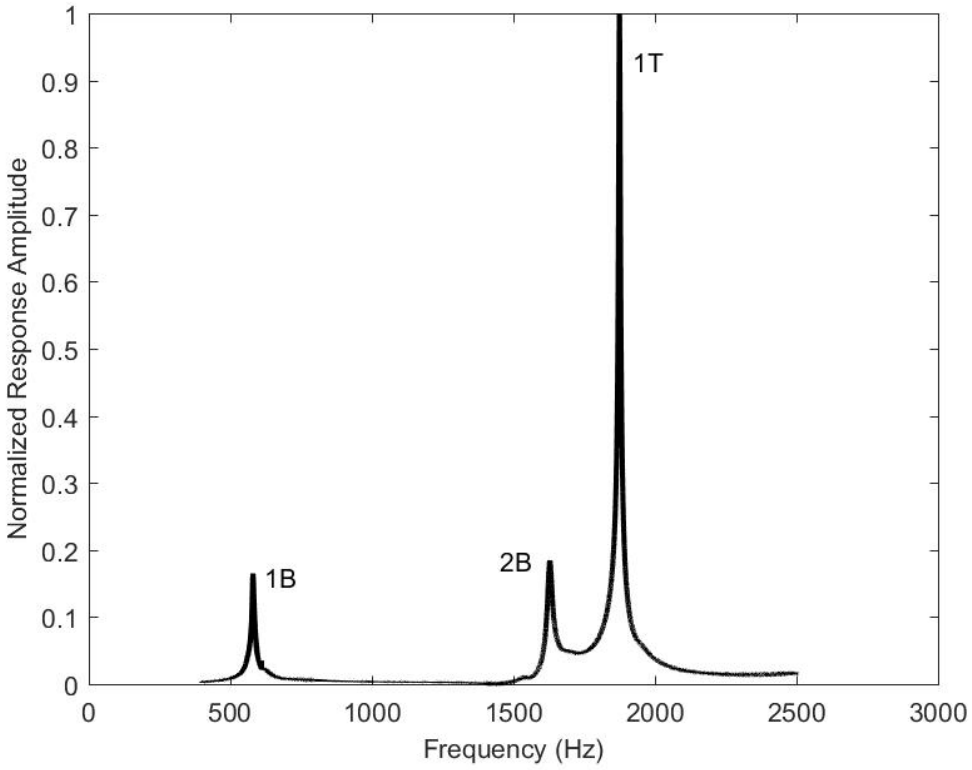

Figure 5.11: Individual Blade Response Isolated Blade

Griffin[31–33]. The basic form of FMM ID uses inputs of only the tuned system frequencies, but the advanced version of FMM ID requires inputs solely based on experimental (or analytical) data. Using Advanced FMM ID, the tuned and mistuned forced response results are predicted with identified parameters and the FMM model. FMM is a very efficient ROM of mistuning that operates under the assumption of an isolated mode family, thereby reducing prediction inputs to the tuned system frequencies and frequency deviation of each blade. Fig. 5.12 displays the nodal diameter map for PBS R4. The three modes of interest are 1_{st} bend (1B), 2_{nd} bend (2B), and 1_{st} torsion (1T) which are all well-isolated from other modes, making them all valid candidates for FMM ID. Errors from measurement variation can be reduced by using blade response data from several system modes from the same family. Mistuning amplification is predicted using the predicted tuned system frequencies, sector frequency deviations, EO, and assumed damping ratio. For comparison purposes,

FMM ID was used to evaluate the mistuning using the response amplitude and phase results from TWE, the compressor rig, and the different as-manufactured models. To predict the mistuning amplification, different damping ratios were assumed whether comparisons were being made between TWE or the compressor rig. Repeatability studies were performed to ensure the inputs from TWE and the compressor rig simulations were providing consistent FMM ID predictions.

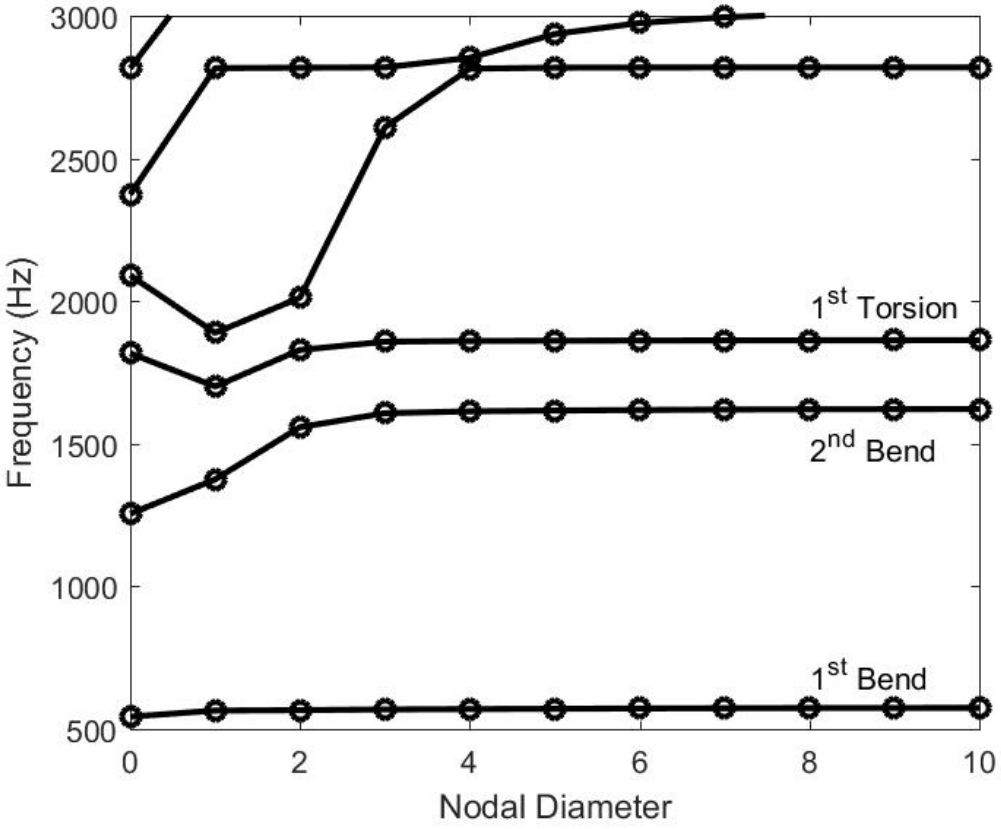

Figure 5.12: Nodal Diameter Map

5.5 Results

Both the mistuning pattern and the mistuning amplification between TWE, the compressor rig, and the as-manufactured model is compared using the three mistuning identification methods identified. The as-manufactured model will be referred to as the geometric mistuned model (GMM) over the course of the comparison. This is accomplished using the IBR designated as PBS R4 as previously discussed for its first bending mode (EO3 and EO4 excitation), second bending mode (EO7 excitation), and first torsion mode (EO7 excitation). These mistuning evaluation techniques will be compared to see how they transition from the analytical domain to the bench and then to the real world environment. The Pearson correlation coefficient, R, is used as a metric to compare each test method. The coefficients can range between -1 and 1, where -1 is a perfect negative correlation, 0 is no correlation, and 1 is a perfect positive correlation between two methods being compared.

5.5.1 Tuned Absorber Factor

Upon completion of experimental and analytical testing, the TAF for each mode and for each method was calculated according to Eq. 5.3. Three different as-manufactured (GMM) simulations were used to compare to the TWE experiment and compressor rig tests. The first GMM model simulates the TWE environment. The other two GMM models simulate the compressor rig with rotational velocities matching each mode. The global damping (Q) in the FEM was varied in the rig simulated GMM model. One damping term simulated the damping measured during TWE testing for each mode denoted as “TWE Q”, where one damping term simulated the damping measured during the compressor rig testing for each mode denoted as “RIG Q”. The global damping for the rig model was varied to determine if the post-processing techniques utilized for the heavier damped system needs refinement. The description of the different as-manufactured FEMs developed are shown in Table 5.1.

The maximum TAF for each experimental/analytical method as a function of the ex-

Table 5.1: As-Manufactured (GMM) Simulations

Descriptor	Environment	Boundary Condition	Damping (Q)
GMM TWE	TWE	Free-Free	TWE
GMM RIG (TWE Q)	RIG	Fixed Hub	TWE
GMM RIG (RIG Q)	RIG	Fixed Hub	RIG

cited mode is shown in Fig. 5.13. A variation in the maximum TAF for each method is visible across each mode analyzed. 1^{st} bend EO3 has a 33% variation, 1^{st} bend EO4 a 40% variation, 2^{nd} bend a 132% variation (18% variation with the TWE outlier removed), and 1^{st} torsion a 32% variation. The largest discrepancy in TAF occurs in the 2^{nd} bend mode, where the TWE TAF is substantially greater than the other methods. The calculated TAF for this mode was consistent over multiple TWE experiments and always occurred on the same blade. The TAF outlier could be one indication of why TAF may not be the most suitable predictor of potential blade amplification on IBR's. TWE, GMM TWE, and GMM RIG (TWE Q) consistently over predict the TAF of the compressor rig across each mode. Additionally, the TAF associated with GMM RIG (TWE Q) is larger than the TAF for GMM RIG (RIG Q) across each mode. Lastly, the TAF GMM RIG (RIG Q) is scattered about the TAF for the actual rig. This provides an indication the rig global damping GMM model presents an adequate representation of the rig conditions, where the TWE global damping GMM models consistently predict an over prediction of the TAF compared to rig.

The potential "tuned absorber" blade does not necessarily translate across the methods, i.e., the maximum TAF does not occur on the identical blade across the three methods. To illustrate the discrepancy between the maximum blade responders, Table 5.2 highlights the maximum TAF for each method as well as the blade at which this TAF occurs. Of the modes of interest, the average maximum TAF across each method falls between $1.60-1.65$. A typical large TAF occurs in ranges greater than 2.0, so the system being analyzed here appears to have a moderate level of amplification across the modes of interest. It remains to be investigated if better correlation between the different methods would be experienced

with respect to prediction of the “tuned absorber” blade if the same study were to be performed on a system with a greater level of amplification.

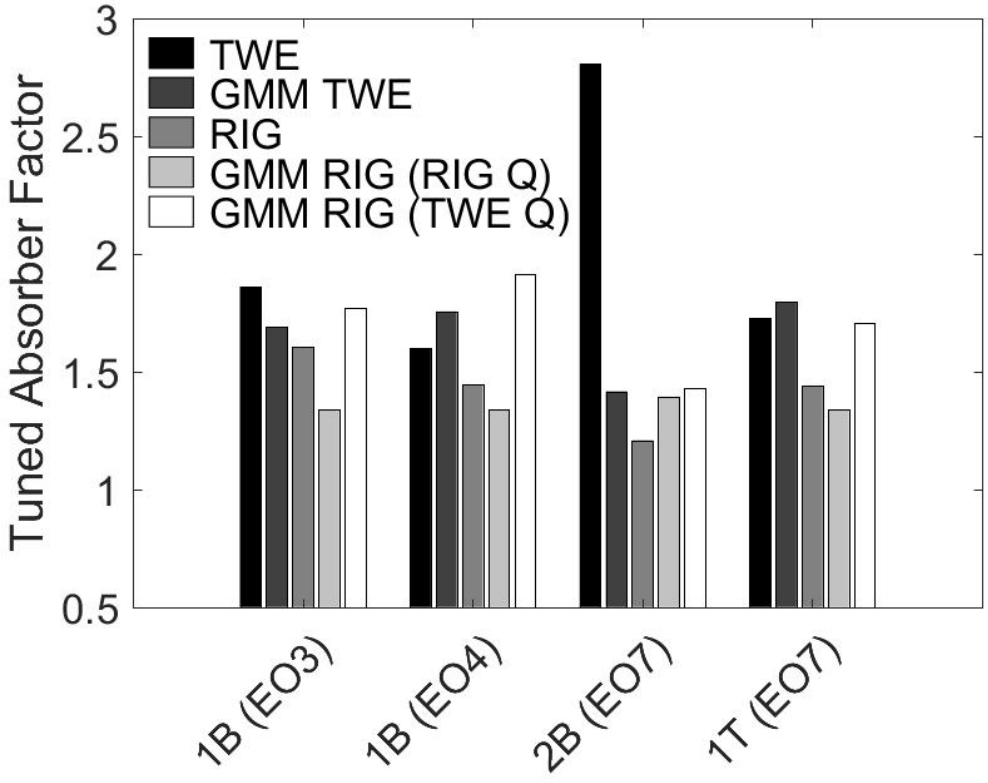

Figure 5.13: Maximum TAF Comparison

5.5.2 Frequency Mistuning

The frequency mistuning of the PBS R4 rotor is now investigated using those methods identified in Sections 5.4.2 and 5.4.3. Comparisons will be drawn between the various methods by examining the sector mistuning as a function of blade number. The Pearson correlation coefficient (R) is used as a metric to determine the compatibility between the various experimental and analytical methods.

Table 5.2: Tuned Absorber Factor Comparisons

Method	1^{st} Bend (EO3)		1^{st} Torsion (EO7)	
	Max TAF	Blade	Max TAF	Blade
TWE	1.86	6	1.73	11
RIG	1.60	16	1.44	3
GMM TWE (TWE Q)	1.69	16	1.80	19
GMM RIG (TWE Q)	1.77	3	1.71	18
GMM RIG (RIG Q)	1.34	9	1.34	6

Isolated Blades

Using the methods to isolate blades both experimentally and analytically using the GMM cyclic blade FEMs previously discussed, the frequency deviations are compared between the isolated experiments, the compressor rig, and the as-manufactured models. Fig. 5.14 displays the frequency deviations for each mode and method as a function of blade number. The correlation coefficient for each mode was calculated with respect to the isolated experimental (EXP) results. Note that Fig. 5.14 highlights the EO driver for each mode. The isolated experiments and the isolated FEMs have no EO drivers for this comparison, and the EO drivers are only taken into account for the non-isolated compressor rig tests.

The 1^{st} bend mode with different engine order excitations is analyzed first, where Fig. 5.14a and Fig. 5.14b show the frequency deviations for this mode. Note that the EO3 harmonic excitation is from the upstream distortion screen present during the compressor rig test, and the EO4 harmonic excitation is from the downstream struts in the compressor rig. The 1^{st} bend EO3 and EO4 frequency deviations show good agreement (R = 0.86) between the experimental isolated blades and the as-manufactured (GMM) individual blade sector FEMs. As anticipated, the compressor rig frequency deviations show a weak correlation for both the EO3 and EO4 mode due to system modes participating in the coupled compressor rig rotor system.

Both the 2^{nd} bend and 1^{st} torsion modes are excited with an EO7 harmonic excitation that is generated through a combination of aerodynamic drivers and fixed rig components.

Fig. 5.14c shows the frequency deviations for the 2^{nd} bend mode that shows excellent agreement (R = 0.91) between the experimental isolated blades and the as-manufactured (GMM) individual blade sector FEMs. The compressor rig sector mistuning correlation to the isolated experiment is more comparable with a correlation coefficient of 0.81, implying less system participation and more blade dominance. Fig. 5.14d display the frequency deviations for the 1^{st} torsion mode. There exists less correlation (R = 0.66) between the isolated experimental tests and the isolated FEMs for this mode compared to the other studied modes. Alternatively, the 1^{st} torsion mode compressor rig sector mistuning correlation to the isolated experiment is exceptional (R = 0.93), again implying a more blade dominant mode and less system level influences. Partly bad correlation between EXP/GMM for the 1^{st} torsion mode could potentially be a ramification of the metal disks used to excite the mode experimentally since the . However, if this were the case then bad correlation would also be anticipated for EXP/RIG (R = 0.93). Significant frequency deviations can be seen in Fig. 5.14d on blade 11, on which strain gages are present. The artificial stiffening of the gages and instrumentation wires in the GMM isolated blade models could have a stronger effect on the 1^{st} torsion mode more so than the bending modes. Hence, this is the more likely indication for poor correlation between EXP/RIG.

A complete set of correlation coefficients comparing each method is given in Table 5.3 showing positive correlation between the experiment and as-manufactured sector models for the 1^{st} and 2^{nd} bending modes and slightly less correlation for the 1^{st} torsion mode. This provides evidence that the as-manufactured models are doing an adequate job capturing the physics associated with the rotor during the TWE experiments. Table 5.3 also shows weak correlation between experimental/rig and rig/GMM for the 1^{st} bend modes with increased correlation for both the 2^{nd} bend and 1^{st} torsion modes. The true comparison with the rotating compressor rig sector mistuning will occur with non-isolated blades, but these comparisons do help provide an indication of the amount of potential system activity for

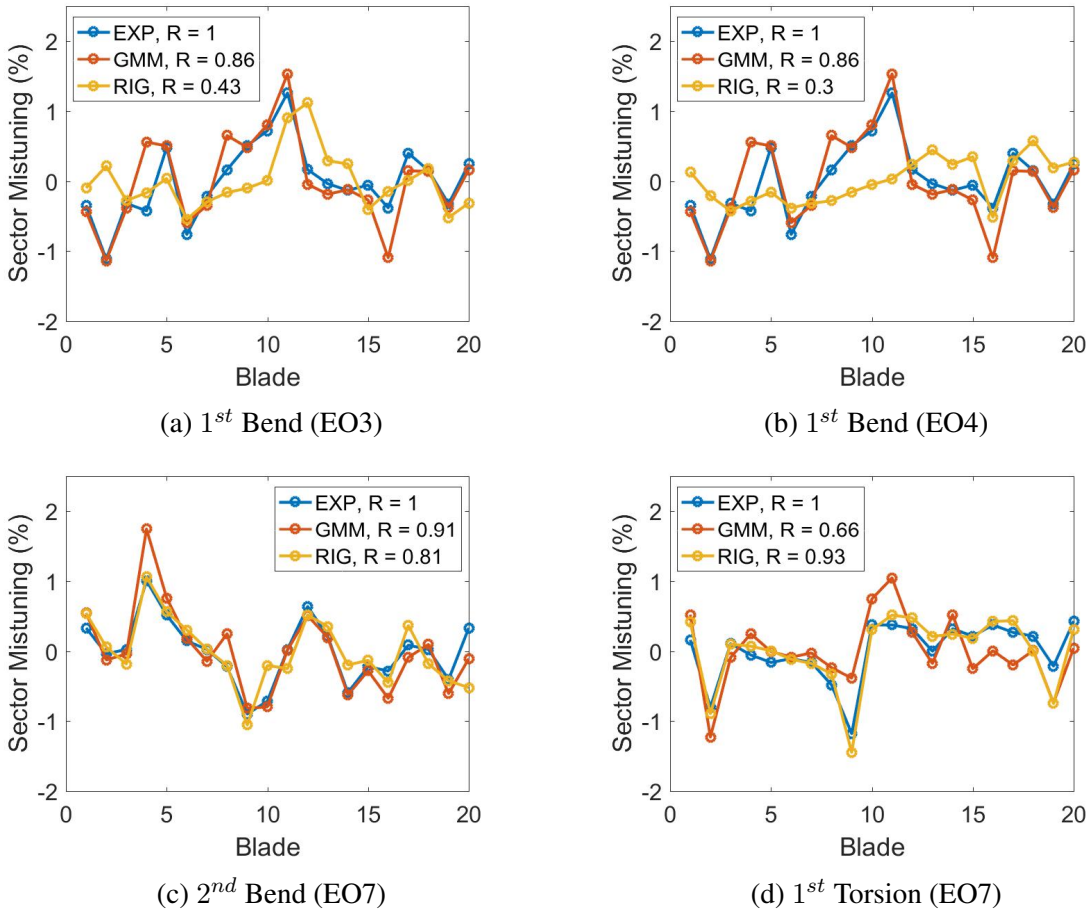

(a) 1^{st} Bend (EO3)

(b) 1^{st} Bend (EO4)

(c) 2^{nd} Bend (EO7)

(d) 1^{st} Torsion (EO7)

Figure 5.14: Isolated Blades Sector Mistuning

each mode.

Non-Isolated Blades

Previously, frequency mistuning investigated only isolated blades and compared isolated blades on the benchtop experiment to isolated as-manufactured blade FEMs. However, in an engine and/or a rig the blades are not isolated and are able to interact with one another. To better compare to this setup, TWE is able to simulate engine order excitation seen in a rig/engine and the same can be accomplished using high-fidelity, as-manufactured models. This section analyzes the blade response data collected during TWE testing, compressor rig testing, and through various as-manufactured models and utilizes FMM ID to calculate

Table 5.3: Isolated Blades Correlation Coefficients

Method Comparisons		Correlation Coefficient (R) 1B-EO3	1B-EO4	2B-EO7	1T-EO7
EXP	GMM	0.86	0.86	0.91	0.66
EXP	RIG	0.43	0.30	0.81	0.93
RIG	GMM	0.35	0.16	0.84	0.70

the sector mistuning.

The sector mistuning calculated via FMM ID as a function of blade number for each mode can be seen in Fig. 5.15. The sector mistuning for each mode varies anywhere between -1.5% to $+2.0\%$ as it did with the isolated bladed sector study. As expected, Fig. 5.15a and Fig. 5.15b show much better agreement between the predicted compressor rig mistuning, TWE, and the various full rotor GMM models compared to the isolated blades (Fig. 5.14a and Fig. 5.14b). The 1^{st} bend modes do exhibit noticeable sector mistuning variation. However, the overall rig mistuning trend for this mode is successfully predicted using TWE and various as-manufactured FEMs. Additionally, the rig mistuning patterns for the 2^{nd} bend (Fig. 5.14c) and 1^{st} torsion (Fig. 5.14d) modes are successfully predicted using both TWE and various as-manufactured models.

Significant frequency deviations between the GMM and experimental methods are visible for blade 4 (Fig. 5.14a, Fig. 5.14b) and for blade 11 (Fig. 5.14d). Strain gages are applied to both of these blades and the artificial stiffening of the instrumentation volumes in the as-manufactured FEMs could play a factor. Changing the damping of the GMM model displayed a small shift in the calculated sector mistuning. This can be minimized by reducing the error associated with defining the inputs into FMM ID. The damping on the rig is roughly 100 times greater than on the TWE experiment, and this increase in damping makes it difficult to distinguish between modes. The TWE response spectrum has very well-isolated modal responses that are easily distinguishable, but the large damping experienced on the rig makes it more difficult to distinguish between the modes. This is a

key input into the FMM ID model and refinements in this process when experiencing large damping will be investigated in future work.

The error associated with each method comparison were found to be random by performing a linear regression model on the actual vs. predicted sector mistuning. An example of the randomness associated with the different methods is provided in Fig. 5.16 for the 2^{nd} bend mode with no clear anomalies present. To provide a more complete comparison between each method, the correlation coefficients comparing each method is given in Table 5.4. There is excellent agreement between TWE and GMM TWE for the 1^{st} and 2^{nd} bending modes and slightly less correlation for 1^{st} torsion. This reaffirms the physics associated with the as-manufactured models is capturing the TWE setup adequately. The weakened correlation for the 1^{st} torsion mode could again be a ramification of strain gages present on the rotor at the time of optical scanning. There exists a general agreement between TWE and RIG across each mode with better correlation existing for the 2^{nd} bend and 1^{st} torsion modes. However, it appears the TWE is potentially lacking some of the physics occurring in the compressor rig. A basic agreement exists between the RIG and the as-manufactured FEM models with various damping ratios. Changing the damping ratio on the GMM RIG model did have an effect on the correlation between each method, i.e., the algorithms to identify FMM ID inputs on systems with large damping needs to be further refined. The correlation between the GMM RIG models with different damping levels themselves was excellent with R-values greater than 0.93 for each mode. Integrating aerodynamic loads into the as-manufactured model may have the ability to improve the GMM to RIG correlation. It is evident that both TWE and the as-manufactured models are able to compare mistuning patterns well to the compressor rig across each mode analyzed.

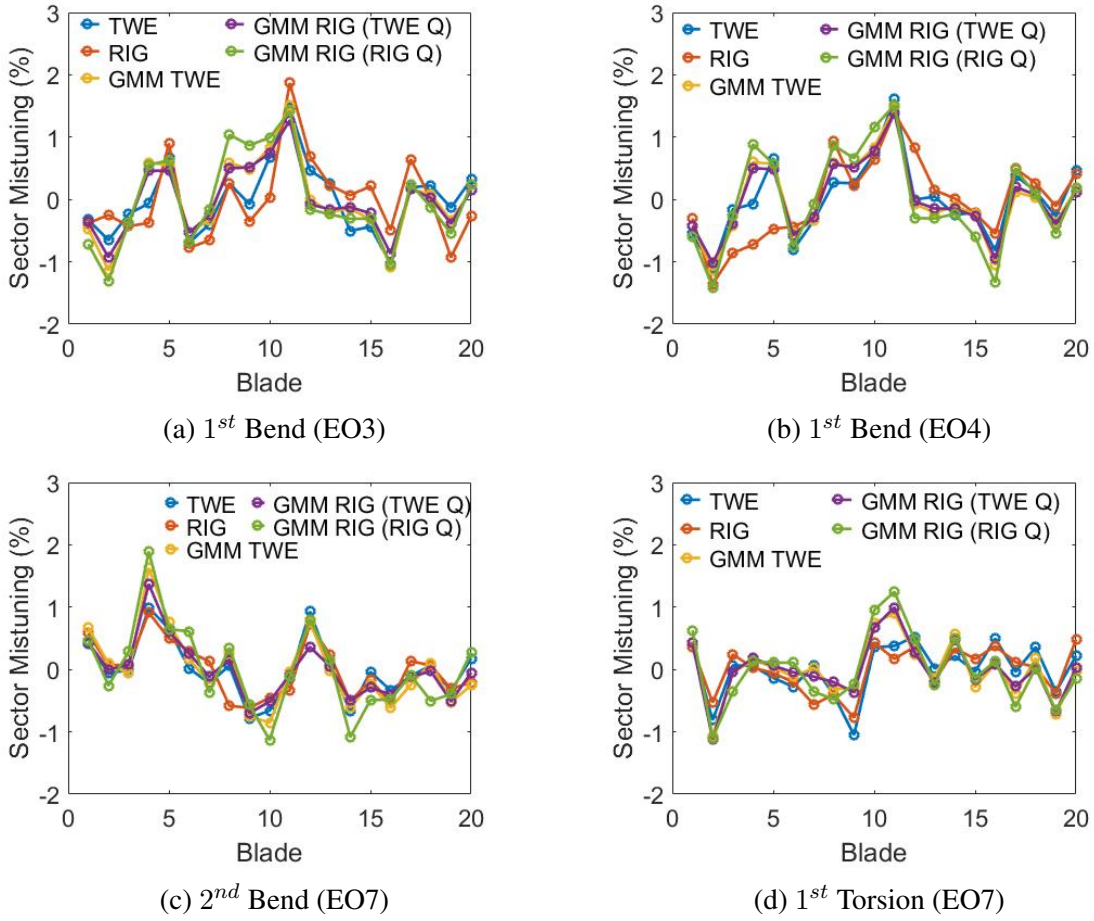

(a) 1^{st} Bend (EO3)

(b) 1^{st} Bend (EO4)

(c) 2^{nd} Bend (EO7)

(d) 1^{st} Torsion (EO7)

Figure 5.15: FMM ID Non-Isolated Blades Sector Mistuning

5.5.3 Force Amplification

The ultimate goal is to predict the forced response amplification due to identified mistuning patterns. Mistuned response amplification is predicted via FMM ID using the predicted tuned system frequencies, sector frequency deviations, EO, and assumed damping ratio. Different damping ratios were used as inputs into FMM ID: one damping term simulated the damping measured during TWE testing for each mode denoted as "TWE Q" or "TWE DAMPING"; the other simulated the damping measured during the compressor rig testing for each mode denoted as "RIG Q" or "RIG DAMPING". An example of the FMM ID predicted mistuned response amplification for each test method being analyzed can be seen in Fig 5.17, which is for the 1^{st} bend mode with an EO4 excitation. Individual blade

Table 5.4: FMM ID Predicted Sector Mistuning Correlation Coefficients

Method Comparisons		Correlation Coefficient (R) 1B-EO3	1B-EO4	2B-EO7	1T-EO7
TWE	GMM TWE	0.87	0.92	0.94	0.74
TWE	RIG	0.77	0.76	0.86	0.84
TWE	GMM RIG (TWE Q)	0.86	0.93	0.91	0.74
TWE	GMM RIG (RIG Q)	0.80	0.89	0.89	0.66
RIG	GMM TWE	0.64	0.70	0.85	0.63
RIG	GMM RIG (TWE Q)	0.65	0.72	0.84	0.67
RIG	GMM RIG (RIG Q)	0.57	0.65	0.77	0.60
GMM RIG (TWE Q)	GMM RIG (RIG Q)	0.98	0.98	0.93	0.95

responses in Fig 5.17 are denoted by different colors. The mistuned response amplification for each method is all calculated relative to the tuned response. It can be seen that for this mode the response relative to tuned falls below 1.5 for each method.

The maximum mistuning amplification for each experimental/analytical method as a function of the excited mode can be seen in Fig. 5.18. The methods of TWE, GMM TWE, and GMM RIG (TWE Q) all assume a damping input into the FMM ID model that emulates the damping measured during TWE testing for each mode. Alternatively, the methods of RIG and GMM RIG (RIG Q) assumes a damping input into the FMM ID model that emulates the damping measured during the compressor rig tests for each mode. A noticeable variation in the maximum mistuned response amplification for each method is visible across each mode analyzed. A linear regression model on the actual vs. predicted mistuning amplification was developed for each method comparison, and the error was found to be random with no indications of bias in the data.

Regardless of the FMM ID input of damping ratio, the predicted mistuning amplification falls below 1.5 with the exception of one case. This is a marginally low predicted amplification[94], where it is more difficult to predict lower levels of mistuning amplification. Therefore, the variation associated with each method could potentially be within the noise. It would be expected that the predicted mistuning amplification between TWE

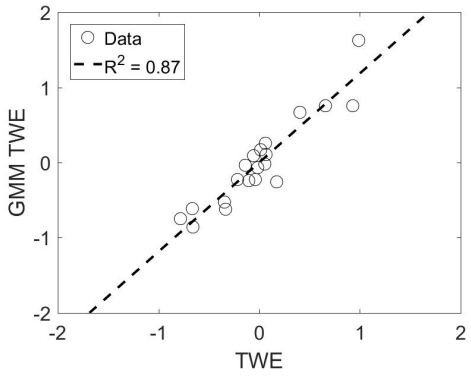

(a) TWE vs. GMM TWE

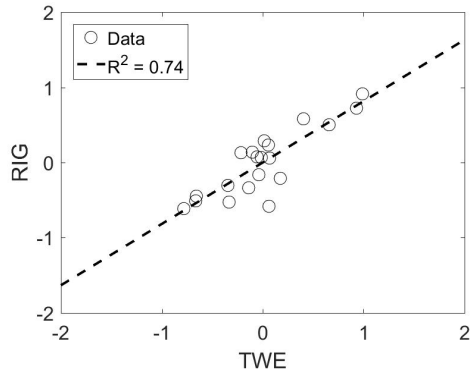

(b) TWE vs. RIG

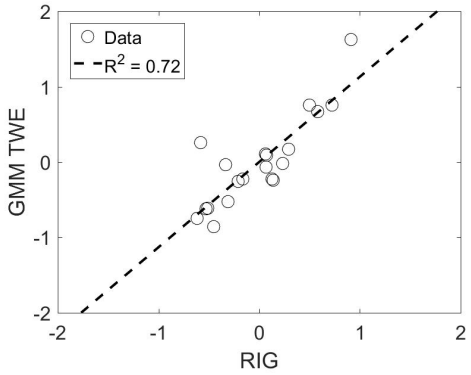

(c) RIG vs. GMM TWE

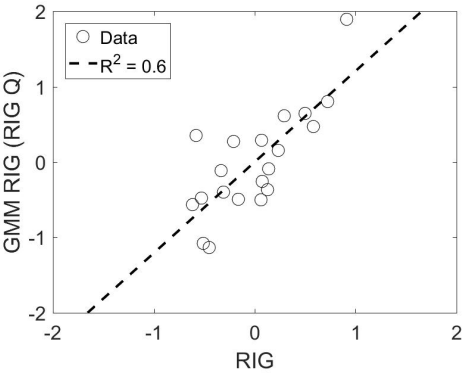

(d) RIG vs. GMM RIG

Figure 5.16: 2^{nd} Bend Actual vs. Predicted Sector Mistuning (%)

and GMM TWE would be more comparable as these two systems are the only two systems that actually exhibit "TWE damping levels", but there is a clear variation for each mode between the two. Potential contributors for this variation could be the assumed free-free boundary condition in the as-manufactured GMM TWE model or possibly a variation in material properties that were different than assumed. Additionally, it would be anticipated that the predicted amplification between RIG and GMM RIG (RIG Q) would be comparable since these are the only two systems that actually exhibit "RIG damping levels", and it can readily be seen that the as-manufactured FEM with assumed rig damping does indeed compare to the actual RIG amplification very well across each mode. The favorable comparison between RIG and GMM RIG (RIG Q) is an indication that the fixed hub boundary conditions along with the pre-stressed forced response analyses provide a realistic imitation

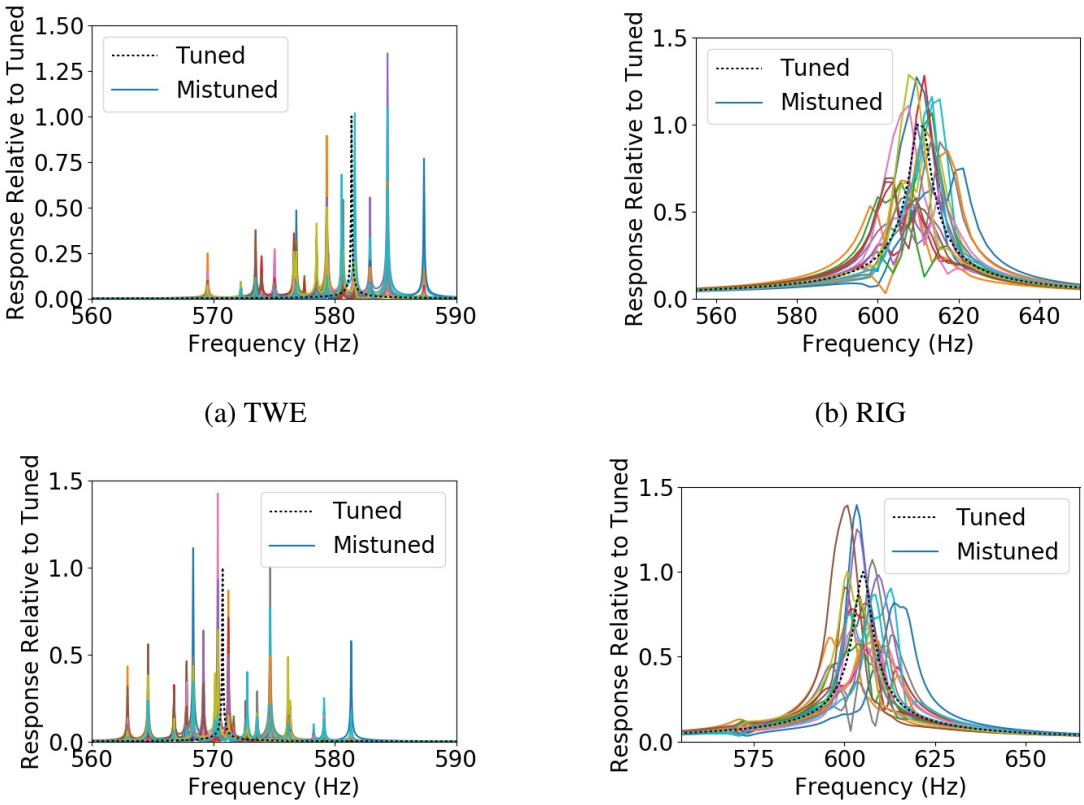

(a) TWE

(b) RIG

(c) GMM TWE

(d) GMM RIG

Figure 5.17: 1^{st} Bend EO4 Predicted Mistuning Amplification

of the actual compressor rig test. Simulating the compressor rig with a TWE damping ratio via GMM RIG (TWE Q) did not provide a good comparison (with the exception of 2^{nd} bend) to the actual RIG predicted mistuning amplification. Neither TWE nor GMM TWE had a positive correlation to the RIG mistuning amplification. TWE conditions cannot simulate blade untwisting, boundary conditions, additional damping, signal noise, and blade pressures associated with an actual compressor rig test. FMM ID predictions are capable of errors as well. There does exist a general agreement between each method despite low mistuning amplification levels.

However, the maximum responding blade does not necessarily translate across the methods. To illustrate the discrepancy between the maximum blade responders, Table 5.5 highlights the maximum mistuning amplification for each method as well as the blade

at which this max amplification occurs. The 1^{st} bend mode has significant variation in maximum blade responders. This mode does have some disk participation, where one of FMM ID's assumption is a blade dominant mode. Significant variation in the maximum blade responders also exists for both 2^{nd} bend and 1^{st} torsion with respect to TWE and GMM TWE. Yet, when comparing the maximum responder between RIG and GMM RIG (RIG Q) for these two modes the predicted maximum responding blade is only a single blade off. It is important to note that each of these modes have relatively low predicted mistuning amplification, so the deviation in predicted blades could fall within the noise. Future work will investigate if better correlation between the different methods would be experienced with respect to prediction of the max responding blade if the same study were to be performed on a heavily mistuned system. It is evident that utilizing the discussed as-manufactured modeling approach of PBS R4 to account for the actual geometric deviations appears to be a viable option to predict mistuned response amplification, even for systems that are not heavily mistuned.

Table 5.5: Mistuning Amplification Comparisons

(a) 1^{st} Bend Mode

Method	1^{st} Bend (EO3)		1^{st} Bend (EO4)	
	Max TAF	Blade	Max TAF	Blade
TWE	1.45	10	1.19	12
GMM TWE	1.17	15	1.43	7
RIG	1.32	14	1.33	1
GMM RIG (RIG Q)	1.30	19	1.39	16
GMM RIG (TWE Q)	0.95	16	1.16	18

(b) 2^{nd} Bend & 1^{st} Torsion Modes

Method	2^{nd} Bend (EO7)		1^{st} Torsion (EO7)	
	Max TAF	Blade	Max TAF	Blade
TWE	1.09	4	1.13	17
GMM TWE	1.47	12	1.65	19
RIG	1.28	7	1.28	5
GMM RIG (RIG Q)	1.28	6	1.22	6
GMM RIG (TWE Q)	1.31	11	1.05	19

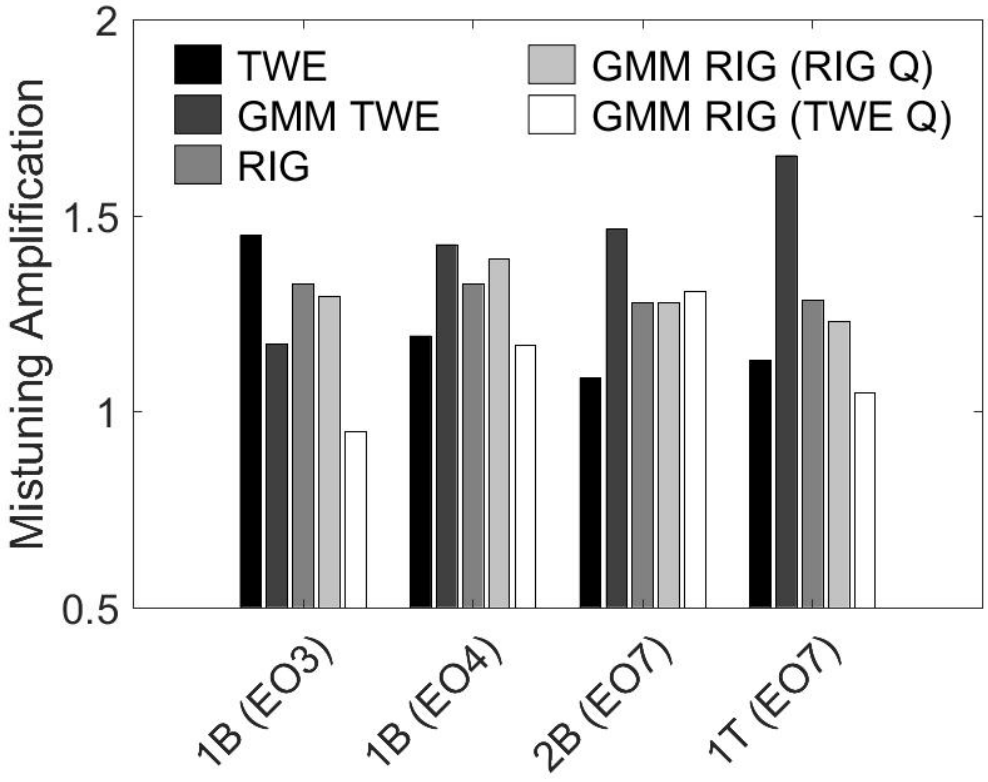

Figure 5.18: Maximum Mistuning Amplification Comparison

5.6 Conclusions

A comprehensive mistuning evaluation was conducted for a 20 bladed IBR. Three separate modes were evaluated: 1^{st} bend with both an EO3 and EO4 excitation, 2^{nd} bend with an EO7 excitation, and 1^{st} torsion with an EO7 excitation. The modes were excited using three different test methods: a benchtop traveling wave excitation, a rotating compressor rig with inlet distortion, and using geometrically mistuned FEM as-manufactured models. Mistuning was evaluated using three separate methods: tuned absorber factor (TAF), isolated blades to generate mistuning patterns, and using a reduced-order model called FMM ID.

The commonly referred industry mistuning term "tuned absorber factor" (TAF) showed variability between TWE, RIG, and the as-manufactured GMM models providing indica-

tions that TAF may not be the most suitable approach for predictions of potential blade amplifications on IBRs. However, it was found that TWE, GMM TWE, and GMM RIG (TWE Q) consistently over predicted the TAF compared to the rig where the GMM RIG (RIG Q) as-manufactured models appeared to provide an adequate representation of the compressor rig conditions when analyzing TAF.

Isolating individual blades both experimentally and analytically displayed a positive frequency mistuning correlation between TWE and the as-manufactured cyclically symmetric blade GMM models for 1^{st} and 2^{nd} bend with slightly less correlation to 1^{st} torsion. The potential factor influencing the 1^{st} torsion comparisons could be a ramification of strain gages being present on the IBR at the time of optical scanning. Basic agreement across each isolated mode family does provide confidence that the as-manufactured models are capable of representing full experimental setups.

The non-isolated blade responses for TWE, the compressor rig, and the full rotor GMM models were analyzed using FMM ID to determine that the frequency mistuning pattern for each mode fell between -1.5% to +2.0%. The general mistuning trend across each mode of the actual compressor rig was successfully predicted using both TWE and as-manufactured models. Excellent agreement exists between TWE and the as-manufactured FEMs for the 1^{st} and 2^{nd} bending modes with slightly less correlation for 1^{st} torsion. There exists an acceptable agreement in the mistuning prediction between TWE and RIG, but it is shown TWE is missing some of the physics associated with the rotor in a relevant aerodynamic environment. Lastly, it is found a basic mistuning agreement exists between the full as-manufactured GMM models and the compressor rig, but further refinement is needed in the approaches to separate modes with large damping for input into ROMs. However, there exists an overall mistuning prediction agreement between TWE, the compressor rig, and the as-manufactured models.

The predicted frequency deviations and tuned modes were used to predict the mistuned response amplification with additional inputs of engine order excitation and damp-

ing. Predicted mistuning amplifications for this rotor is less than 1.5 with the exception of one method for a single mode. This is a relatively low amplification, which makes it more difficult to predict using current methods. There exists some agreement between the maximum mistuned response amplification across all methods (TWE, RIG, and GMM) even with a relatively low level of mistuning present in this rotor. Moreover, the predicted mistuning amplification for the as-manufactured model simulating the compressor rig(GMM RIG) with representative rig damping is within 5% of the predicted mistuning amplification of the compressor rig for each mode. The corresponding blade at which the maximum amplification occurred did not necessarily translate across each method, but the maximum responders between the compressor rig and GMM RIG (RIG Q) were only off by a single blade for the 2^{nd} bend and 1^{st} torsion modes. Further investigations are needed to couple each system more accurately to predict rig/engine mistuning amplification responses.

The work herein comparing as-manufactured models to experiments ultimately shows the importance and the ability to use as-manufactured models to help increase detailed understanding of aerospace systems and the ability to have increased confidence in these models to determine how rotors will potentially respond during bench, rig, and engine tests. It also illustrates the ability to use as-manufactured models to predict both the mistuning pattern and the mistuning amplification across a broad series of modes.

Strain Gage Ramifications on Mistuning in As-Manufactured Models and Experimental Testing

Blade mounted strain gages are vital during rig and engine development to ensure safe engine operation. However, they also create a change in dynamics of integrally bladed rotors (IBR). State-of-the-art IBR dynamic response predictions are accomplished using as-manufactured models (AMM) generated via optical topography measurements and mesh morphing. Two AMM finite element models (FEMs) are created of a 20 bladed IBR. One FEM has no strain gages present, and the second FEM includes strain gages on six blades. Traditionally, strain gages and lead wires are treated as the same material property as the IBR itself. It will be shown that the inclusion of strain gages in AMMs using this method changes the IBRs predicted mistuning. An alternative AMM approach is developed that changes the material properties of the finite elements attributed to the strain gages. The predicted mistuning for each AMM is accomplished using the Fundamental Mistuning Model Identification (FMM ID), where the predicted mistuning will be compared to both Traveling Wave Excitation (TWE) experiments and a rotating, single stage compressor rig. Findings show mistuning predictions of the non-strain gaged AMM compare far better to the experiments when compared to the inclusion of the strain gages in the AMM. Additionally,

altering material properties of the strain gages in the AMM improves mistuning prediction compared to treating the strain gages as the parent IBR material. Therefore, AMM should be acquired using clean, non-strain gaged rotors or the material properties of strain gaged elements need to be altered to more accurately model the component.

6.1 Introduction

The digital thread/digital twin paradigm has been a widely covered topic throughout the turbine engine community for the past decade. Industry and government alike are exploring ways to use these digital networks to make products faster, cheaper, and easier to maintain [95]. The digital nature of these models will help to make better informed decisions throughout an engine's life cycle. One aspect of these digital twins are digital models of the individual components. These components consist of fans, compressors, turbines, support frames, etc. and each component is a vital part to continue successful operation of a turbine engine. The research conducted in this work uses a digital twin or as-manufactured model (AMM) of a turbine engine fan.

As-manufactured modeling has been a growing field at the component level for the last several years. These as-manufactured models are physics-based models used to predict responses based on optically-scanned geometry [9, 10], which aligns with visions for aircraft and engine digital twins by the Air Force Research Laboratory (AFRL) and NASA [92]. As-manufactured models can be used to generate physics-based results directly from a finite element model. They can be created throughout a component's life to help track the health of components that have been in service undergoing degradation from engine wear. Developing high fidelity as-manufactured models throughout a rotor's life has the potential to screen the component during service inspections to detect potential issues such as mistuning to avoid catastrophic failures due to HCF issues [2, 7, 78, 79]. Further, it has been shown that accounting for the geometric blade-to-blade variation via as-manufactured

FEMs illustrates a large variation in sensor response and placement of safety instrumentation, i.e., strain gages and tip timing probes [11, 12]. As-manufactured models have the potential to be used for higher fidelity sensor placement, more accurate computationally fluid dynamic (CFD) simulations for turbines and compressors [13, 14], and more accurate mistuning predictions [96], allowing for better informed engineering decisions throughout a component's life.

Confidence in as-manufactured modeling approaches using the finite element method has continued to grow as more comparative studies have been introduced in literature showing the positive (or negative) correlation that these analytical methods have compared to real world engine and rig operation. There exist published works comparing reduced order models (ROMs) to traveling wave excitation (TWE) experiments, spin pits, and compressor rigs that show the ability to use ROMs to identify mistuning [31, 34, 55, 62, 72–76]. Additionally, there has been comparative studies between low-fidelity as-manufactured models to modal ping testing that showed varying success when comparing mistuning patterns [13, 46, 48, 50, 51]. There have been few comparison studies using high-fidelity as-manufactured models developed via mesh morphing. Maywald, et al. [10] utilized an as-manufactured model via mesh morphing to predict the mistuning pattern of an IBR and successfully compared the results to modal ping testing. Kaszynski, et al. [54] showed that as-manufactured models are capable of predicting a mistuned response by comparing to TWE experiments. Gillaugh, et al. [96] demonstrated successful sector mistuning predictions to modal ping testing, TWE experiments, and a compressor rig. However, the as-manufactured models developed by Gillaugh et al. had strain gages mounted to the rotor that were treated with the same material properties as the parent rotor itself that potentially caused poor mistuning comparisons for one of the analyzed modes [96].

Strain gages have been the foundation for real time health monitoring of rig and engine testing in the turbine engine community for decades, but they also have the ability to cause potential ramifications when developing as-manufactured models. Traditional blade

mounted strain gages consist of foil strain gages embedded in an epoxy resin for lower temperatures or embedded in a ceramic cement for higher temperature applications. Traditional approaches for dealing with strain gages in as-manufactured models treat the strain gages and their associated lead wires and bonding agent as the exact same material as the rotor itself, i.e., a titanium rotor would be modeled with titanium strain gages. This clearly causes an impact on the stiffness and mass of the IBR, thus, affecting the mistuning predicted using the AMM. This impact is discussed in [96], where the authors' showed poor mistuning comparisons between AMM and experiments for a mode that was strongly influenced by the placement of the strain gages on the rotor. This artifact seems very evident, but little research has been done to examine the ramifications associated with this.

This chapter is focused on achieving two goals. The first goal is to demonstrate the negative impact modeling strain gages using the same material properties as the rotor itself has on mistuning predictions when developing as-manufactured models. The second goal is to develop an approach to more effectively model strain gages on an IBR by changing the material properties of the finite elements associated with the strain gages and epoxy resin. Lastly, an investigation is conducted to determine if the application of strain gages onto a rotor effect mistuning by using traveling wave excitation experiments pre/post strain gage application to analyze the rotor's mistuning.

6.2 Rotor Description

A production like IBR designated PBS (parametric blade study) R4 [90] is used to investigate the strain gage ramifications on a turbine engine fan component. The rotor consists of 20 low-aspect ratio blades with a rough diameter of 17 inches. It has been heavily tested and studied both aeromechanically and aerodynamically in the Air Force Research Laboratory's (AFRL) Compressor Aero Research Laboratory (CARL) and the Turbine Engine Fatigue Facility (TEFF). The rotor is subject to aerodynamic drivers from various inlet dis-

tortion screens, 31 downstream stators, and 4 downstream struts. The culmination of these drivers excite three modes during operation: 1^{st} bend, 2^{nd} bend, and 1^{st} torsion [96]. To monitor the aeromechanic behavior of these modes and to ensure safe test operation, strain gages are present on six blades (Blades 1, 3, 4, 11, 13, and 14) for a total of 13 strain gages on the rotor. The strain gage and its associated lead wires are bonded in a soft epoxy resin, denoted by the yellow strip on Blade 13 in Fig. 6.1. Additionally, the rotor is equipped with blade tip timing (BTT) on the leading and trailing edge tips of the rotor to record raw tip deflection of the rotor during operation. The non-intrusive nature of the BTT probes do not effect the dynamic response of rotors. However, the application of strain gages to rotors have the potential to change the dynamics of rotors both experimentally and analytically as in as-manufactured models. To investigate these potential strain gage ramifications a mixture of experimental and analytical methods will be used to evaluate the mistuning of this rotor.

6.3 Experimental & Analytical Mistuning Methods

Analyzing the mistuning of rotors requires frequency response functions (FRF) for each individual blade. The FRFs for this rotor were collected using four methods: modal ping testing, traveling wave excitation, a rotating compressor rig, and using various as-manufactured FEM forced response analysis results. The mistuned modes and system frequencies of the FRFs for a particular mode family are inputs into a commonly referenced reduced-order model (ROM) called the Fundamental Mistuning Model Identification (FMM ID) developed by Feiner & Griffin [31–33] that creates an analytical model from the experimental results to evaluate a system's mistuning. The underlying assumptions associated with FMM ID require an isolated mode family where the majority of strain energy lies in the rotor blade (not the disk). The vibratory modes discussed in the work herein are well isolated modes, making them all valid candidates for FMM ID [96].

Figure 6.1: PBS R4 Applied Strain Gage

6.3.1 Modal Ping Testing

Modal ping testing is a common method to determine the natural frequencies of components. It can be accomplished using a modal impact hammer or shaker, where the frequency response can be collected using various methods such as accelerometers or laser vibrometers [56, 57]. The drawback with modal ping testing and IBR's is individual blades need to be "de-coupled" from the system to determine an individual blade's natural frequency. Research in the past detuned the system by using additional masses [10], where the current study uses a series of damping pads between each blade to isolate a single blade. Each isolated blade is excited using an electromagnet, and the vibration response is measured using a scanning laser vibrometer to obtain each blade's natural frequencies.

As-manufactured models of each bladed-disk sector were then generated and the cyclic boundaries on each sector were constrained to analytically determine each isolated blade's natural frequencies..The blade-to-blade frequency deviation is then calculated to allow for a direct comparison to the experimental modal testing approach. Details of this setup and process can be found in Gillaugh, et al. [96]. Modal ping testing develops adequate mistuning predictions, but results could sometimes be contaminated since it is never truly possible to completely isolate a single blade from an IBR. Therefore, traveling wave excitation experiments provide a means where the system de-coupling is not needed.

6.3.2 Traveling Wave Excitation

Traveling wave excitation is a form of experimental testing that simulates an engine order environment. Traveling wave systems have been utilized by both industry and academia to research the mistuning phenomena inherent in turbine engine IBRs [6, 60–62], where additional research investigated IBR vibrational analysis via contact and contactless excitation methods [63, 64]. The experimental configuration for this work consists of a stationary IBR, mounting fixture, electromagnet actuators, and components to control the phasing and excitation levels of each electromagnet, where a single electromagnet is positioned under each blade as seen in Fig. 5.3. The rotor being analyzed in this research is non-magnetic, therefore, small steel disks (t = 0.015", d = 0.16") with negligible mass are attached to the tip of each airfoil on the pressure side within 0.010" of the excitation source, where any remaining variation is calibrated out. Internal investigations have compared TWE using both acoustic and magnetic excitation and found almost no changes ($<$0.1%) in the extracted blade alone natural frequencies. However, it was found that the natural frequencies of a mode family would shift downward on the order of $0-5\%$ for modes with high mode participation where the steel disks were mounted. This was further verified using as-manufactured models that included the mass of each steel disk at the tip of each airfoil. This research is primarily concerned with the blade-to-blade frequency variation within a

mode family, not between them.

During traveling wave excitation of the IBR, the response of each airfoil leading edge tip is measured with a scanning laser vibrometer. Traveling wave tests were conducted over a range of engine orders and the responses were recorded. Fig. 6.2 shows the normalized individual blade responses, where the high, medium, and low responding blades are highlighted with the remaining blade responses in gray scale. The responses recorded during TWE testing have minimal damping and, thus, the responses have well separated modes. This enables an ease of input into FMM ID for mistuning prediction, allowing for a robust means of screening IBRs for mistuning using TWE.

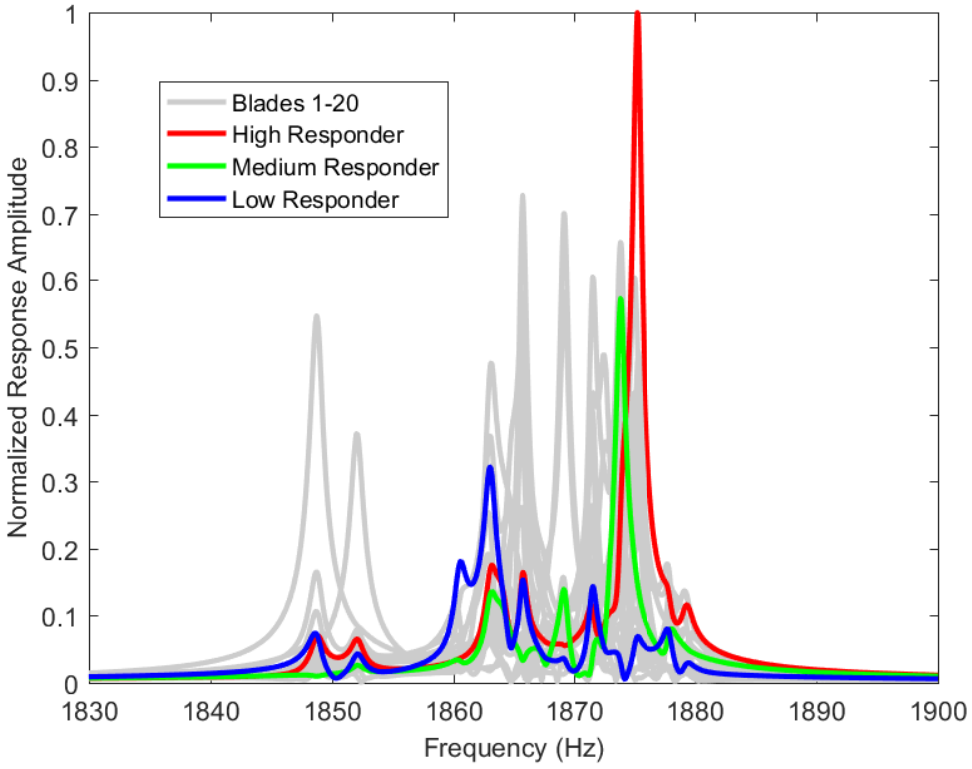

Figure 6.2: 1^{st} Torsion EO7 TWE Response

6.3.3 Rotating Compressor Rig

Rotating compressor rigs offer the ability to represent the actual environment of IBRs. PBS R4 is installed in the CARL facility that tests axial flow compressors with speed capability up to 21,000 rpm. The IBR is heavily instrumented including blade mounted strain gages and a non-contact measurement system (NSMS) that consists of 24 optical spot probes (12 leading edge/12 trailing edge). To capture quality modal response data during testing, slow sweep rates (25 rpm/sec) were used to traverse each mode of interest, where multiple sweeps were performed for each mode to assess measurement variance [93, 96]. An example of blade responses for the 1^{st} torsion mode with an EO7 response can be seen in Fig. 6.3. The response data is evaluated for mistuning using FMM ID. However, unlike the TWE data, a large amount of damping is present in the system (100x more than TWE) due to the addition of the aerodynamic damping component. This large amount of damping makes it more difficult to distinguish between system modes for each mode family, and this was taken into account using a method involving nodal decomposition[75].

6.3.4 As-Manufactured Modeling

Traditional As-Manufactured Modeling Approach

Finite element models (FEM) of IBRs allow the simulation of experiments such as TWE and compressor tests, where as-manufactured FEMs allow the representation of the actual geometry of the rotor to a high fidelity. These as-manufactured FEMs can be developed using optical topography measurements and mesh morphing. An optical scan of PBS R4 was conducted using a structured light approach with the capability of producing point clouds with an accuracy of ± 0.0003 inches [9, 47]. This research captured optical scans of the PBS rotor in two different states: clean rotor without any strain gages and the strain gaged rotor. A notional tuned finite element model was reverse engineered from the optical

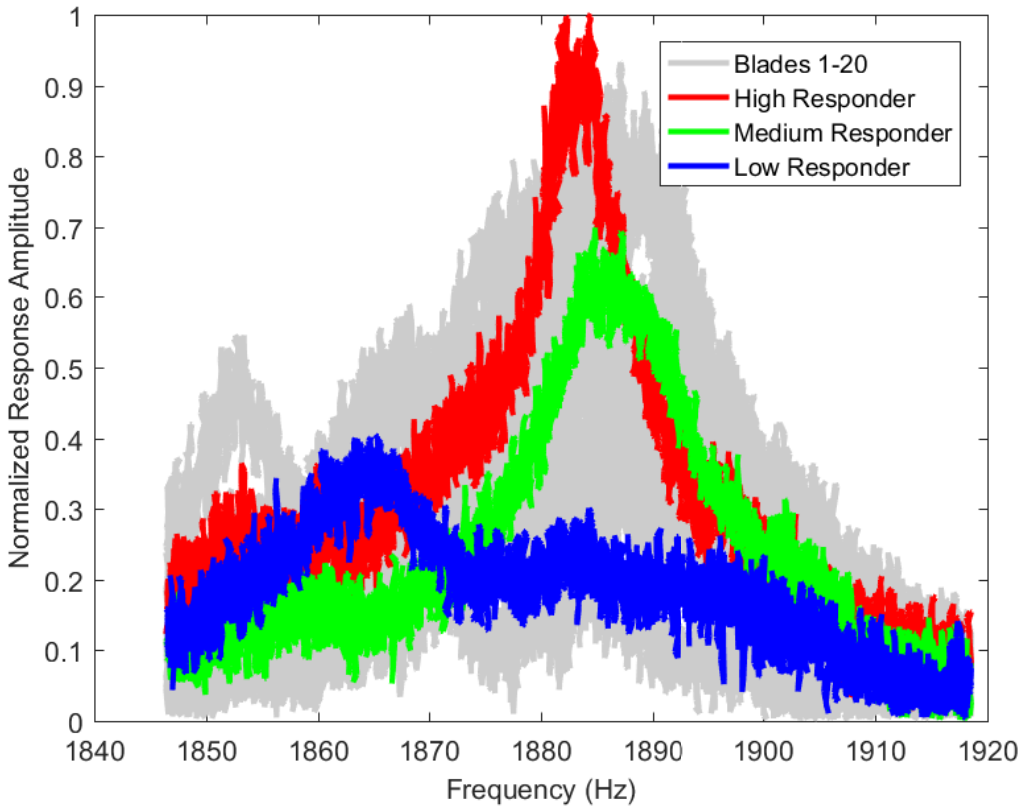

Figure 6.3: 1^{st} Torsion EO7 Rig NSMS Response

scan of the IBR. This tuned FEM will be used later in the mesh morphing process. The tuned FEM is then aligned to each point cloud representing the actual geometry of the IBR. A mesh morphing process is then used to update the notional tuned FEM nodes to match the tessellated surface data of the point cloud. The details of this process can be found in the works of Kaszynski et al. [9]. Fig. 6.4 shows the mesh morphing process on the leading edge tip of PBS R4, displaying the aligned tuned FEM model to the tessellated surface data of the point cloud (white surface mesh). There is clearly a discrepancy between the as-manufactured IBR (white surface mesh) and the tuned FEM with deviations between the two ranging from $\pm$ 0.010 inches. Upon completion of the mesh morphing process, an as-manufactured IBR is developed that is within $\pm$0.0003 inches of the tessellated point cloud. The AMM of PBS R4 consists of 2,279,707 nodes and 504,480 elements composed of 95%

hexahedral elements with a tetrahedral/pyramidal interface between the blade platform and the remainder of the disk. A mesh refinement study was performed to ensure the mesh was sufficiently dense as to not impact the results.

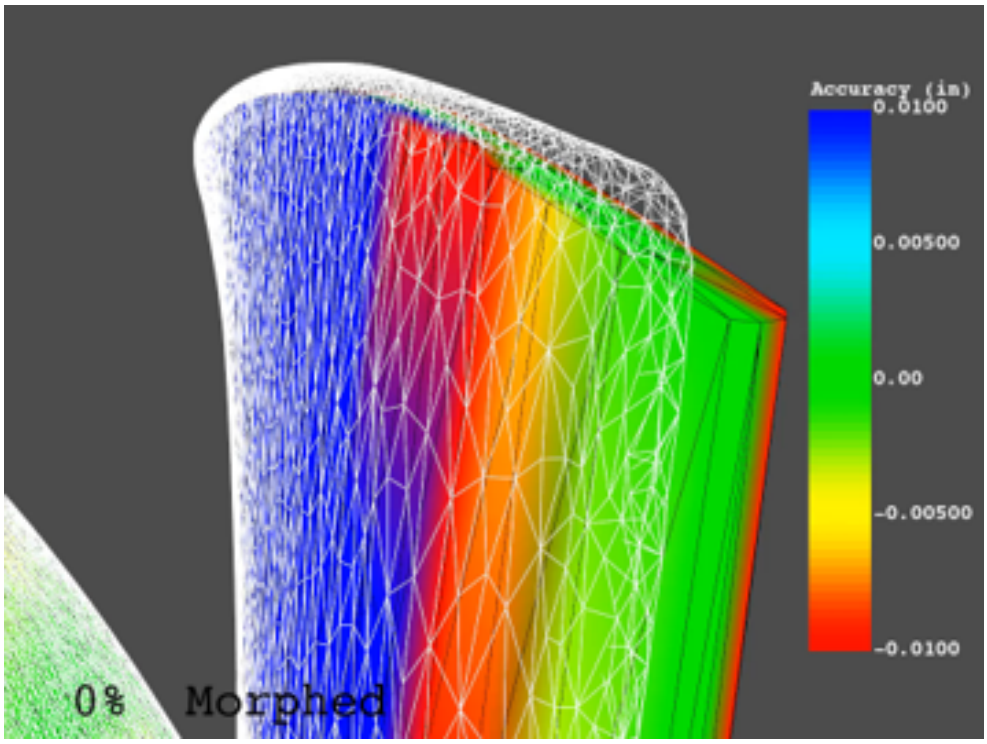

Figure 6.4: Mesh Morphing Process

Additionally, the mesh morphing process allows the capability to assess the accuracy between multiple IBR rotor scans or multiple FEM meshes. Fig. 6.5a shows PBS R4 with strain gages applied to the rotor on two blades, where Fig. 6.5b shows an accuracy plot comparing two scans of the PBS Rotor 4 with and without strain gages. The scans are nearly identical (as they should be) except for the location of the strain gages and associated lead wires and application material. This can be easily distinguished in Fig. 6.5b by denoting the red and yellow contours, showing a deviation between the scans greater than 0.015 inches in some areas. The geometry associated with these strain gages and instrumentation wires is embedded in the as-manufactured FEMs, and the material properties associated with this volume is traditionally treated as the same material as the rotor itself. Therefore,

artificial stiffening and mass loading could impact the mistuning. The forced response of the AMM rotor is simulated by applying modal superposition [96]. Multiple forced response analyses were conducted using the developed as-manufactured models. The first analysis simulated the TWE environment with a free-free boundary condition by fixing a single node on the back face of the rotor bore with a global damping matching the TWE environment(Fig. 6.6a). The second analysis simulates the rotating compressor rig with fixed constraints at the hub of the rotor with a rotational velocity matching the mode and EO driver of interest with a global damping matching the rig environment(Fig. 6.6b). No additional aerodynamic loadings were applied to the rig FEM analyses. The as-manufactured FEM responses (Fig. 6.6) for each blade are then evaluated for mistuning using FMM ID.

As-Manufactured Modeling Accounting for Strain Gages

The as-manufactured models previously discussed treat the strain gages, lead wires, and associated bonding agent as the same material properties as the rotor themselves. A more accurate approach when developing an as-manufactured model from optical scans with strain gages is to attempt to alter the finite elements associated with the strain gages to more accurately match the material properties of the resin and strain gages/lead wires. One approach to accomplish this is to manually select elements where the user "believes" the strain gages are present. However, this approach is error-prone and provides inaccurate predictions. A more accurate method to demonstrate an approach to model strain gages is to utilize existing scans of the IBR pre and post strain gage application. Utilizing the accuracy plot in Fig. 6.5b, the nodes/elements above a user specified threshold of deviation can be selected. This allows the material properties for those selected elements (that match the actual geometry of the strain gages to an extremely high fidelity) to be optimized to more closely represent the material properties of the strain gages and bonding resin. M-bond 610 is the bonding epoxy used to apply the strain gages to the titanium substrate,

(a) Strain Gaged Rotor

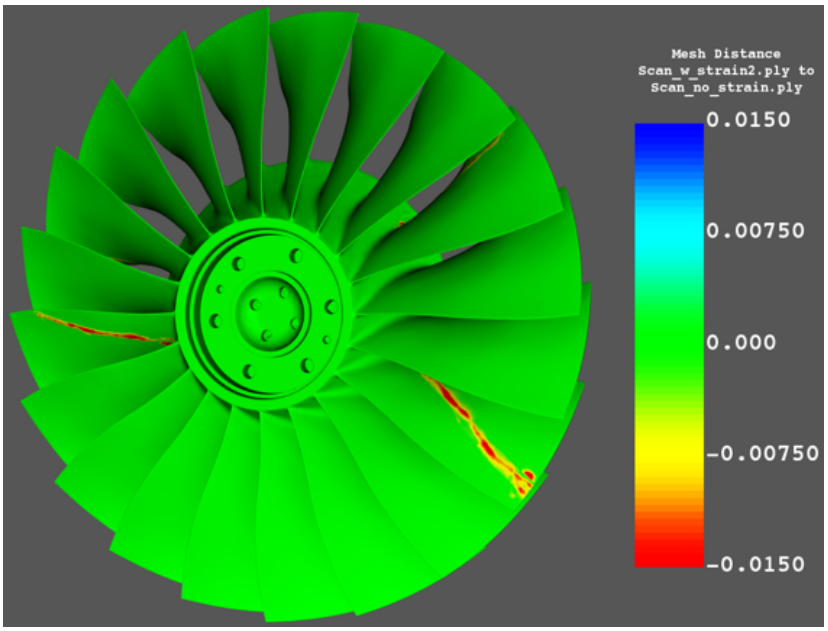

(b) Accuracy Plot Comparing Strain Gaged To Non-Strain Gaged Rotor

Figure 6.5: PBS R4 With Applied Strain Gages

where Fig. 6.7 displays a graphical depiction of the finite element mesh and the selected elements that encompass the strain gages. Fig. 6.7 depicts the mean cell distance that a cell

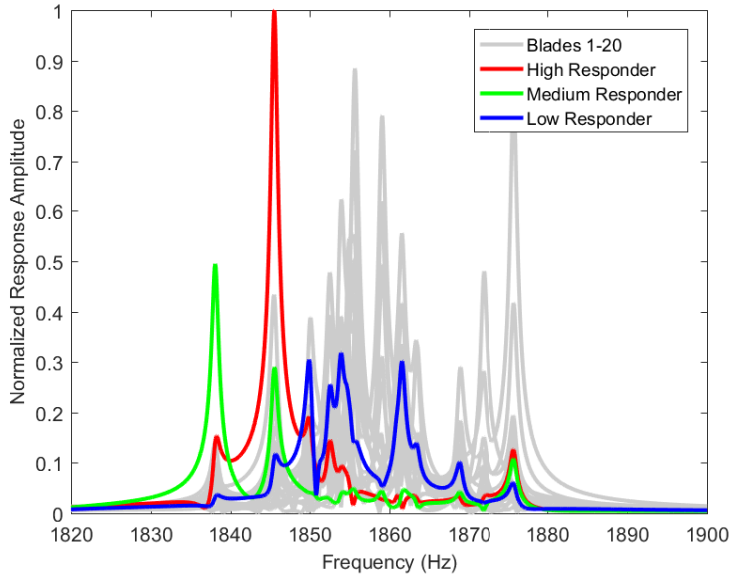

(a) Staionary TWE FEM with TWE Damping Ratio

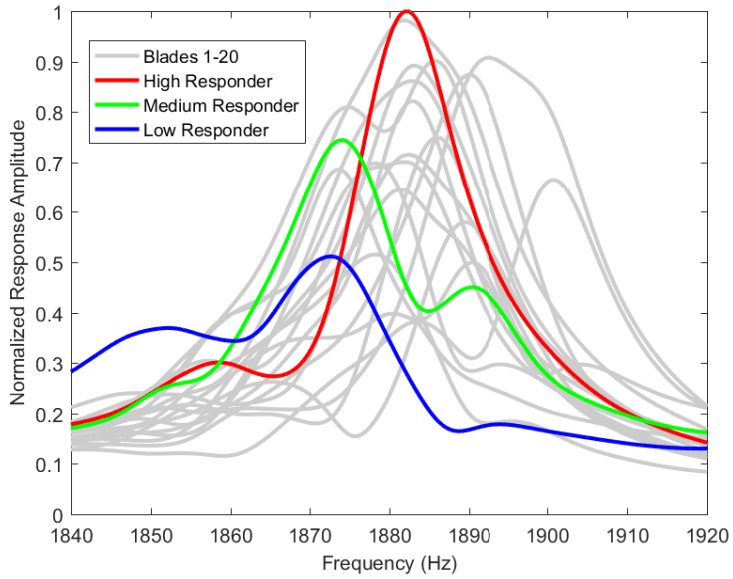

(b) Rotating Compressor Rig FEM with Rig Damping Ratio

Figure 6.6: 1^{st} Torsion EO7 As-Manufactured FEM Response

needed to be shifted when morphing the finite element mesh between the strain gaged and non-strain gaged optical scan. These elements above a specified threshold were made into components to import into a finite element solver where the material properties of these components were changed from the titanium properties to strain gage properties. A trend

study was developed to investigate and optimize the parameters to more accurately model the strain gage instrumentation in the as-manufactured model. Note that the selected elements associated with the strain gages are not solely the instrumentation/epoxy material associated with the strain gages and more likely are a combination of the strain gage and titanium material. These optimized material parameters will change depending on mesh density and element size. The parameters that were investigated were the density and modulus of the elements as well as the mean cell distance threshold (Fig. 6.7).

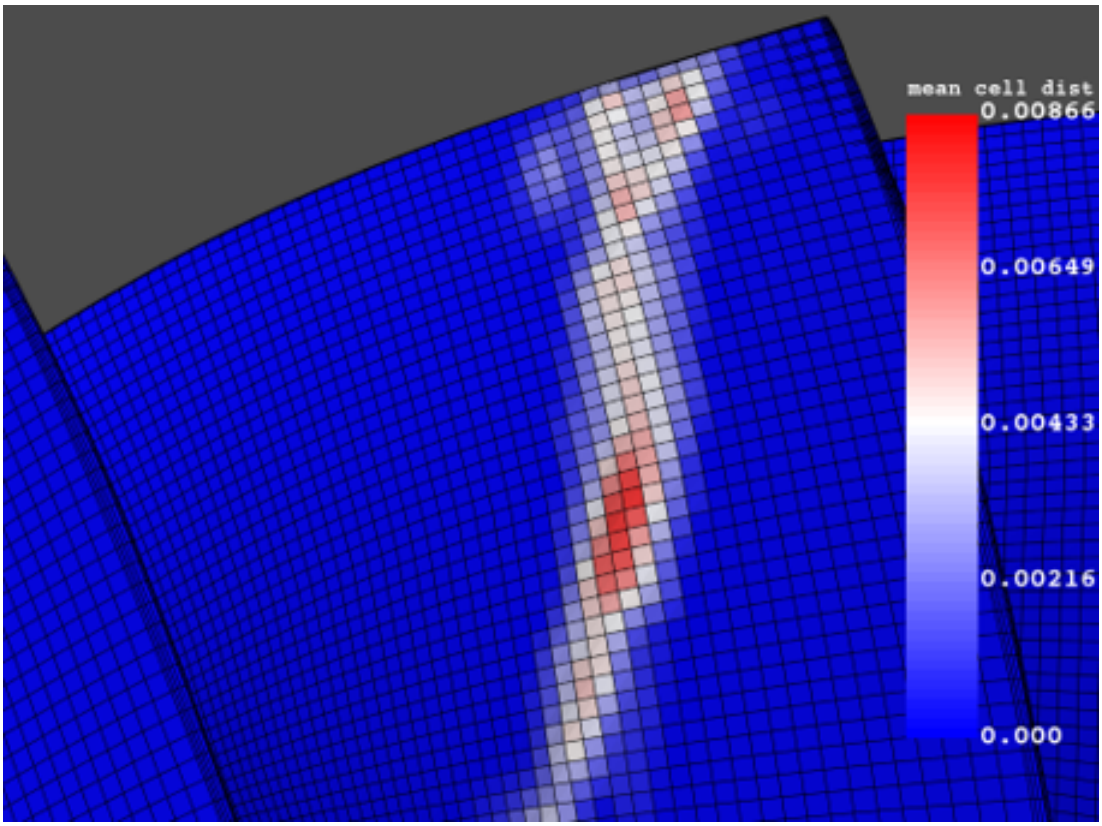

Figure 6.7: As-Manufactured Model with Contoured Elements Matching Strain Gage Material Properties

6.4 Results

6.4.1 Strain Gage Effects on As-Manufactured Models

Strain Gage Effects on Modal Ping Testing

Using the methods to isolate blades both experimentally and analytically using the AMM cyclic blade FEMs previously discussed, the frequency deviations are compared. Fig. 6.8 displays the frequency deviations for each mode and method as a function of blade number. The correlation coefficient, R, for each mode was calculated with respect to the isolated experimental (EXP) results.

The 1^{st} bend frequency deviations (Fig. 6.8a) show good agreement (R = 0.86) between the experimental isolated blades and the AMM isolated blade models that include the strain gages treated as the same material as the rotor. However, the correlation improves (R = 0.94) when the AMM with no strain gages is used. A similar trend occurs for 2^{nd} bend mode (Fig. 6.8b) where the correlation improves from $R = 0.91$ to $R = 0.94$. A significant better agreement exists for the 1^{st} torsion mode when removing the strain gages as seen in Fig. 6.8c. The numerical results are better illustrated in Table 6.1. The effect strain gages have on individual modes will vary from IBR to IBR. The instrumentation layout associated with this PBS rotor had a strong impact on the mistuning predictions for the torsional mode, meaning the instrumentation wires were adhered in such a way as to effect this mode more so than the bending modes. This is a general finding and other rotors could exhibit larger discrepancies in mistuning for different modes based on how the strain gages are laid out on that specific rotor.

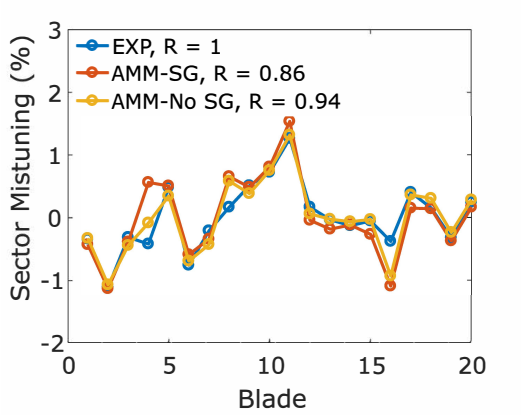

(a) 1^{st} Bend

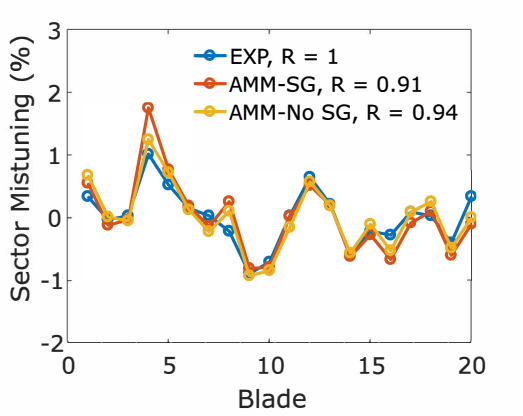

(b) 2^{nd} Bend

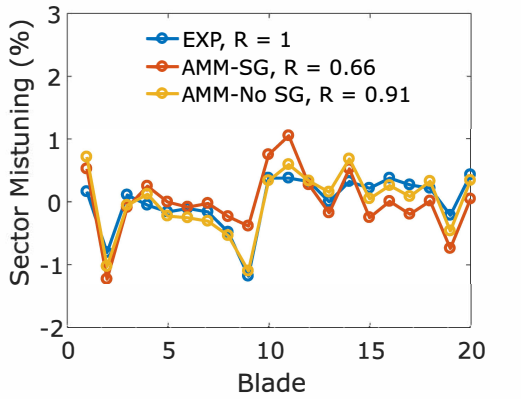

(c) 1^{st} Torsion

Figure 6.8: Modal Ping Testing Sector Mistuning

Strain Gage Effects on TWE

The previous section investigated the effect strain gages had on isolated blades only. However, to determine strain gage effects on the mistuning of the system, participation between individual blades/disk needs to be allowed. This section will analyze the effects modeled strain gages in as-manufactured models have on the mistuning calculated using TWE experiments. Fig. 6.9 displays the sector mistuning calculated via FMM ID using the TWE response data for three modes. Note the average error across each blade and mode for the TWE experiments is $\pm 0.13\%$. Fig. 6.9a and Fig. 6.9b both show an improved AMM correlation to TWE when using the AMM model with no strain gages. Fig. 6.9c shows minor improvement, but still excellent correlation, where Fig. 6.9d shows the largest improvement

Table 6.1: Modal Ping Testing Correlation Coefficients

Method Comparisons	Correlation Coefficient (R) 1B	2B	1T
GMM with Strain Gages	0.86	0.91	0.66
GMM without Strain Gages	0.94	0.94	0.91

in correlation. These results depict the same trend as the results in the isolated sector study, which showed that treating the modeled strain gages as the same material properties as the parent rotor has a larger effect on the torsional mode compared to the bending modes. Additionally, the 1^{st} bend mode is analyzed using two separate engine order excitations (EO3 and EO4), where the EO4 excited mode shows a better correlation than the EO3 mode. This is because the EO3 excited 1^{st} bend mode falls in a frequency range that excites a disk mode simultaneously. One of the assumptions with FMM ID is that the majority of the strain energy lies in the blades. Therefore, a disk mode contaminates the results associated with the EO3 mode causing a slightly worsened correlation. However, it is again shown that utilizing an as-manufactured model without strain gages has a better mistuning correlation than treating the strain gages as the same material as the parent rotor.

Table 6.2: TWE Correlation Coefficients

Method Comparisons	Correlation Coefficient (R) 1B (EO3)	1B (EO4)	2B (EO7)	1T (EO7)
GMM with Strain Gages	0.87	0.92	0.94	0.74
GMM without Strain Gages	0.90	0.96	0.95	0.84

Strain Gage Effects on Compressor Rig

This section analyzes the blade response data collected during a rotating rig compressor test and through various as-manufactured models and utilizes FMM ID to calculate the sector mistuning. Fig. 6.10 shows the IBR's sector mistuning with and without strain

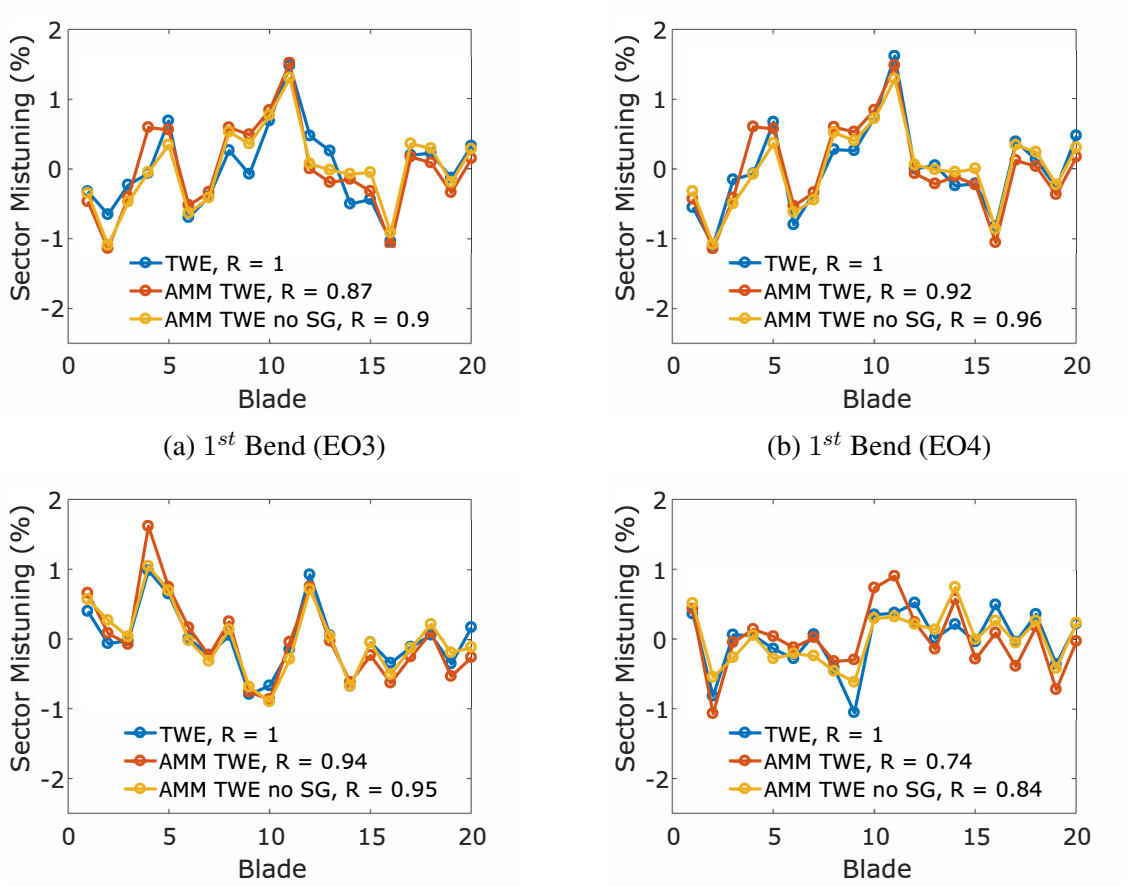

(a) 1^{st} Bend (EO3)

(b) 1^{st} Bend (EO4)

(c) 2^{nd} Bend (EO7)

(d) 1^{st} Torsion (EO7)

Figure 6.9: TWE Sector Mistuning

gages, which again shows an improved correlation when no strain gages are present on the as-manufactured model. Note the average error across each blade and mode for the compressor experiments is $\pm 0.05\%$. There exists worsened correlation for the 1^{st} bend mode with an EO3 excitation, which again can be accounted for due to the disk mode occurring at a similar speed as that which excites this mode. The disk mode is excited more during the rig testing compared to the TWE testing, causing the correlation between the as-manufactured models and the rig to be worse. However, the other modes all developed increased correlation when utilizing the as-manufactured models without strain gages present. This helps to solidify the basic fact that better mistuning correlation exists when using AMM models that do not have strain gages present on the blades (as expected). This

is a very evident finding, but some as-manufactured models may not have the luxury of optical scans before instrumentation is placed on the rotor. The findings presented in this work show the potential ramifications strain gages can have on mistuning predictions when treated as the same material properties as the parent rotor, allowing researchers to gage the accuracy of the results.

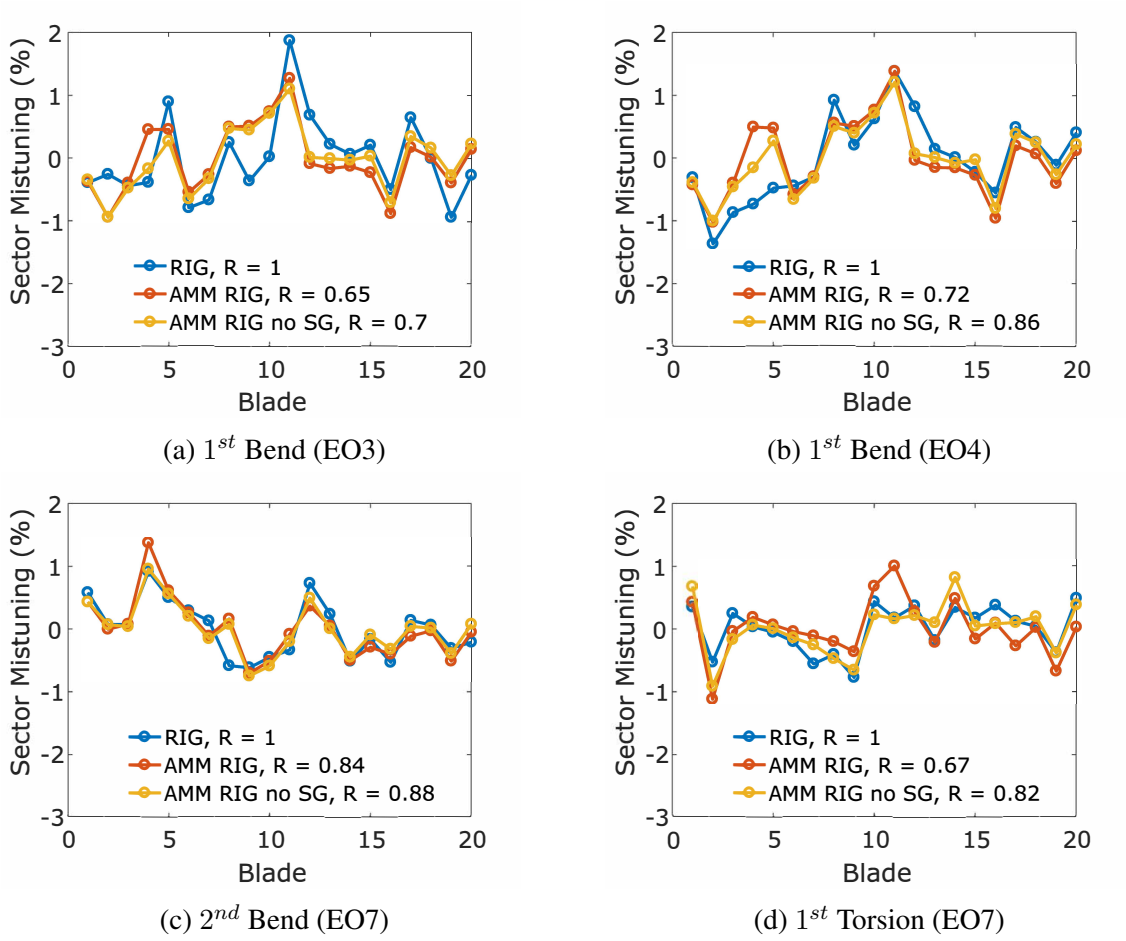

(a) 1^{st} Bend (EO3)

(b) 1^{st} Bend (EO4)

(c) 2^{nd} Bend (EO7)

(d) 1^{st} Torsion (EO7)

Figure 6.10: Compressor Rig Sector Mistuning

Strain Gage Effects on As-Manufactured Model, TWE, and Rig Comparisons

This section analyzes the blade response data from the previous sections consisting of as-manufactured model data, rotating compressor rig, and traveling wave excitation results.

Table 6.3: Compressor Rig Correlation Coefficients

Method Comparisons	Correlation Coefficient (R)			
	1B (EO3)	1B (EO4)	2B (EO7)	1T (EO7)
GMM with Strain Gages	0.65	0.72	0.84	0.67
GMM without Strain Gages	0.70	0.86	0.88	0.82

The goal of this section is to show the ability to use benchtop testing and as-manufactured modeling as functional methods to determine the mistuning of an IBR.

The sector mistuning calculated via FMM ID as a function of blade number for each mode can be seen in Fig. 6.11. The AMM simulations in these figures refer to the as-manufactured models that do not have strain gages present on the blades. Fig. 6.11 shows adequate correlation of predicted mistuning for both TWE and the GMM models. The correlation between each AMM simulation and the rig are nearly identical for each mode of interest, which provides confidence in the method developed to extract frequency and mode shape information for heavily damped systems. The 1^{st} bend mode with an EO 3 excitation shown in Fig. 6.11a shows a weaker correlation to the rig compared to the other modes due to the shaft bending mode in the operating range. Results show that both TWE and the as-manufactured simulations perform an adequate job of mistuning prediction, where the AMM models even perform substantially better for the 1^{st} bend EO4 mode. Therefore, both benchtop experiments and as-manufactured models provide accurate means of determining an IBRs mistuning as experienced during real world operation.

Table 6.4: GMM, TWE, & Rig Correlation Coefficients

Method Comparisons	Correlation Coefficient (R)			
	1B (EO3)	1B (EO4)	2B (EO7)	1T (EO7)
TWE	0.77	0.76	0.86	0.84
GMM TWE	0.70	0.85	0.85	0.81
GMM RIG	0.70	0.86	0.88	0.82

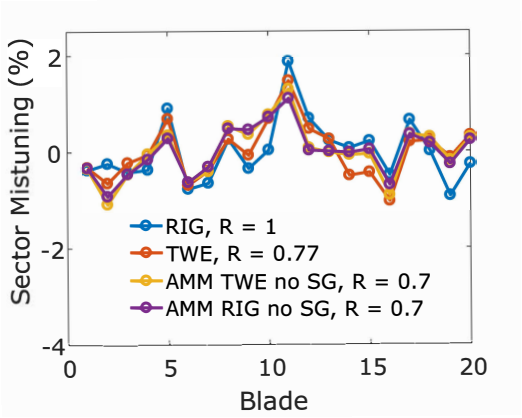

(a) 1^{st} Bend (EO3)

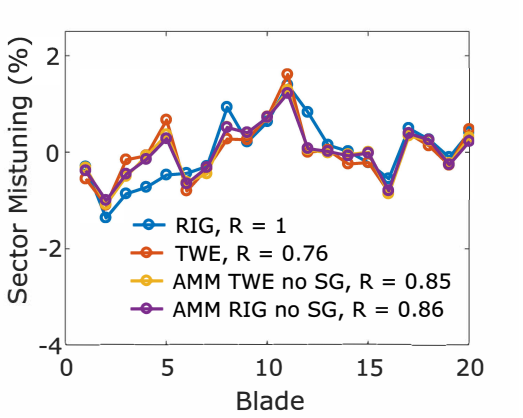

(b) 1^{st} Bend (EO4)

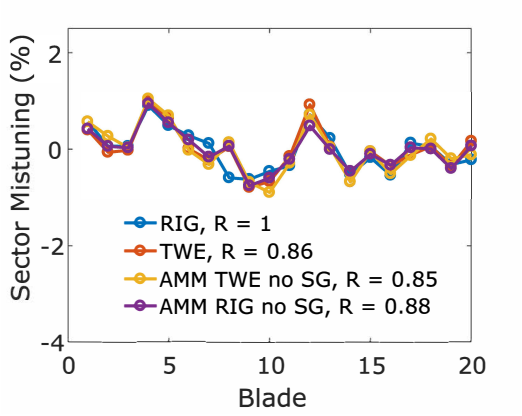

(c) 2^{nd} Bend (EO7)

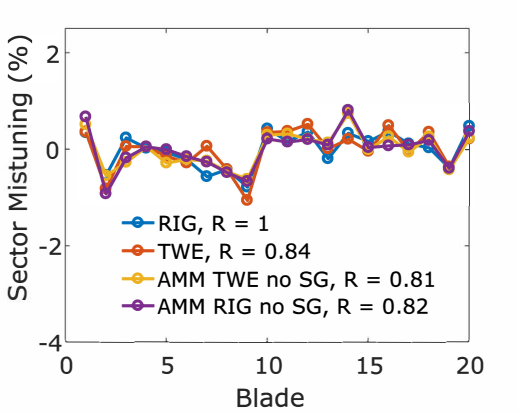

(d) 1^{st} Torsion (EO7)

Figure 6.11: GMM, TWE, & Rig Sector Mistuning

6.4.2 Strain Gage Modeling in As-Manufactured Models

It has now been shown that accounting for instrumentation on IBRs when developing as-manufactured models is important. This section utilizes the process developed in Section 3.4.2 to demonstrate an approach to account for strain gage instrumentation in an as-manufactured model. An initial baseline trend study was performed using a three factor/two level investigation where the density and modulus were varied between 30% and 90% of the original titanium properties and the element threshold was varied between 0.0025 inches and 0.005 inches. This equated to a total of eight as-manufactured models, where the results of these runs will be discussed by analyzing the 1^{st} torsion mode. This mode had the weakest correlation both with and without strain gages modeled using as-manufactured

modeling. The forced response data for this mode for each of the eight cases were processed with FMM ID to determine the IBR sector mistuning and correlated to the compressor rig sector mistuning. Results of the baseline investigation found little correlation between both R/density/element threshold and R/modulus/threshold. Therefore, element threshold using the chosen levels does not appear to have a strong effect on the modeling of strain gages and an element threshold of 0.0025 inches was chosen for the remaining modeling. A stronger correlation (R $>$ 0.90) was found between R/density/modulus. The baseline trend study portrayed that the density of the strain gaged elements should be reduced while maintaining a modulus representative of the parent rotor. This provides a possible conclusion that modeling the strain gage instrumentation with the same material properties as the parent material has a larger effect on the mistuning by inducing increased mass loading as opposed to stiffness.

Therefore, a revised study was performed (Fig. 6.12) that maintained the modulus of the parent material while varying the density of the elements associated with the strain gages from 5% to 100% of the initial parent material density. This culminated with 11 different as-manufactured model FRF's that were processed with FMM ID to determine sector mistuning, which was correlated to the sector mistuning measured in the compressor rig. Fig. 6.12 plots the calculated correlation coefficents for each of these AMM models as a function of percent density of the original titanium material. A 3^{rd} degree polynomial curve was fitted to this data and the 95% confidence bounds are shown. Three validation points were generated by creating AMM models with strain gaged element densities of 46%, 58%, and 63% density to verify the curve fit was adequate. Results show varying the density of the elements that are a mixture of strain gage and titanium material properties produces a maximum correlation of 0.82 for the 1^{st} torsion mode at 60% density, which is a substantial increase in correlation compared to treating the strain gages as pure titanium (Fig. 6.10d). This also matches the calculated correlation coefficient for the AMM model with no strain gages present, which shows the capability to meet or exceed the same correlation by varying

the material properties of selected elements matching the strain gage locations.

The as-manufactured models developed account only for the geometric deviations. The material properties of the blades are all assumed to be isotropic. Both the traveling wave experiments and the rotating compressor rig experiments account for both geometric irregularities as well as the material property variation in the rotor. Ideally, if the as-manufactured models were able to perfectly match the boundary conditions of the experiments and if material variation was null, then the sector mistuning between the models and experiments would be perfectly correlated. Of course, boundary conditions are not always identical, there is test error/noise, and material property variation that is not accounted for with these models. By comparing the sector mistuning between the as-manufactured models, TWE, and the compressor rig, the authors are able to approximate material mistuning, test error, boundary condition problems, etc.

A drawback of the proposed modeling strategy is that it necessitates an optical scan of the rotor both before and after strain gage application. Future work is needed to generate algorithms to select those finite elements associated with the strain gages without the need for the clean rotor optical scan. Further, although the maximum correlation was seen using $\approx 60\%$ material density properties for this rotor, this will still vary from rotor to rotor depending on mesh size and strain gage bonding size. However, it has been shown that the modeling of strain gaged elements can be accounted for using mesh morphing approaches to more accurately calculate sector mistuning.

6.4.3 Strain Gage Application Effects on Experiments

The mistuning of PBS R4 will now be discussed in a strictly experimental sense by using TWE experimental results of the rotor performed both before and after strain gages were applied to the rotor. A total of 13 strain gages were applied to the rotor across 6 blades, and those strain gages were bonded to the blades with a soft epoxy resin. The rotor consists

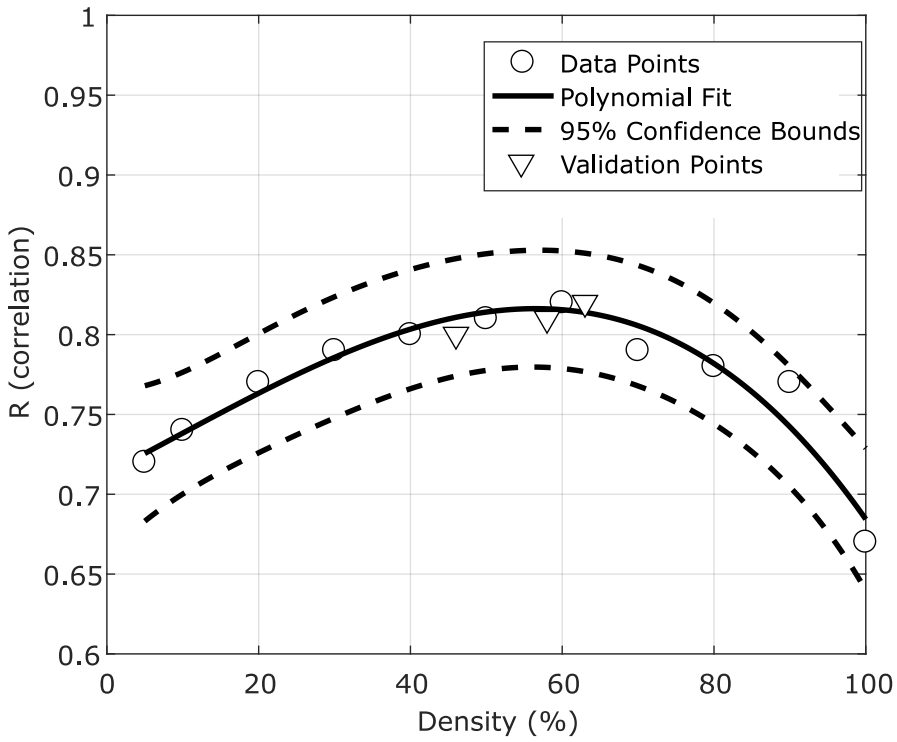

Figure 6.12: As-Manufactured Model with Strain Gage Modeling Trend Study

of 20 blades, hence, the EO drivers range from 0 EO to N/2 or 10 EO, where the nodal diameter map associated with PBS R4 can be found in Fig. 5.12. Based on the nodal diameter map, the engine order drivers that are studied in this work are EO1, which occurs in a small veering region for the 1^{st} torsion mode, and EO9, which occurs on a level region for each mode. To ensure measurement repeatability, four TWE experiments were done for each engine order for each strain-gaged/non-strain-gaged rotor. Three modes (1^{st} bend, 2^{nd} bend, 1^{st} torsion) were analyzed to explore the effect the strain gages have on the experimental mistuning prediction.

Fig. 6.13 shows the sector mistuning for PBS R4 with an EO1 excitation, where Fig. 6.14 shows the sector mistuning for PBS R4 with an EO9 excitation. The correlation coefficients for these figures are shown in Table 6.5. It is clear to see that the general mistuning trend for each mode is captured for each mode with excellent correlation for the

1^{st} and 2^{nd} bend modes with some variability and reduced correlation for the 1^{st} torsion modes for both engine order excitations. To further investigate these results a linear regression model was developed on the predicted sector mistuning between TWE with strain gages and TWE without strain gages (Fig. 6.15 and Fig. 6.16). The results show excellent correlation for both the 1^{st} bend and 2^{nd} bend modes with weaker correlation for the 1^{st} torsion modes. These results align with the as-manufactured modeling results that also showed weaker correlation for the 1^{st} torsion mode. This provides evidence that even soft epoxy mounted strain gages have the capability to effect IBR mistuning. The specific configuration of strain gages for this specific rotor does appear to effect the mistuning associated with the 1^{st} torsion mode. Therefore, strain gage instrumentation should be accounted for when analyzing rotors during engine development programs and research activities. Failure to account for the mistuning effect of strain gages during testing has the possibility to cause failures induced by strain gage application.

Table 6.5: Strain Gaged vs. Non-Strain Gaged IBR Experimental Correlation Coefficients

	Correlation Coefficient (R)		
Engine Order	1B	2B	1T
EO1	0.94	0.95	0.84
EO9	0.92	0.96	0.88

6.5 Conclusions

This chapter achieved three goals. The first goal demonstrated the negative impact treating strain gages as the parent rotor material has on mistuning predictions when developing as-manufactured models. This was accomplished by comparing two as-manufactured finite

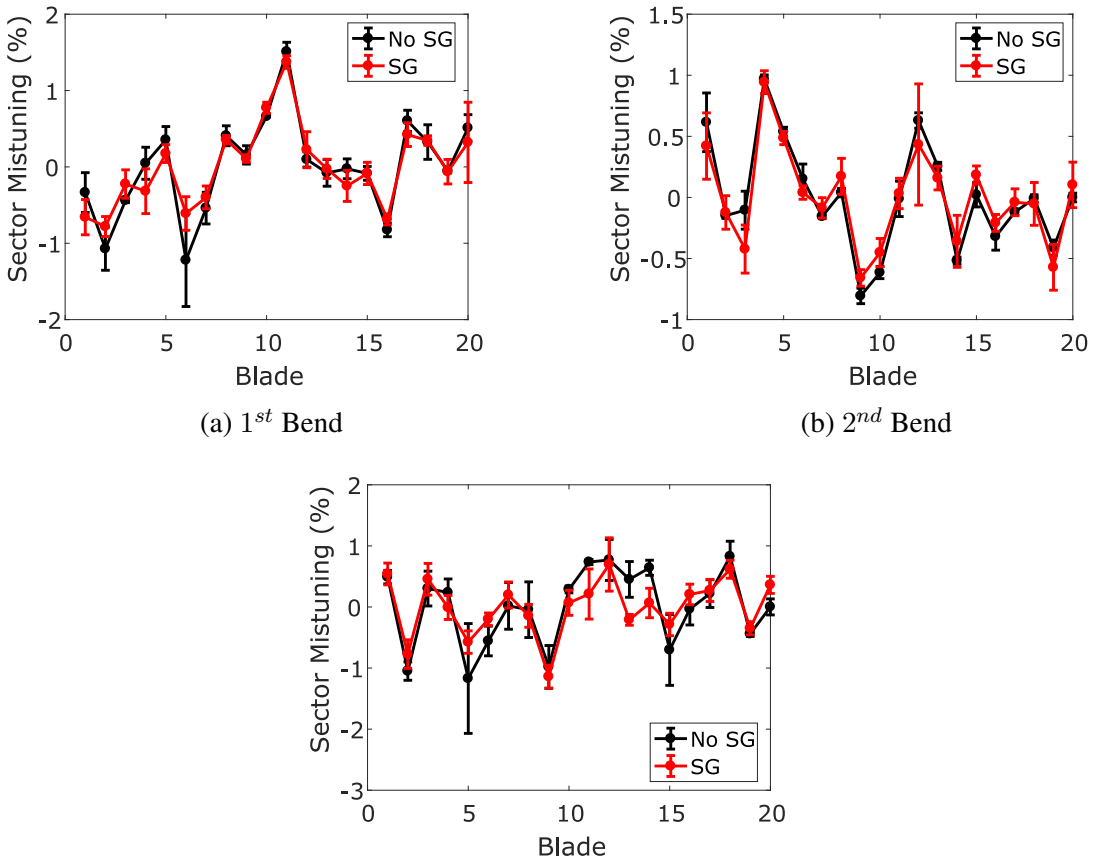

(a) 1^{st} Bend

(b) 2^{nd} Bend

(c) 1^{st} Torsion

Figure 6.13: PBS R4 EO1 Sector Mistuning

element models (one with strain gages and one without) to modal ping tests, to traveling wave excitation experiments, and to a rotating compressor rig experiment. Results show improved sector mistuning correlations when utilizing as-manufactured models without strain gages applied. Thus, if strain gages are present on an optical scan used to develop an as-manufactured model, then they need to be accounted for using modeling approaches as discussed in the second goal. The second goal developed an approach to more effectively model strain gages on an IBR by changing the material properties of the elements associated with the strain gages and epoxy resin. Improved sector mistuning correlation occurred by varying the density and modulus of elements associated with strain gage instrumentation where the strain gage elements were selected using mesh morphing algorithms. This

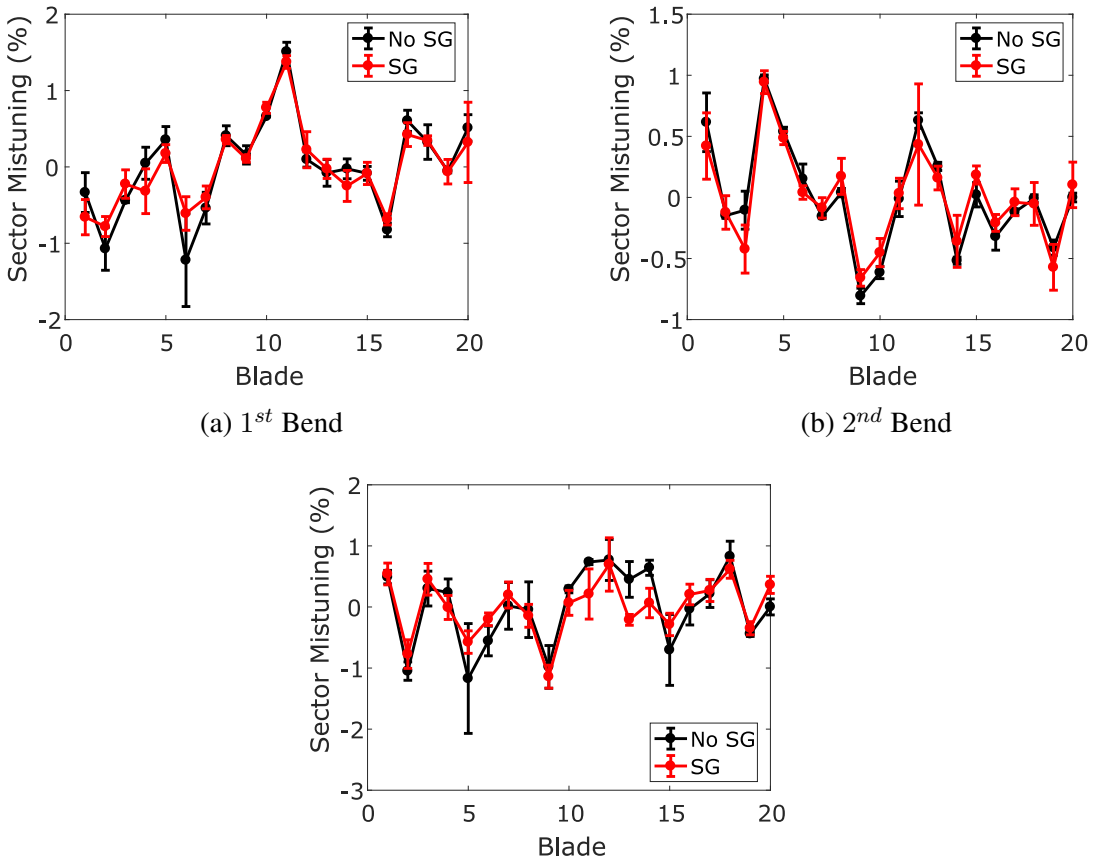

(a) 1^{st} Bend

(b) 2^{nd} Bend

(c) 1^{st} Torsion

Figure 6.14: PBS R4 EO9 Sector Mistuning

demonstrates the ability to account for strain gages in as-manufactured models to more accurately predict IBR mistuning. The last goal was to show the effect strain gages with a soft epoxy resin bonding agent applied to a fan stage had on the mistuning predictions of an IBR. This was accomplished by performing TWE tests on the same IBR pre and post strain gage application. The latter goal focused on strain gages effects experimentally rather than analytically. It is found that even soft epoxy mounted strain gages can effect rotor mistuning for specific modes. This effect will vary from rotor-to-rotor depending on the instrumentation layout, but should be accounted for during the engine developmental process. Accomplishing these three goals ultimately show the importance and the ability to use as-manufactured models to help increase detailed understanding of aerospace sys-

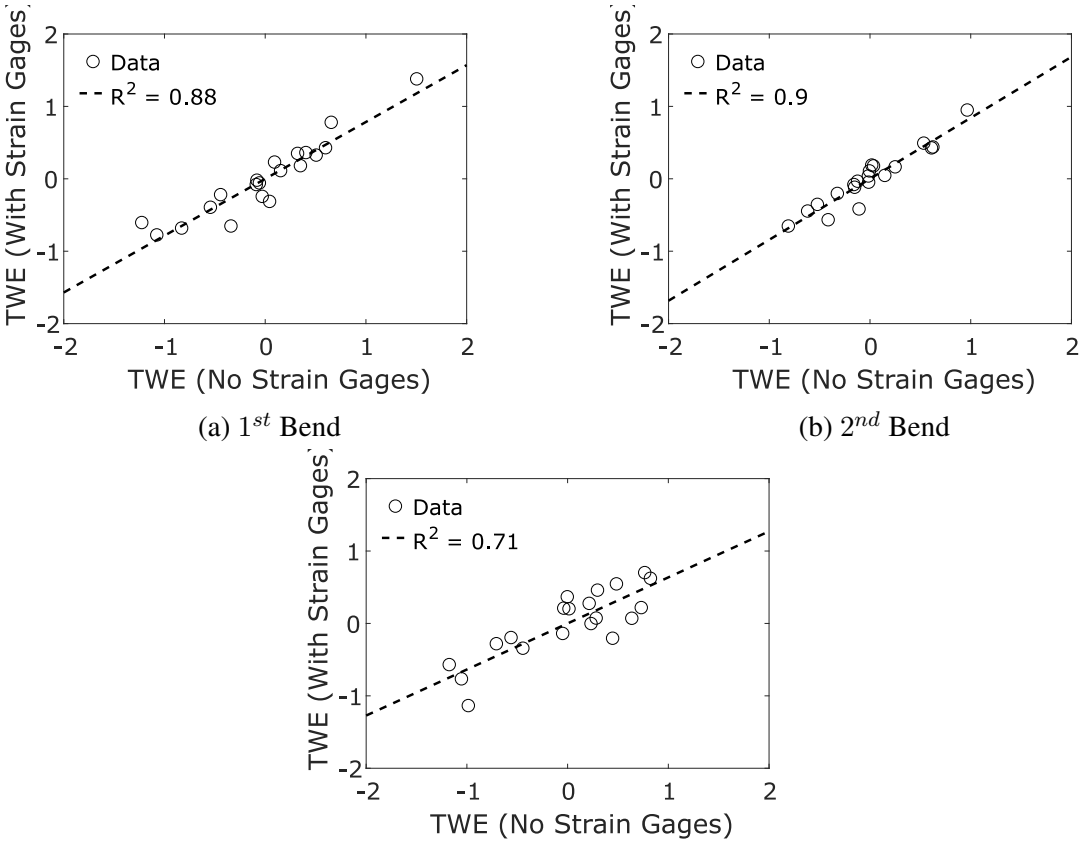

(a) 1^{st} Bend

(b) 2^{nd} Bend

(c) 1^{st} Torsion

Figure 6.15: EO1 TWE with Strain Gages vs. TWE without Strain Gages Predicted Sector Mistuning

tems and the ability to have increased confidence in these models to determine how rotors will potentially respond during bench, rig, and engine tests, further enhancing the digital twin/digital thread paradigm.

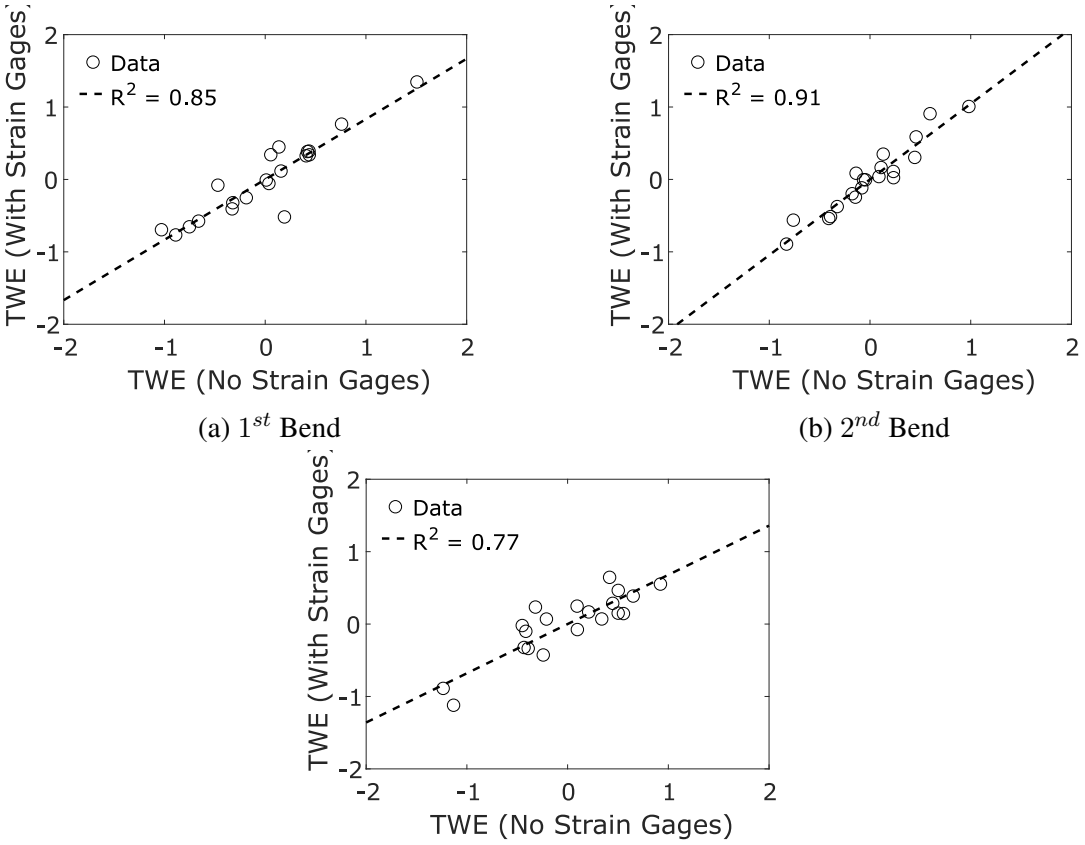

(a) 1^{st} Bend

(b) 2^{nd} Bend

(c) 1^{st} Torsion

Figure 6.16: EO9 TWE with Strain Gages vs. TWE without Strain Gages Predicted Sector Mistuning

Dissertation Closing

7.1 Conclusions

Traditional design approaches assume nominal, tuned geometries when analyzing IBR's for turbine engine designs. Failure to account for the actual geometry of components throughout their lifecycle can lead to costly failures and issues such as HCF. Optical scanning systems have enabled the development of as-manufactured modeling approaches that offer designers the ability to capture the actual geometry of components to an extremely high fidelity. The ease of as-manufactured modeling approaches allows the capability to track the health of components throughout their lifecycle, allowing a more detailed understanding of the component. However, the turbine engine community lacks comparison studies validating as-manufactured modeling approaches against experimental methods. The effort presented in this work completed a comprehensive mistuning comparison of a compressor using as-manufactured modeling, stationary benchtop experiments, and a rotating compressor facility. Results demonstrated the ability of as-manufactured models to successfully predict mistuning characteristics of a compressor by analyzing three different vibratory modes. Additional studies showed that not properly accounting for instrumentation in as-manufactured models can influence mistuning predictions. An approach was developed in this work to account for instrumentation in as-manufactured models by changing the material properties of the finite elements associated with the instrumentation material. The developed method improved mistuning correlation significantly compared to traditional

methods. One drawback of the developed method to account for strain gages is that an optical scan is needed of the rotor both pre/post strain gage application. Additionally, it was illustrated that as-manufactured models offer the ability to more accurately set strain gage limits and more accurately place strain gages on responsive blades. A detailed investigation was presented showing how strain gage limits can vary drastically due to mode shape variation between blades. An approach was developed to utilize as-manufactured models to optimally place strain gages on responsive blades. The culmination of this work increases confidence in as-manufactured modeling approaches and illustrates to the turbine engine community how powerful accounting for the actual geometry of components can be not only early in the design phase but also throughout the life of turbine engine components.

7.2 Future Work

The work presented in this effort did not include any aerodynamic effects on mistuning. Additionally, comparisons between the as-manufactured modeling methods and experimental approaches analyzed only mistuning sector deviations and mistuned amplification factors, neglecting actual predicted airfoil stresses. Further, the modes studied in this work were lower order vibratory modes. It would be of interest to study higher order modes as well. Future areas of work include:

- Aerodynamic effects on mistuning using as-manufactured models
- As-manufactured forced response predictions compared to BTT measurements
- As-manufactured forced response predictions compared to strain gage responses
- Higher-order mode mistuning predictions using as-manufactured modeling.

Bibliography

[1] Quora, "How Does a Turbine Engine Work," , 2018. URL https://www.quora.com/How-does-a-turbine-engine-work.

[2] Cowles, B. A., "High Cycle Fatigue in Aircraft Gas Turbines - An Industry Perspective," *International Journal of Fracture*, Vol. 80, 1996, pp. 147–163. doi: 10.1007/BF00012667.

[3] Sanders, A., Hassan, K., and Rabe, D., "Experimental and Numerical Study of Stall Flutter in a Transonic Low-Aspect Ratio Fan Blisk," *Journal of Turbomachinery*, Vol. 126, 2004, pp. 166–174. doi:10.1115/1.1645532.

[4] Silkowski, P., Rhie, C., Copeland, G., Eley, J., and Bleeg, J., "Computational Fluid-Dynamics Investigation of Aeromechanics," *Journal of Propulsion and Power*, Vol. 18, 2002, pp. 788–796. doi:10.2514/2.6001.

[5] Srivastava, R., Bakhle, M., Keith, T., and Stefko, G., "Flutter Analysis of a Transonic Fan," *ASME Turbo Expo*, Vol. 4, 2002. doi:10.1115/GT2002-30319.

[6] Castanier, M., and Pierre, C., "Modeling and Analysis of Mistuned Bladed Disk Vibration: Current Status and Emerging Directions," *Journal of Propulsion and Power*, Vol. 2, No. 22, 2006, pp. 384–396. doi:10.2514/1.16345.

[7] Hodges, C., "Confinement of Vibration by structural irregularity," *Journal of Sound and Vibration*, Vol. 82, 1982, pp. 411–424.

[8] Sinha, A., Hall, B., Cassenti, B., and Hilbert, G., "Vibratory Parameters of Blades from Coordinate Measurement Machine Data," *Journal of Turbomachinery*, Vol. 130, 2008, p. 011013. DOI: 10.1115/1.2749293.

[9] Kaszynski, A., Beck, J., and Brown, J., "Uncertainties of an Automated Optical 3D Geometry Measurement, Modeling, and Analysis Process for Mistuned Integrally Bladed Rotor Reverse Engineering," *Journal of Engineering for Gas Turbines and Power*, Vol. 135, No. 10, 2013, p. 102504. doi:10.1115/1.4025000.

[10] Maywald, T., Backhaus, T., Schrape, S., and Kuhhorn, A., "Geometric Model Update of Blisks and its Experimental Validation for a Wide Frequency Range," *ASME Turbo Expo 2017*, edited by ASME, 2017. DOI: 10.1115/GT2017-63446.

[11] Kaszynski, A., Beck, J., and Brown, J., "Experimental Validation of a Mesh Quality Optimized Morphed Geometric Mistuning Model," *ASME Turbo Expo*, Vol. 7A, 2015. doi:10.1115/GT2015-43150.

[12] Gillaugh, D., Kaszynski, A., Brown, J., Johnston, D., and Slater, J., "Accurate Strain Gage Limits Through Geometry Mistuning Modeling," *58th AIAA/ASME/ASCE/AHS/AS Structures, Structural Dynamics, and Materials Conference*, edited by AIAA, 2017. DOI: 10.2514/6.2017-0865.

[13] Schnell, R., Lengyel-Kampmann, T., and Nicke, E., "On the Impact of Geometric Variability on Fan Aerodynamic Performance, Unsteady Blade Row Interaction, and Its Mechanical Characteristics," *Journal of Turbomachinery*, Vol. 136, 2014, p. 091005(14 pages). doi:DOI:10.1115/1.4027218.

[14] Clark, J., Beck, J., Kaszynski, A., Still, A., and Ni, R., "The Effect of Manufacturing

Variations on Unsteady Interaction in a Transonic Turbine," *ASME Turbo Expo 2017: Turbomachinery Technical Conference and Exposition*, 2017.

[15] Slater, J., Minkiewicz, G., and Blair, A., "Forced Response of Bladed Disk Assemblies - A Survey," *34th AIAA/ASME/SAE,ASEE Joint Propulsion Conference and Exchibit*, 1998. doi:10.2514/6.1998-3743.

[16] Dye, R., and Henry, T., "Vibration Amplitudes of Compressor Blades Resulting from Scatter in Blade Natural Frequencies," *Journal of Engineering Power*, Vol. 91, 1969, pp. 182–187. doi:10.1115/1.3574726.

[17] Ewins, D., "The Effect of Detuning upon the Forced Vibrations of Bladed Disks," *Journal of Sound and Vibration*, Vol. 9, 1969, pp. 65–79. doi:10.1016/0022-460X(69)90264-8.

[18] Ewins, D., "A Study of Resonance Coincidence in Bladed Discs," *Journal of Mechanical Engineering Science*, Vol. 12, 1970, pp. 305–312. doi:10.1243/JMES_JOUR_1970_012_055_02.

[19] Ewins, D., "Vibration Characteristics of Bladed Disc Assemblies," *Journal of Mechanical Engineering Science*, Vol. 15, 1973, pp. 165–186. doi:10.1243/JMES_JOUR_1973_015_032_02.

[20] Ewins, D., "Vibration Modes of Mistuned Bladed Disks," *Journal of Engineering Power*, Vol. 98, 1976, pp. 349–355. doi:10.1115/1.3446180.

[21] Ottarsson, G., and Pierre, C., "On the Effects of Interblade Coupling on the Statistics of Maximum Forced Response Amplitudes in Mistuned Blade Disks," *Proceedings of the 36th AIAA/ASME/ASCE/AHS/ASC Structures, Structural Dynamics and Materials Conference*, Vol. 5, 1995. doi:10.2514/6.1995-1494.

[22] Griffin, J., and Hoosac, T., "Model Development and Statistical Investigation of Turbine Blade Mistuning," *Journal of Vibration, Acoustics, Stress and Reliability in Design*, Vol. 106, 1984, pp. 204–210. doi:10.1115/1.3269170.

[23] Hurty, W., "Dynamic Analysis of Structural Systems using Component Modes," *AIAA Journal*, Vol. 3, 1965, pp. 678–685. doi:10.2514/3.2947.

[24] Bampton, M., and Craig, R., "Coupling of Substructures of Dynamic Analyses," *AIAA Journal*, Vol. 6, 1968, pp. 1313–1319. doi:10.2514/3.4741.

[25] Dowell, E., "Free Vibrations of an Arbitrary Structure in Terms of Component Modes," *Journal of Applied Machinery*, Vol. 3, 1968, pp. 727–732. doi:10.1115/1.3422780.

[26] Castanier, M., Ottarsson, G., and Pierre, C., "A Reduced Order Modeling Technique for Mistuned Bladed Disks," *Journal of Vibration And Acoustics*, Vol. 119, 1997, pp. 439–447. doi:10.1115/1.2889743.

[27] Bladh, R., Castanier, M., and Pierre, C., "Component Mode-Based Reduced Order Modeling Techniques for Mistuned Bladed Disks - Part I: Theoretical Models," *Journal of Engineering for Gas Turbines and Power*, Vol. 123, 2000, pp. 89–99. doi:10.1115/1.1338947.

[28] Bladh, R., Castanier, M., and Pierre, C., "Component Mode-Based Reduced Order Modeling Techniques for Mistuned Bladed Disks - Part II: Application," *Journal of Engineering for Gas Turbines and Power*, Vol. 123, 2000, pp. 100–108. doi:10.1115/1.1338948.

[29] Yang, M., and Griffin, J., "A Normalized Modal Eigenvalue Approach for Rsolving Modal Interaction," *Journal of Engineering for Gas Turbines and Power*, Vol. 119, 1997, pp. 647–650. doi:10.1115/1.2817033.

[30] Yang, M., and Griffin, J., "A Reduced-Order Model of Mistuning Using a Subset of Nominal System Modes," *Journal of Engineering for Gas Turbines and Power*, Vol. 123, 2001, pp. 893–900. doi:10.1115/1.1385197.

[31] Feiner, D., and Griffin, J., "A Fundamental Model of Mistuning for a Single Family of Modes," *Journal of Turbomachinery*, Vol. 124, No. 4, 2002, pp. 597–605. doi: 10.1115/1.1508384.

[32] Feiner, D., and Griffin, J., "Mistuning Identification of Bladed Disks Using a Fundamental Mistuning Model - Part 1: Theory," *Journal of Turbomachinery*, Vol. 126, No. 1, 2004, pp. 150–158. doi:10.1115/1.1643913.

[33] Feiner, D., and Griffin, J., "Mistuning Identification of Bladed Disks Using a Fundamental Mistuning Model - Part 2: Application," *Journal of Turbomachinery*, Vol. 126, No. 1, 2004, pp. 159–165. doi:10.1115/1.1643914.

[34] Lim, S., Bladh, R., Castanier, M., and Pierre, C., "Compact, Generalized Component Mode Mistuning Representation for Modeling Bladed Disk Vibration," *AIAA Journal*, Vol. 45, No. 9, 2007, pp. 2285–2298. doi:10.2514/1.13172.

[35] Brown, J. M., "Reduced Order Model Development for Airfoil Forced Response," *International Journal of rotating machinery*, Vol. 2008, 2008. doi:10.1155/2008/ 387828.

[36] Beck, J., Brown, J., Slater, J., and Cross, C., "Probabilistic Mistuning Assessment using Nominal and Geometry Based Mistuning Methods," *Journal of Turbomachinery*, Vol. 135, 2013, p. 051004 (9 pages). DOI: 10.1115/1.4023103.

[37] Bhartiya, Y., and Sinha, A., "Accuracies of Reduced Order Models of a Bladed Rotor with Geometric Mistuning," *Journal of Turbomachinery*, Vol. 136, 2014. doi:10.1115/ 1.4025666.

[38] Sinha, A., "Reduced-Order Model of a Bladed Rotor with Geometric Mistuning," *ASME Journal of Turbomachinery*, Vol. 3, No. 131, 2009, p. 031007. doi:10.1115/1.2987237.

[39] Bhartiya, Y., and Sinha, A., "Reduced Order Model of a Multistage Bladed Rotor with Geometric Mistuning via Modal Analyses of Finite Element Sectors," *Journal of Turbomachinery*, Vol. 134, 2012. doi:10.1115/1.4003224.

[40] Bhartiya, Y., and Sinha, A., "Reduced Order Modeling of a Bladed Rotor wiht Geometric Mistuning via Estimated Deviations in Mass and Stiffness Matrices," *Journal of Engineering for Gas Turbines and Power*, Vol. 135, 2013. doi:10.1115/1.4007783.

[41] Madden, A., Epureanu, B. I., and Filippi, s., "Reduced-Order Modeling Approach for Blisks with Large Mass, Stiffness, and Geometric Mistuning," *AIAA Journal*, Vol. 2, No. 50, 2012, pp. 366–374. doi:10.2514/1.J051140.

[42] Baek, S., and Epureanu, B., "Reduced-Order Models of Blisks with Small Geometric Mistuning," *Journal of Vibration and Acoustics*, Vol. 139, 2017. doi:10.1115/1.4036105.

[43] Beck, J., Brown, J., Cross, C., and Slater, J., "Component-Mode Reduced Order Models for Geometric Mistuning of Integrally Bladed Rotors," *AIAA Journal*, Vol. 52, 2014. doi:10.2514/1.J052420.

[44] Beck, J., Brown, J., Runyon, B., and Scott-Emuakpor, O., "Probabilisitic Study of Integrally Bladed Rotor Blends using Geometric Mistuning Models," *58th AIAA/ASCE/AHS/ASC Structures, Structural Dynamics, and Materials conference*, edited by AIAA, 2017. DOI: 10.2514/6.2017-0860.

[45] Beck, J., Brown, J., Kaszynski, A., Cross, C., and Slater, J., "Geometric Mistuning Reduced Order Models for Integrally Bladed Rotors with Mistuned Disk-Blade Boundaries," *Journal of Turbomachinery*, Vol. 137, 2015. doi:10.1115/1.4029122.

[46] Schoenenborn, H., Grossmann, D., Satzger, W., and Zisik, H., "Determination of Blade-Alone Frequencies of a Blisk for Mistuning Analysis Based on Optical Measurements," *ASME Turbo Expo 2009: Turbomachinery Technical Conference and Exposition*, 2009.

[47] Brajlih, T., Drstvensek, I., Valentan, B., and Hadzistevic, M., "Possibilities of using Three-Dimensional Optical Scanning in Complex Geometrical Inspection," *Journal of Mechanical Engineering*, Vol. 57, 2011. doi:10.5545/sv-jme.2010.152.

[48] Honisch, P., Strehlau, U., and Kuhhorn, A., "Modelling of industrial blade integrated disks (blisks) with regard to mistuning," *Procedings of ISMA2012-USD2012*, 2012.

[49] Paulic, M., Irgolic, T., Balic, J., Cus, F., Cupar, A., and Brajlih, T., "Reverse Engineering of Parts with Optical Scanning and Additive Manufacturing," *24th DAAAM International Symposium on Intelligent Manufacturing and Automation*, Vol. 69, 2014. doi:10.1016/j.proeng.2014.03.056.

[50] de Cazenove, J., Cogan, S., and Mbaye, M., "Finite-element Modelling of an Experimental Mistuned Bladed Disk and Experimental Validation," *ASME Turbo Expo 2013: Turbomachinery Technical Conference and Exposition*, 2013.

[51] Nyssen, F., and Golinval, M., "Experimental Modal Identification of Mistuning in an Academic Blisk and Comparison with the Blades Geometry Variations," *ASME Turbo Expo 2015: Turbomachinery Technical Conference and Exposition*, 2015.

[52] Stapelfeldt, S., and Vahdati, M., "On the Importance of Engine Representative Models for Fan Flutter Predictions," *Journal of Turbomachinery*, 2018. DOI: 10.1115/1.4040110.

[53] Kaszynski, A., Beck, J., and Brown, J., "Automated Finite Element Model Mesh Updated Scheme Applicable to Mistuning Analysis," *ASME Turbo Expo*, Vol. 7B, 2014. doi:10.1115/GT2014-26925.

[54] Kaszynski, A., Beck, J., and Brown, J., "Experimental Validation of an Optically Measured Digital Replica of a Geometrically Mistuned Rotor using a System ID Approach," *17th AIAA Non-Deterministic Approaches Conference*, edited by AIAA, 2015.

[55] Feiner, D., Griffin, J., Jones, K., Kenyon, J., Mehmed, O., and Kurkov, A., "System Identification of Mistuned Bladed Disks from Traveling Wave Response Measurements," *Proceedings of DETC'03 ASME 2003 Design Engineering Technical Conferences and Computers and Information in Engineering Conference*, edited by ASME, 2003, pp. 1231–1240. DOI: 10.1115/DETC2003/VIB-48448.

[56] Bertini, L., Santus, C., and Guglielmo, A., "Automated Experimental Modal Analysis of Bladed Wheels with an Anthropomorphic Robotic Station," *Experimental Mechanics*, 2017. DOI: 10.1007/s11340-016-0223-5.

[57] Kammerer, A., and Abhari, R., "Experimental Study on Impeller Blade Vibration During Resonance - Part I: Blade Vibration Due to Inlet Flow Distortion," *Journal of Engineering for Gas Turbines and Power*, 2009. DOI: 10.1115/1.2968869.

[58] Weber, R., and Kuhhorn, A., "Mistuning Identification Approach with Focus on High-Speed Centrifual Compressors," *Journal of Engineering for Gas Turbines and Power*, 2018. DOI: 10.1115/1.40040999.

[59] Beirow, B., Figaschewsky, F., Kuhhorn, A., and Bornhorn, A., "Modal Analyses of an Axial Turbine Blisk with Intentional Mistuning," *Journal of Engineering for Gas Turbines and Power*, 2018. DOI: 10.1115/1.4037588.

[60] Cox, G., Palazotto, A., Brown, J., and George, T., "Traveling Wave Excitation: A Method to Produce Consistent Experimental Results," *Journal of Engineering for Gas Turbines and Power*, Vol. 136, 2014, p. 122502(8 pages). DOI: 10.1115/1.4027744.

[61] Jones, K., and Cross, C., "Traveling Wave Excitation System for Bladed Disks," *Journal of Propulsion and Power*, Vol. 19, 2003, pp. 135–141. DOI: 10.2514/2.6089.

[62] Holland, D., Castanier, M., Ceccio, S., Epureanu, B., and Filippi, S., "Testing and Calibration Procedures for Mistuning Identification and Traveling Wave Excitation of Blisks," *Journal of Engineering for Gas Turbines and Power*, Vol. 132, No. 4, 2010, p. 042502(9 pages). doi:10.1115/1.3204656.

[63] Bertini, L., Neri, P., Santus, C., and Guglielmo, A., "One Exciter Per Sector Test Bench for Bladed Wheels Harmonic Response Analysis," *Proceedings of ASME Turbo Expo 2017: Turbomachinery Technical Conference and Exposition*, 2017.

[64] Neri, P., "Excitation Device for High Frequency Vibration Analysis: Design and Test Results," *Journal of Vibration and Control*, 2018. DOI: 10.1177/1077546317731210.

[65] Stowell, W., and Weise, R., "Application of Thin Film Strain Gages and Thermocouples for Measurement on Aircraft Engine Parts," *AIAA/SAE/ASME 19th Joint Propulsion Conference*, 1983.

[66] Klauke, T., Kuhhorn, A., Beirow, B., and Parchem, R., "Blade Vibration Phenomena of HPC Bliscs Considering Manufacturing Effects and Strain Gauge Application," *Proceedings of ASME Turbo Expo 2008: Power for Land, Sea, and Air*, Vol. 5, 2008. doi:10.1115/GT2008-50683.

[67] Manwaring, S., Rabe, D., Lorence, C., and Wadia, A., "Inlet Distortion Generated Forced Response of a Low-Aspect-Ratio Transonic Fan," *Journal of Turbomachinery*, 1997.

[68] Kenyon, J., and Minkiewicz, G., "Mistuning Characteristics of a Bladed Rotor from a Two-Stage Transonic Compressor," *34th AIAA/ASME/SAE/ASEE Joint Propulsion Conference*, 1998.

[69] Knappett, D., and Garcia, J., "Blade Tip Timing and Strain Gauge Correlation on Compressor Blades," *Proceedings IMechE Vol.222 Part G: J. Aerospace Engineering*, 1998.

[70] Heath, S., and Imregun, M., "A Survey of Blade Tip-Timing Measurement Techniques for Turbomachinery Vibration," *Journal of Engineering for Gas Turbines and Power*, 1998. DOI: 10.1115/1.2818468.

[71] Kharyton, V., Dimitriadis, G., and Defise, C., "A Discussion on the Advancement of Blade Tip Timing Data Processing," *Proceedings of ASME Turbo Expo 2017*, 2017.

[72] Besem, F., Kielb, R., Galpin, P., Zori, L., and Key, N., "Mistuned Forced Response Predictions of an Embedded Rotor in a Multistage Compressor," *Journal of Turbomachinery*, Vol. 138, 2016, p. 061003 (10 pages). doi:10.1115/1.4032164.

[73] Besem, F., Kielb, R., and Key, N., "Forced Response Sensitivity of a Mistuned Rotor From on Embedded Compressor Stage," *Journal of Turbomachinery*, Vol. 138, 2016, p. 031002 (10 pages). doi:10.1115/1.4031866.

[74] Li, J., Aye-Addo, N., III, N. K., Mathews, D., Key, N., and Kielb, R., "Mistuned Higher Order Mode Forced Response of an Embedded Compressor Rotor, Part I: Steady and Unsteady Aerodynamics," *Proceedings of ASME Turbo Expo 2017: Turbomachinery Technical Conference and Exposition*, edited by ASME, 2017. DOI: 10.1115/GT2017-64633.

[75] Li, J., Aye-Addo, N., Kielb, R., and Key, N., "Mistuned Higher Order Mode Forced Response of an Embedded Compressor Rotor, Part II: Steady and Unsteady Aerdynamcis," *Proceedings of ASME Turbo Expo 2017: Turbomachinery Technical Conference and Exposition*, edited by ASME, 2017. DOI: 10.1115/GT2017-64647.

[76] Petrov, E., Mare, L., Hennings, H., and Elliot, R., "Forced Response of Mistuned Bladed Disks in Gas Flow: A Comparitive Study o Predictions and Full-Scale Ex-

perimental Results," *Journal of Engineering for Gas Turbines and Power*, Vol. 132, 2010, p. 052504 (10 pages). doi:10.1115/1.3205031.

[77] Nicholas, T., and Zuiker, J., "On the use of the Goodman Diagram for High Cycle Fatigue Design," *International Journal of Fracture*, Vol. 80, 1996, pp. 219–235. doi: org/10.1007/BF0001267.

[78] Bartsch, T. M., "High Cycle Fatigue Science and Technology Program," Tech. rep., Air Force Research Laboratory, 2000.

[79] Nicholas, T., "Critical Issues in High Cycle Fatigue," *International Journal of Fracture*, Vol. 21, 1999, pp. 221–231. doi:10.1016/S0142-1123(99)00074-2.

[80] Nichol, K., "Reasons for Missing HCF Problems During Test," *43rd AIAA/ASME/ASCE/AHS/ASC Structures, Strual Dynamics, and Materials Conference*, 2002. doi:10.2514/6.2002-1509.

[81] EDAS, "EDAS GM Documentation Theory," *GageMap*, 2016.

[82] Aksoy, S., Mitlin, B., and Borowy, H., "Structural Evaluation and Testing of Swept Compressor Rotor," *Journal of Engineering for Gas Turbines and Power*, Vol. 116, No. 1, 1994, pp. 217–222. doi:10.1115/1.2906796.

[83] Nichol, K., "Numerical Strain Gage Representation," *39th AIAA/ASME/ASCE/AHS/ASC Structures, Structural Dynamics, and Material Conference*, 1998. doi: 10.2514/6.1998-1720.

[84] Nichol, K., "Assessment of Current Turbine Engine High Cycle Fatigue Test Methods," *Journal of Propulsion and Power*, Vol. 125, No. 3, 2003, pp. 760–765. doi: 10.1115/1.1423913.

[85] Mbaye, M., Soize, C., and Ousty, J. P., "A Reduced-Order Model of Detuned Cyclic Dynamical Systems with Geometric Modifcations using a Basis of Cyclic Modes,"

ASME Journal of Engineering Gas Turbines Power, Vol. 11, No. 132, 2010, p. 112502. doi:10.1115/1.4000805.

[86] Beirow, B., Kuhhorn, A., and Nipkau, J., "On the Influence of Strain Gauge Instrumentation on Blade Vibrations of Integral Blisk Compressor Rotors Applying a Discrete Model," *Proceedings of ASME Turbo Expo 2009: Power for Land, Sea, and Air*, Vol. 6, 2009. doi:10.1115/GT2009-59207.

[87] Kaszynski, A., and Brown, J., "Accurate Blade Tip Timing Limits through Geometry Mistuning Modeling," *Proceedings of ASME Turbo Expo 2015*, Vol. 7A, 2015. doi: 10.1115/GT2015-43192.

[88] Liu, C., and Jiang, D., "Improved Blade Tip Timing in Blade Vibration Monitoring with Torsional Vibration of the Rotor," *Journal of Physics: Conference Series*, Vol. 364, 2012, p. 012136. doi:10.1088/1742-6596/364/1/012136.

[89] Sensmeier, M. D., and Nichol, K. L., "Optimum Placement of Sensors for Vibration Measurements of Turbine Engine Blades," *39th AIAA/ASME/ASCE/AHS/ASC Structures, Structural Dynamics, and Materials Conference*, 1998. doi:10.2514/6. 1998-1849.

[90] Hah, C., Puterbaugh, S., and Copenhaver, W., "Unsteady Aerodynamic Flow Phenomena in a Transonic Compressor Stage," *Journal of Propulsion and Power*, Vol. 3, No. 13, 1997, pp. 329–333. doi:10.2514/2.5175.

[91] Heath, S., Slater, T., Mansfield, L., and Loftus, P., "Turbomachinery Blade Tip Measurement Techniques," *Proceedings 598 on Advanced Non-Intrusive Instrumentation for Propulsion Engines*, edited by AGARD, 1997.

[92] Glaessgen, E., and Stargel, D., "The Digital Twin Paradigm for Future NASA and U.S. Air Force Vehicles," *53rd AIAA/ASME/ASCE/AHS/AS Structures, Structural Dy-*

namics, and Materials Conference, edited by AIAA, 2012. DOI: 10.2514/6.2012-1818.

[93] Fredrick, N., and Hayes, B., *Best Practice: Non-Contact Stress Measurement Blade Tip-Timing*, AEDC, 2010.

[94] Hemberger, D., Filsinger, D., and Bauer, H., "Investigations on Maximum Amplitude Amplification Factor of Real Mistuned Bladed Structures," *ASME Turbo Expo 2012: Turbomachinery Technical Conference and Exposition*, 2012.

[95] Zaleski, A., "At GE Aviation, Digital Transformation Hinges on Digital Twins," , 2017. URL www.ca.com/us/modern-software-factory/content/at-ge-aviation-digital-transformation-hinges-on-digital-twins.html.

[96] Gillaugh, D., Kaszynski, A., Brown, J., Beck, J., and Slater, J., "Mistuning Evaluation Comparison via As-Manufactured Models, Traveling Wave Excitation, and Compressor Rigs," *Journal of Engineering for Gas Turbines and Power*, 2018. DOI: 10.1115/1.4042079.